

Investigation of an Alternative AC Magnetic Tracking System.

A thesis submitted in partial
fulfilment of the requirements for the degree of

Master of Engineering in Electrical and Electronic Engineering

at the University of Canterbury,
Christchurch, New Zealand
12th June 2007

Author: John Taylor
Supervisors: P. J. Bones, K. W. Eccleston



Computers are incredibly fast, accurate and stupid. Human beings are incredibly slow, inaccurate and brilliant. Together they are powerful beyond imagination.

author unknown

Acknowledgements

I would like to gratefully acknowledge the tireless efforts of Phil Bones for his guidance and invaluable contributions in many of the most complex aspects of my research, Brent Price for his practical advice, and Rachel Johnston for her support throughout the completion of my thesis. Special thanks also goes to Kim Eccleston for his expertise and critique of my ideas, Shannon Carlson, and Barrie Amtman, who helped construct and develop the test jig apparatus from which I obtained my results. Finally, I would like to thank my girlfriend Jane for her patience and support throughout my postgraduate studies.

Thanks guys, I couldn't have done it without you.

Abstract

A general overview of the hardware and software implementation requirements of an AC magnetic tracking system is presented. The overview includes an analysis of the Polhemus Fastrak, the development of mathematical models and algorithms used for magnetic tracking and the design of test jigs used to verify the results. An original non-iterative tracking algorithm that allows sensor position and orientation to be calculated in rotation matrix form is developed and verified. Future methods of calibration are proposed with results supporting the design methods. It is concluded that the algorithm presented is effective, but that further developments in hardware and software are needed in order for the system to attain the tracking resolution and accuracy specifications of other leading tracking systems.

Contents

List of Figures	xi
1 Introduction	1
1.1 Specifying the System Requirements	1
1.2 Selecting a Tracking Mechanism	2
1.2.1 Optical Tracking	2
1.2.2 RF Tracking	4
1.2.3 Inertial Tracking	4
1.2.4 Acoustic Tracking	4
1.2.5 Mechanical Tracking	5
1.2.6 Combination Tracking Systems	5
1.3 AC and Pulsed DC Magnetic Tracking	6
1.4 Development of an AC Magnetic Tracker.	7
2 Prior Art Instrumentation	9
2.1 Functionality	9
2.2 Signal Generation Circuitry	10
2.3 Signal Sensing Circuitry	13
2.4 4th Coil Circuitry	13
3 Prior Art Algorithms	15
3.1 Physical Model Development	15
3.1.1 Position Calculation	19
3.1.2 Orientation Calculation	21

4	Instrumentation and Signal Processing	23
4.1	Project Development	23
4.1.1	Signal Amplification, Sampling and Processing	24
4.1.2	System Synchronization	26
4.2	Signal Processing and Amplitude Estimation	27
4.3	Frequency Domain Estimation	28
4.3.1	Auto-correlation Estimation	29
4.3.2	Cross-correlation Estimation	29
4.3.3	Polarity Estimation	31
4.3.4	Bandlimiting the Signal	32
4.3.5	Estimation Using Weighted Averaging	33
4.4	Time Domain Estimation	34
4.5	Post Estimation Averaging	34
5	Estimation of Position and Orientation	37
5.1	Resolution of Position Magnitude	38
5.2	Resolution of Sensor Orientation	41
5.2.1	Magnetic Field Prediction	41
5.2.2	Euler Angle Resolution	45
5.2.3	Resolving Position Polarity	46
5.2.4	Orientation Continuity	48
6	Calibration	49
6.1	Sources of Distortion	50
6.1.1	Coil Position Offsets	50
6.1.2	Coil Orientation Offsets	51
6.1.3	Variations in Sensed and Detected Magnetic Fields	53
6.1.4	Internal Inter-Coil Coupling Factors	53
6.1.5	Hardware Circuitry	56
6.1.6	Aperture Correction	56
6.1.7	Environmental Effects	57
6.1.8	Complicated Coil Distortion Effects	57
6.2	Measurement of Distortion Parameters	58
6.2.1	Source Coil Position and Orientation Offsets	58
6.2.2	Internal Source Coil Coupling and Gain Variations	59

6.2.3	Sensor Coil Position and Orientation Offsets	59
6.2.4	Internal Sensor Coil Coupling and Gain Variations	59
6.2.5	Verifying the Calibration Model	60
7	Results	63
7.1	Test Jig Construction	63
7.2	Theoretical Models and Practical Data	64
7.2.1	Source Rotation Test Jig Data	65
7.2.2	Sensor Rotation Test Jig Data	66
7.2.3	Test Jig Alignment	67
7.3	Theoretical Model Calibration	67
7.3.1	Development of A Simple Calibration Model	68
7.3.2	Implementation of the Simple Calibration Model	71
7.3.3	Source Rotation Test Jig Calibration	72
7.3.4	Sensor Rotation Test Jig Calibration	73
7.4	Practical Data Calibration	74
7.5	Tracking Speed and Update Rate	76
8	Tracking System Performance	77
8.1	Resolution	77
8.1.1	Translational Resolution.	78
8.1.2	Angular Resolution	81
8.2	Accuracy	82
8.2.1	Translational Accuracy	83
8.2.2	Angular Accuracy	88
8.2.3	Increasing the Tracking Accuracy	91
9	Discussion and Conclusions	95
9.1	Research into the Polhemus Fastrak	96
9.2	Work Completed	97
9.3	Future Work	98
9.3.1	Resolution Improvements	99
9.3.2	Accuracy Improvements	100
9.3.3	Speed Improvements	100
9.3.4	Algorithmic Improvements	102

CONTENTS

9.3.5	Physical Improvements	102
9.3.6	Functionality	102
9.4	Conclusions	103
A	Research Apparatus	109
B	Coupled Coils Analysis	113
B.1	Field for current-carrying circular coil	113
B.2	Far-field approximation	114
B.3	Mutual inductance between two small circular coils	115
B.3.1	Coplanar coils	115
B.3.2	Coaxial coils	116
B.3.3	Parallel-plane coils	117
B.3.4	Coils with arbitrary positions and orientations	117

List of Figures

1.1	(a) Fastscan Cobra scanning a manequin, (b) Computer generated surface resulting from the scan.	2
1.2	(a) Polhemus Fastrak AC magnetic tracking system, (b) Ascension Flock of Birds DC magnetic tracking system.	6
2.1	Schematic of the Fastrak system.	10
2.2	Signal generation circuitry used by the Fastrak to generate magnetic fields. . .	11
2.3	Four-pulse sequence generated by the Fastrak DAC.	12
2.4	Circuitry used to amplify and detect the voltage signals induced in each sensing coil.	13
2.5	Signal excitation circuitry for the fourth coil of each Fastrak sensor.	14
3.1	(a) Position vector direction and coordinate frame rotation, (b) Coplanar and coaxial coil coupling; the distance between the coils is r in both cases.	16
3.2	Position components in terms of rotation angles A and B	20
4.1	System used to interface the professional audio development kit to the Fastrak. . .	23
4.2	Signal sensing circuitry used to detect magnetic fields.	24
4.3	Schematic of the PADK development kit used for sampling [Lyrtech (2006)]. . .	25
4.4	Sampling synchronization of the PADK and Fastrak generated magnetic fields. . .	26
4.5	Reference template signal used for the generation of magnetic fields.	27
4.6	Magnitude of the DFT of a noisy signal $D(k)$	28
4.7	Comparison between the detected pulse envelope and a window function.	32
4.8	FFT of several noisy detected signals.	33
4.9	Detected signals containing multiple sign errors and the resulting mean.	35
4.10	Bias error due to averaging the magnitude of small signals.	35

LIST OF FIGURES

5.1	(a) Sensor position with respect to the z source frame in terms of spherical coordinates r and θ , (b) Three magnetic field constant magnitude surfaces generated by three orthogonal source coils.	40
5.2	Magnetic field components in terms of rectangular and spherical coordinates. .	42
5.3	Projection of B_r and B_θ onto the rectangular coordinate system.	42
5.4	Mutually perpendicular coil orientations.	44
5.5	Octant regions into which the tracking space is divided.	47
6.1	Block diagram of the hardware components introducing distortion.	50
6.2	Sensor and source coil position offsets.	51
6.3	Coil transformations resulting from rotations $\Delta\alpha, \Delta\beta, \Delta\gamma$. Coordinates are transformed from $(x,y,z) \rightarrow (x_\alpha, y_\alpha, z_\alpha) \rightarrow (x_{\alpha\beta}, y_{\alpha\beta}, z_{\alpha\beta}) \rightarrow (x_{\alpha\beta\gamma}, y_{\alpha\beta\gamma}, z_{\alpha\beta\gamma})$ as the rotations are applied sequentially.	52
6.4	Orthogonal coils x and y located within the source or sensor.	54
6.5	Distortion of coil widths due to sequential coil windings given a coil radius of a and a coil width of w	57
6.6	Proposed method of sensor coil calibration.	58
6.7	Proposed internal sensor coil coupling test jig.	60
6.8	Proposed test jig used to verify measurement model.	60
7.1	Initial test jigs used for the verification of theory and testing of simplified calibration models.	63
7.2	Sensor position and orientation with respect to the frame of the source in the source and sensor rotation test jigs.	64
7.3	Comparison of the predicted and detected signals for the source rotation test jig.	65
7.4	Coil alignment and current direction associated with coaxial and coplanar coupling.	66
7.5	Comparison of the predicted and detected signals for the sensor rotation test jig.	67
7.6	Difference between the calibrated and detected magnetic fields in the source rotation test jig.	73
7.7	Matching the theoretical and practical models for the coils.	74
7.8	Comparison of the calibrated measured magnetic fields with the theoretical model for the source rotation test jig.	75
7.9	Comparison of the calibrated measured magnetic fields with the theoretical model for the sensor rotation test jig.	75

8.1	Variation in the resolved position coordinates as the sensor position is varied along the x axis of the source frame.	78
8.2	Frequency distribution of 10000 position measurements at a sensor position of (400,0,0) with a 270° rotation about the z axis with respect to the source frame.	79
8.3	Variation of translation resolution with range r	80
8.4	Frequency distribution of 10000 Euler angle measurements at a sensor position of (400mm,0mm,0mm) and an orientation of (0°,0°,270°) with respect to the source.	82
8.5	Sensor position coordinates calculated from the source rotation test jig.	84
8.6	Average and Statistical Range Variation with Sensor-Source Separation	85
8.7	Calculated sensor position as the sensor is rotated 360° clockwise from (90°,0,0)	87
8.8	Position coordinates resolved as the sensor moves from (100mm,0mm,0mm) to (565mm,0mm,0mm) in 15mm increments at an orientation of (0°,0°,270°).	87
8.9	Euler angles of sensor rotation from the sensor rotation test jig calculated from the detected magnetic fields and the resolved position coordinates.	89
8.10	Euler angles of sensor rotation from the sensor rotation test jig calculated from the detected magnetic fields and corrected position coordinates.	91
8.11	Euler angles of sensor rotation calculated as the sensor moves away from the source.	92
A.1	Fastrak Sensor used for the detection of AC magnetic fields via the professional audio development kit.	109
A.2	Test jig apparatus used for the measurement and analysis of magnetic fields.	110
A.3	Source rotation test jig setup.	110
A.4	Sensor rotation test jig setup.	110
A.5	The Fastrak printed circuit board.	111
A.6	.The Professional Audio Development Kit and the signal amplification circuitry used to amplify and sample voltages induced on the sensor	112

LIST OF FIGURES

Chapter 1

Introduction

1.1 Specifying the System Requirements

This project was undertaken on behalf of ARANZ Scanning Ltd., a technology company requiring further research into the capability of tracking systems complementary to the three dimensional laser scanners which it produces. Development of a new tracking system would allow closer scanner-tracker integration in a more cost effective system as opposed to current implementations which require separate tracking units from Polhemus Ltd. The project aim was therefore to review the different forms of tracking available and to undertake research and development of the most appropriate method.

The available choices for tracker implementation were extensive as trackers have been adapted for a number of diverse applications including medical, defence, entertainment, security and consumer products. In order to cater to these applications different tracking systems are used according to the cost, range, latency, accuracy, and environmental requirements of the application. The most popular forms of tracking used within the industry include optical, radio frequency, mechanical, acoustic, magnetic and inertial.

ARANZ Scanning required a tracking system with specifications similar to those of the Polhemus Fastrak (shown in Table 1.1) that ideally exceeded the specified accuracy and resolution performance. The tracking system was required to provide continual updates on the position and orientation of a hand-held wand which scanned surfaces by projection and detection of a laser as shown in Figure 1.1. The tracker could not restrict the wand freedom

of motion or use light sources which interfered with the frequencies used by the camera to resolve the surface.

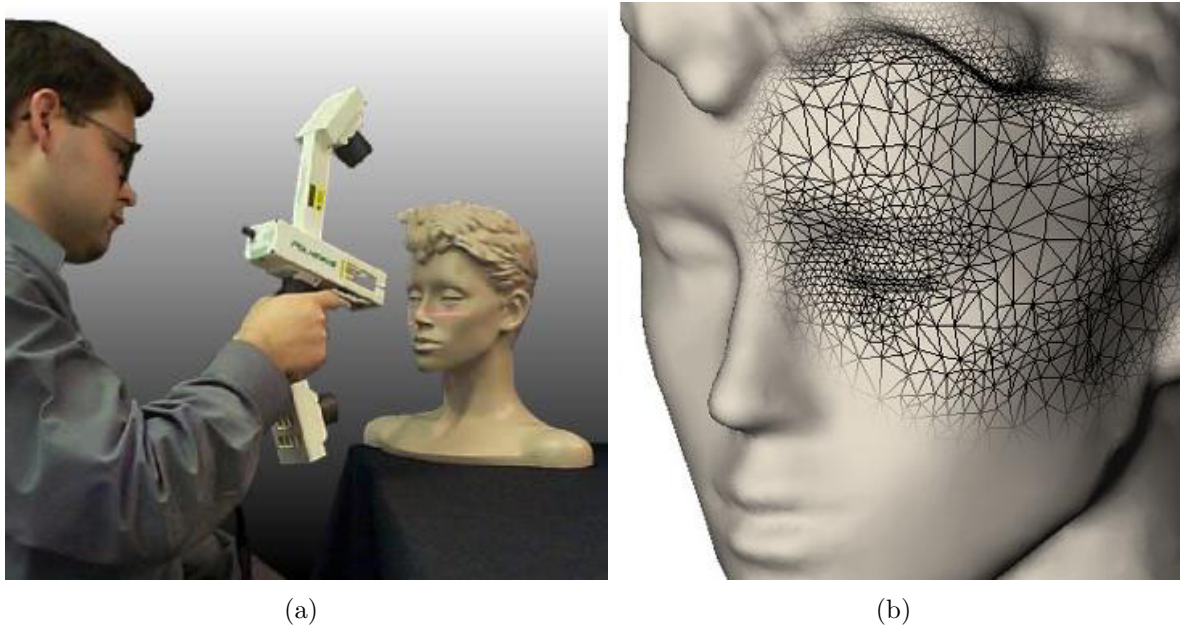


Figure 1.1: (a) Fastscan Cobra scanning a mannequin, (b) Computer generated surface resulting from the scan.

1.2 Selecting a Tracking Mechanism

The specifications of the Polhemus Fastrak (shown in table 1.1) represent the highest accuracy performance in AC magnetic tracking and compare well with other forms of commercially available tracking systems. The Polhemus Fastrak does however require a precise construction and calibration methodology. It is susceptible to hemispheric ambiguity and metallic interference resulting in a significant technical knowledge requirement and increased construction costs. It is worthwhile therefore to consider competing forms of tracking. These are briefly reviewed over the following sections.

1.2.1 Optical Tracking

Optical tracking encompasses a number of differing technologies which utilize light as a method of detecting the position and orientation of a remote object. Optical tracking systems are capable of high levels of accuracy, however the dependence on light can result in

Polhemus Fastrak Specifications		
<i>Characteristic.</i>	<i>Specification.</i>	<i>Description.</i>
Range	760 mm	Source - sensor separation distance over which the tracking system maintains its specifications.
Update Rate	120 updates per second	Maximum rate at which new measurements may be sampled, processed, and communicated to an external processor.
Translational Resolution	0.0005 mm/mm of range	The precision of the position measurements of the tracking system. Dependent upon the SNR of the detected signals (which decreases with range), the position resolution is calculated from the standard deviation of each of the resolved position coordinates.
Angular Resolution	0.025°	The precision of the orientation measurements of the tracking system. Dependent on the SNR of the detected signals, the angular resolution is calculated from the standard deviation of each the resolved Euler angles.
Static Position Accuracy	0.8 mm	The position error between the calculated and actual sensor positions within the tracking field, determined from test jig measurements.
Static Orientation Accuracy	0.15°	The orientation error between the calculated and actual sensor positions within the tracking field, determined from test jig measurements.
Latency	4.0 ms	Time taken for the tracker to detect, process, and indicate that a new measurement is ready to an external processor.

Table 1.1: Performance specifications of the Polhemus Fastrak system.[Polhemus (2004)]

environmental interference. Optical tracking systems can be categorized into three different forms. *Pattern recognition systems* (such as the 3rdTech ‘Hiball’) use multiple prearranged external sources to allow motion detection via a remote sensor in space. *Image based systems* (such as the Vicon ‘Peak Motus’) use one or more cameras to resolve object motion through video detection. *Structured light or laser systems* (such as the Ascension ‘laserBIRD 2’) use directed light that can be resolved with a source - sensor system. Optical tracking systems tend to be more expensive and can be limited by occlusion (blockage of the line of sight between the sensor and source) problems, however specifications of latency, update rate, and accuracy compare well with other competing forms of tracking.

1.2.2 RF Tracking

Radio frequency tracking may be used to track an object accurately by using spatially separated sources and sensors which are capable of transmitting or receiving an electromagnetic signal. By using time-of-flight and phase detection techniques the remote position of an object may be determined via long or short range transmission and detection. While this has been used to provide a method of the position tracking with millimetre resolution for a number of differing systems (including global positioning, vehicle and military tracking), there are no commercial RF tracking systems currently offering the capability of orientation tracking to the knowledge of the author.

1.2.3 Inertial Tracking

Inertial tracking involves the use of sensors capable of determining the gravitational attraction and inertial motion of an object to resolve the movement and orientation. Such mechanisms are generally limited to three degrees of freedom orientation tracking due to position drift susceptibility (constant velocity implies zero acceleration which can imply significant position drift offsets). In spite of these drawbacks, inertial trackers are cheap, sourceless, largely immune to other environmental effects and are capable of resolving orientation to sub-degree resolution. Several companies market such orientation trackers however most combine inertial tracking with sourceless magnetic tracking of the Earth’s magnetic field (such as the Ascension ‘3D Bird’, Polhemus ‘Minuteman’ and Intersense ‘InertiaCube2’).

1.2.4 Acoustic Tracking

Multiple sonic sensors and sources may be used to determine the position and orientation of an object by detecting the level of attenuation, time of flight, and phase variations in

the acoustic signal. Acoustic tracking systems have an extended operating area and commercially available trackers (such as the Intersense ‘IS-900 Mark 2’) specify latency, update rate, accuracy and resolution specifications that are close to those of the Polhemus Fastrak. Acoustic trackers do however suffer from environmental effects of reflection and scattering and from similar occlusion problems to optical trackers. In spite of this, the low construction cost and comparatively simple technical development requirements make acoustic tracking an attractive alternative for suitable applications.

1.2.5 Mechanical Tracking

Mechanical tracking is fast, accurate, and largely immune to environmental interference. Tuned mechanical trackers provide the best position and orientation accuracy resolution specifications currently available (such as Force Dimension ‘6-DOF Delta’ and Sensable Technologies ‘Phantom 1.5 6 DOF HF’) and for this reason are often used to calibrate other forms of trackers. In spite of this, mechanical trackers are severely limited by tethering requirements and contain a significant number of precisely calibrated moving components. As a result, mechanical trackers can be expensive and provide significant limitations to the movement capability of the tracked object.

1.2.6 Combination Tracking Systems

A number of the forms of tracking described above have significant drawbacks based on the respective environmental requirements. Current research is being undertaken into the development of systems which utilize multiple forms of tracking in order to minimize the environmental effects. Such tracking combinations include MARG (Magnetic, Angular Rate, Gravity), mechanical/inertial, (in motion capture suits), and optical/inertial (such as the Nintendo Wii controller). Such tracking systems have been demonstrated as being effective and are a current area of active research. However, in order to develop such systems, the construction of multiple tracking systems is required, thereby increasing the development time and knowledge requirement.

A number of factors must be taken into account when determining the appropriate form of tracking system. First, and most importantly, the specifications of the system must be equal or above those of the current AC magnetic tracking system which is produced by Polhemus Ltd. Second, the system must be cost-effective and not impose significant restrictions on the scanning wand. Finally, the system must be able to be researched in a relatively short

time frame (less than 2 years). These requirements eliminate the majority of the tracking systems, as inertial and acoustic tracking mechanisms are too inaccurate for the application specifications, while mechanical systems are too restrictive and lack the freedom of motion required by the current product. RF and optical tracking systems are able to provide highly accurate methods of resolving these problems, however the RF detection is limited to three degrees of freedom and optical systems are dependent upon precise lighting and environmental conditions. Thus, the most appropriate form of tracking to replace the current tracking system is magnetic.

1.3 AC and Pulsed DC Magnetic Tracking

Current commercially available magnetic tracking systems may be formed into two distinct categories - AC and pulsed DC. AC magnetic tracking systems utilize an alternating current to generate a magnetic field which may be sensed at a remote location. Such an implementation allows an amplitude modulation scheme to be implemented on a low-frequency carrier signal. Those carrier signals are required to remain low frequency in order to allow the magnetic fields to be approximated as static (i.e., quasi-static) magnetic fields.



Figure 1.2: (a) Polhemus Fastrak AC magnetic tracking system, (b) Ascension Flock of Birds DC magnetic tracking system.

In contrast, pulsed DC magnetic tracking systems use time-multiplexed DC signals which, when excited, generate a steady state magnetic field at the sensor location. Such an implementation allows the minimization of the distortion effects inherent in localized metallic objects by allowing eddy currents to settle prior to measurements being taken. While this

system of magnetic detection demonstrates greater resilience towards metallic distortion, the detection of DC magnetic fields must be separated from the inherent magnetic fields of the Earth.

Both AC and DC magnetic tracking systems are mature products, with both systems having implementations currently sold commercially - the Fastrak by Polhemus (AC) and the Flock of Birds by Ascension (Pulsed DC) shown in Figure 1.2. Although the companies marketing these products appear to differ on their comparative performances, it appears that the AC magnetic tracking system is able to attain a higher level of accuracy than that of its DC counterpart.

1.4 Development of an AC Magnetic Tracker.

The project aim of the development of a tracking system to match the specifications of the Polhemus Fastrak is well suited to the development of an original AC magnetic tracking system. ARANZ Scanning Ltd currently produces scanners designed to have minimal distortion effects on magnetic fields and has some knowledge of the basic operations of an AC magnetic tracker. The following chapters will outline an investigation into the currently implemented system and the research and development of alternate methods that would be required for the generation of an original tracker.

1. INTRODUCTION

Chapter 2

Prior Art Instrumentation

2.1 Functionality

The Polhemus Fastrak is a magnetic tracking system which uses AC magnetic fields amplitude modulated with a Hanning window onto one of four carrier frequencies to resolve a position and orientation measurement. The system utilizes a three-coil source and four-coil sensor in order to generate, sense and self-calibrate the magnetic fields used to resolve the position and orientation of the sensor. The size and type of the sources may be altered according to the range requirements of the tracking application, however the use of longer range, larger size, higher current tracking sources generally results in a lower position and orientation accuracy due to additional distortion being generated.

The Fastrak is controlled by a DSP which synchronizes the generation and detection of the magnetic fields, resolves the position and orientation of the sensor, converts it into the appropriate format and communicates it to an external processor as shown in Figure 2.1. The DSP also controls the multiplexing circuitry in the transmitter and interfaces to several SRAM modules. An FTDI serial-to-USB converter is used to transmit the detected position and orientation measurements in both USB and serial RS232 formats to the external processor. The Fastrak is able to track up to four targets, a process which is achieved by the introduction of additional sensors which are time multiplexed in the tracking process to

Number of Sensors:	1	2	3	4
Update Rate (Updates/Second):	120	60	40	30

Table 2.1: Updates rates for the Polhemus Fastrak [Polhemus (2004)].

allow their position to be determined. Inherent with such a time-multiplexing process is the reduction of the update rate according to the number of sensors being tracked as shown in table 2.1.

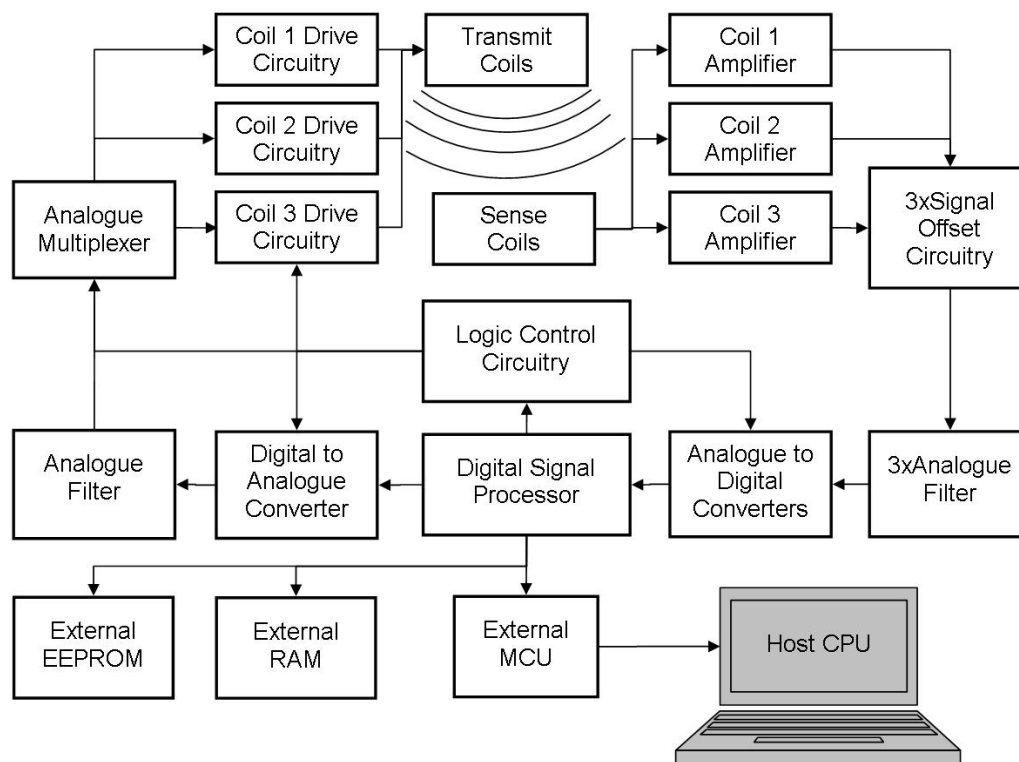


Figure 2.1: Schematic of the Fastrak system.

Additional adjustments can also be made to the tracking range which may be extended by using a larger, higher power transmitter to generate larger magnetic fields that may be detected by the sensors. In addition to this the Fastrak contains a number of features which allow the user to alter the characteristics of the tracking system so that an adaptive filter can be adjusted to the environment in which the system is operating.

2.2 Signal Generation Circuitry

Figure 2.2 illustrates the signal generation components used within the Fastrak system. A 14-bit voltage-output bipolar DAC is used to generate a sequence of four signals modulated onto one of four carrier frequencies (8.013kHz, 10.016kHz, 12.019kHz, or 14.022kHz) as shown in Figure 2.3. A second order multiple feedback bandpass filter implemented using a low cost

TL072 amplifier is used to eliminate the DAC generation noise before the signal is passed to a CD4053 analogue multiplexer. The first three pulses are passed onto an analogue amplifier, while the fourth is passed through a separate channel and used to calibrate the receiving coils (discussed in Section 2.4).

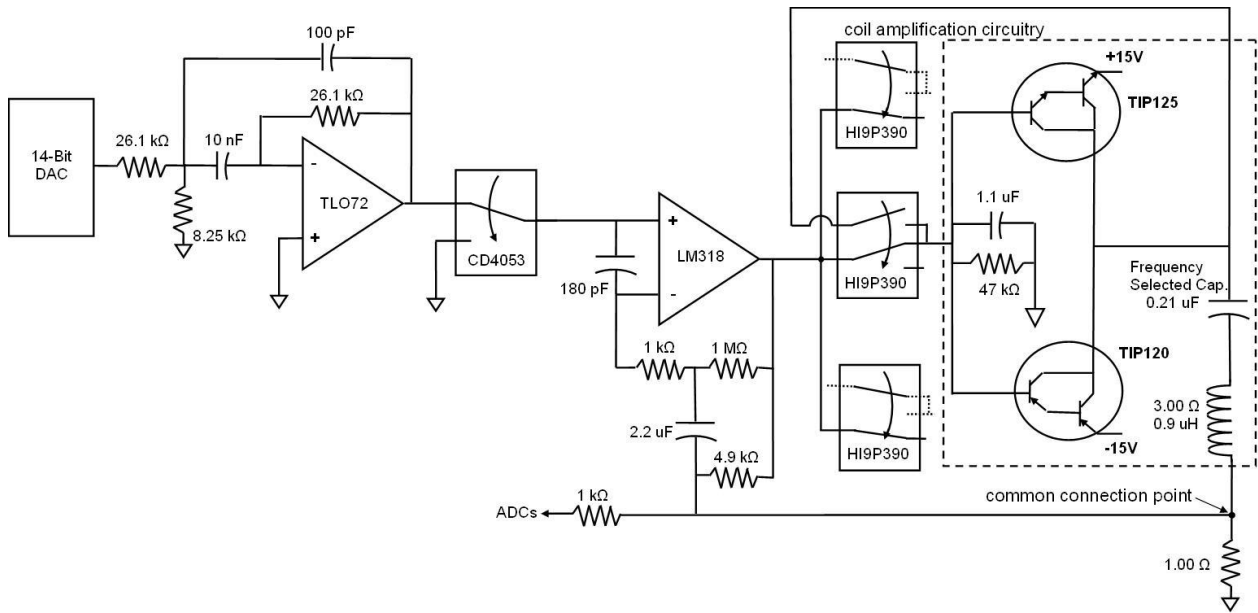


Figure 2.2: Signal generation circuitry used by the Fastrak to generate magnetic fields.

The three pulses are amplified by the LM318M and passed onto three HI9P390 multiplexers connected to three identical coil excitation circuits (shown in the dashed box). The voltage across all of the coils is controlled by the same LM318M amplifier and the return leads of all three source coils are connected to a common point. During the excitation of each coil the amplification circuitry of the alternate coils is short circuited via the HI9P390 multiplexers preventing multiple signals from being transmitted. The negative feedback path of the LM318M amplifier is used to control the generated signal and includes a class-B power amplifier design which drives a series resonant RLC circuit. This allows the bipolar signal generated by the amplifier to be significantly amplified (from $\pm 5\text{V}$ to $\pm 90\text{V}$) between the capacitor and inductive coil while maintaining control of the amplified signal. Amplifying the signal prior to the multiplexing stage also eliminates the requirement for each of the coils to be amplified separately. In order to supply the current requirements of each resonant circuit, two complementary TIP125 and TIP120 darlington pair transistors are used, switching off and on rapidly according to the polarity of the signal. While such power amplifier configurations tend to produce significant switching noise, the implementation of a resonant circuit causes

2. PRIOR ART INSTRUMENTATION

this noise to be reduced by a filtering effect.

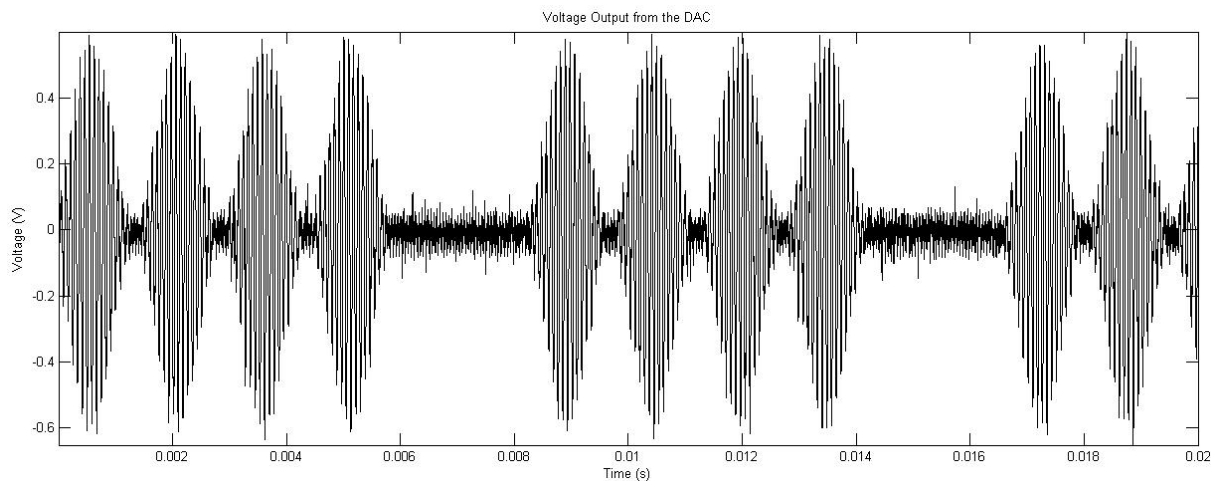


Figure 2.3: Four-pulse sequence generated by the Fastrak DAC.

In order for the Fastrak to operate on four different frequencies the resonant circuit must be frequency matched to the carrier frequency. In order to achieve this both a software change (generating a message signal modulated onto a different carrier frequency) and a hardware change (replacing the capacitors in order to allow the circuit to resonate at the corresponding frequency) is required. A detachable daughter-board is included which contains the three source coil capacitors for this purpose.

The switching system is particularly important as the excitation of each source coil causes large magnetic fields to be generated. If a small amount of coupling exists between the source coils, a current can be induced within the perpendicular coils causing the generation of magnetic fields. Although the use of switches minimizes such effects, secondary currents are induced within the transmitter causing the generation of small perpendicular magnetic fields that distort the transmitted signal.

In order to maintain an accurate measure the signal passing through each source coil and allow a precise comparison with the signal being received at the given location, the transmitted signal is passed through a feedback mechanism to the ADCs. The coils are wound to precise inductance and impedance specifications and are manufactured by Polhemus using precise winding mechanisms, however inherent differences inevitably arise which must be measured.

2.3 Signal Sensing Circuitry

The sensing system uses three mutually orthogonal coils to detect the direction and orientation of the magnetic fields in the frame of the sensor. Each coil is associated with a separate low noise amplifier which is set to have a fixed gain of 200. In order to avoid problems with the current being too large to accurately resolve the pulse envelope, the transmitted signal power is reduced as the sensor moves progressively closer to the transmitter position.

Each coil is amplified using a dedicated SSM2019 instrumentation amplifier and is protected from overvoltage and electrostatic discharge with a SP720 ESD protection array. A passive high-pass RC filter with a cutoff frequency of 5 KHz is used to allow the sensor to remain grounded and prevent the signal from drifting over the voltage range. Any DC bias is removed by a series capacitor and the output is passed through a set of multiplexers, which isolate the given set of three mutually orthogonal coils as shown in Figure 2.4.

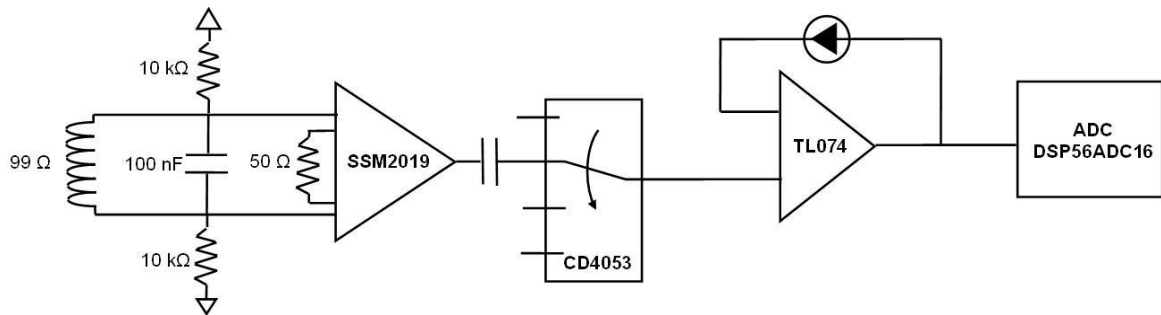


Figure 2.4: Circuitry used to amplify and detect the voltage signals induced in each sensing coil.

As there are four available sensor connectors and twelve dedicated instrumentation amplifiers (three coils per connector), the multiplexers are required to identify the signals from the three coils currently being sensed and transmit those signals to the ADCs. A standard TL074 amplifier is used with a reverse biased LM336 diode to offset each of the three signals by 2.5V, biasing the signals to minimize over-voltage and under-voltage clipping in the sigma-delta ADCs.

2.4 4th Coil Circuitry

Each sensor contains a fourth coil which is used for real-time calibration of the tracking system. A signal of with the same carrier frequency and a similar envelope to those generated in

2. PRIOR ART INSTRUMENTATION

the transmitting coils is excited in the fourth coil of each Fastrak sensor. The signals induced in the three orthogonal sensing coils are amplified and passed to the ADC's to detect variations in the sensor at the time of measurement.

The Fastrak system allows four sensors to be tracked simultaneously. Each sensor contains a fourth coil which is excited independently. Figure 2.5 illustrates the mechanism by which the signal is generated within the fourth coil of each sensor.

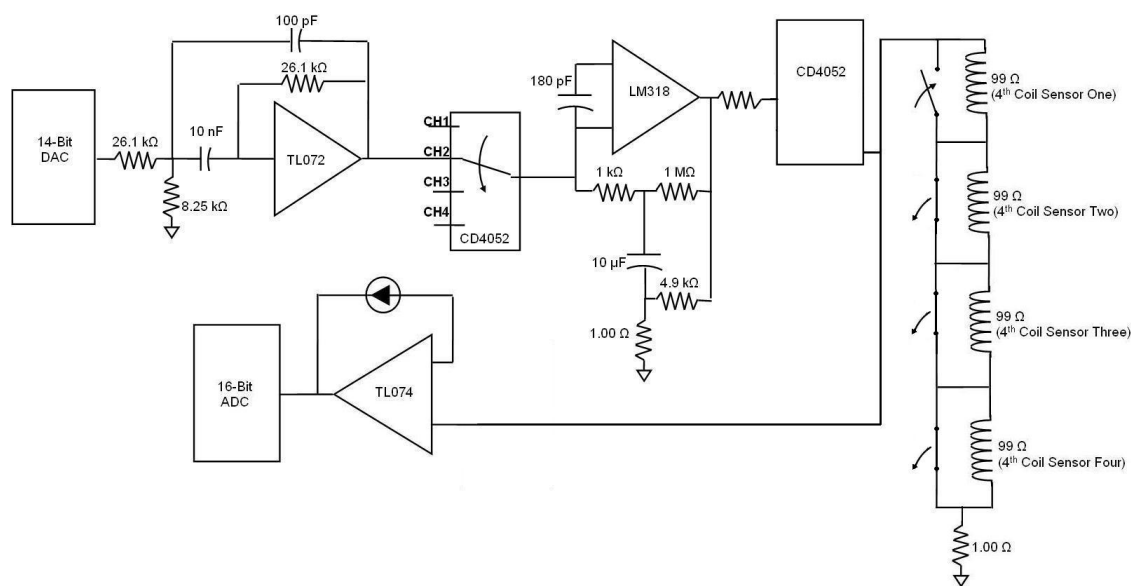


Figure 2.5: Signal excitation circuitry for the fourth coil of each Fastrak sensor.

The fourth coil signal is generated by the DAC as a 'fourth pulse' after the three pulses used for excitation of each of the transmitting coils. A multiplexer is used to separate the fourth pulse from the other three pulses and the signal passes through the fourth coil of each sensor connected to the Fastrak. The fourth pulse is also passed directly through an amplifier to an ADC allowing direct comparison with the signals detected on the three sensing coils.

Although the current flows through every fourth coil of every sensor connected to the Fastrak each sensor is calibrated independently. A switch is used to provide a low-impedance short across each fourth coil sensor whenever the sensor is not being calibrated. Hence, each of the four normally closed switches will open whenever the corresponding sensor is to be calibrated.

Chapter 3

Prior Art Algorithms

A significant amount of research has been undertaken into the algorithms and processes used in AC magnetic tracking. Many of these have demonstrated operational tracking systems with good results [Liu (2004)], however none of the research undertaken has been able to exceed the Fastrak accuracy specifications. For this reason the focus of the prior art research has been on the patents produced by Polhemus [Kuippers (1988)] [Jones (1994)][Jones (1988)]. Most attention is paid in particular to the research undertaken in [Kuippers (1988)] which outlines the fundamental algorithms used for tracking in the Fastrak.

3.1 Physical Model Development

The calculation of the sensor position and orientation with respect to the source is based on a set of nine measurements from the sensor coils. When each of the three source coils is excited the induced voltage on each of the three sensor coils is measured. A signal matrix S is formed with the measurements arranged according to the source coil being excited (by row) and the detecting sensor coil (by column) as shown in equation 3.1.

$$S = \begin{bmatrix} s_{Xx} & s_{Xy} & s_{Xz} \\ s_{Yx} & s_{Yy} & s_{Yz} \\ s_{Zx} & s_{Zy} & s_{Zz} \end{bmatrix} \quad (3.1)$$

The position and orientation of the sensor may be determined by using matrix algebra to represent the physical path between the source and sensor coils. If the source is arbitrarily assigned to be located at the origin of a right-handed coordinate system, then a unit vector \hat{p} directed along the line between the source and sensor positions may be defined as shown in

3. PRIOR ART ALGORITHMS

figure 3.1(a).

Two rotation angles A and B are defined which allow the source co-ordinate frame to be rotated so that the x axis is aligned with the direction of the sensor. A is defined as the counter-clockwise angle of rotation between the x axis and the projection of $\hat{\mathbf{p}}$ onto the xy plane, while B is the angle from the xy plane to $\hat{\mathbf{p}}$. This co-ordinate frame transformation may be represented by a rotation matrix P as shown in equation 3.2.

$$P = \begin{bmatrix} \cos(A) \cos(B) & \sin(A) \cos(B) & -\sin(B) \\ -\sin(A) & \cos(A) & 0 \\ \cos(A) \sin(B) & \sin(A) \sin(B) & \cos(B) \end{bmatrix} \quad (3.2)$$

If a source coil is excited and the generated magnetic fields are detected by two identical sensor coils of the same orientation located a distance r along the y and z axes respectively the detected magnetic fields will differ. The sensor coil co-axially aligned with the source coil along the z axis will detect twice the magnetic field of the sensor coil in coplanar alignment with the source along the y axis as shown in Figure 3.1(b).

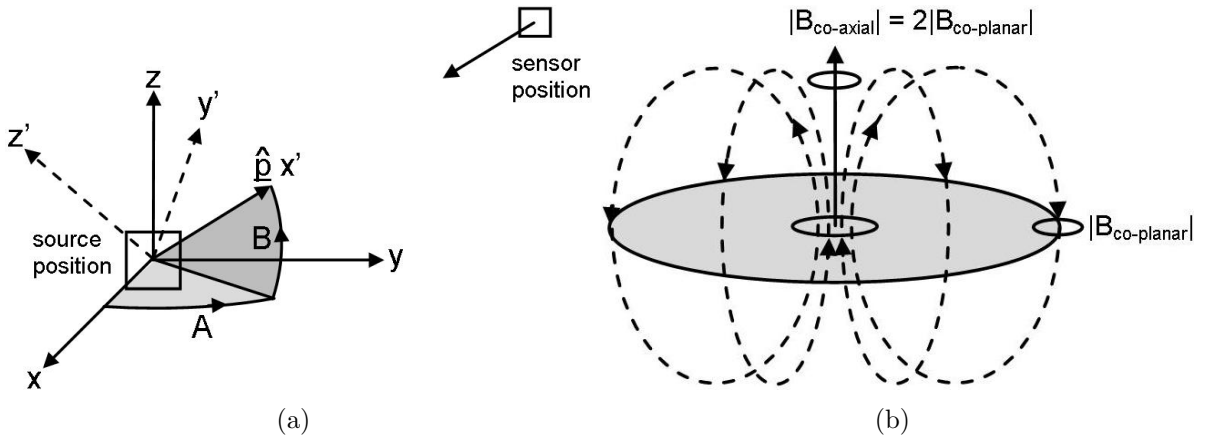


Figure 3.1: (a) Position vector direction and coordinate frame rotation, (b) Coplanar and coaxial coil coupling; the distance between the coils is r in both cases.

Therefore, if each of the three source coils are excited sequentially the magnitude and direction of the magnetic field detected at a given point in space will be different according to the position with respect to the excited source coil. Furthermore, if a sensor coil is axially aligned with a source coil, the magnetic fields detected by the sensor will be in the same direction as that generated by the source (i.e. positive) while a coplanar sensor located in the plane of

the source will detect a magnetic field in the opposite (i.e. negative) direction. This magnetic field alignment may be represented by a coupling matrix H , defined in equation 3.3.

$$H = \begin{bmatrix} 2 & 0 & 0 \\ 0 & -1 & 0 \\ 0 & 0 & -1 \end{bmatrix} \quad (3.3)$$

In order to resolve the magnetic field direction at the three-coil sensor position, the coupling matrix must be resolved into the direction components of the sensor. The angles A and B will not change if the sensor moves directly toward or away from the source, and are therefore direction invariant (but not magnitude invariant) along the direction of $\hat{\mathbf{p}}$. The direction of the magnetic fields for sensor positions located along the vector $\hat{\mathbf{p}}$ may be represented by HP .

The magnitude of the magnetic fields detected by the sensor will depend upon the source-sensor separation distance which can be introduced using an attenuation factor ‘ k ’ that will be defined at a later stage. k is related to the range, and decreases with an inverse cube relationship as shown in equation 3.4.

$$k \propto \frac{1}{r^3} \quad (3.4)$$

The magnitude of the magnetic fields also decrease with an inverse cube relationship to the range and thus the attenuation factor k is a useful method of describing the magnitude of the magnetic fields for any given range. The magnetic fields at the sensor position may therefore be represented by equation 3.5.

$$B_{relative} = kHP \quad (3.5)$$

In order to associate the frame of the $\hat{\mathbf{p}}$ vector with the sensor frame a ‘tracking matrix’ Q may be used to relate the magnetic fields detected by the sensor to the orientation of the magnetic fields at the given point in space as shown in equation 3.6.

$$S = kQHP \quad (3.6)$$

This is not however a convenient method of moving between the co-ordinate frames as the sensor orientation remains coupled to the sensor direction matrix P . If the tracking matrix Q is defined in terms of the rotation matrix P^T which rotates the system back into the frame of the source, a source to sensor rotation matrix A may be used to obtain the orientation of the source with respect to the orientation of the sensor. In order to allow representation of

3. PRIOR ART ALGORITHMS

any orientation, the rotation matrix A must allow rotation about all three Euler axes, namely heading, elevation, and roll, thus:

$$A = \begin{bmatrix} \cos(h) \cos(e) & \sin(h) \cos(e) & -\sin(e) \\ \cos(h) \sin(e) \sin(r) - \sin(h) \cos(r) & \sin(h) \sin(e) \sin(r) + \cos(h) \cos(r) & \cos(e) \sin(r) \\ \cos(h) \sin(e) \cos(r) + \sin(h) \sin(r) & \sin(h) \sin(e) \cos(r) - \cos(h) \sin(r) & \cos(e) \cos(r) \end{bmatrix}$$

The resulting relationship for the signal matrix is then:

$$S = kAP^T HP \quad (3.7)$$

The attenuation factor k is the only factor within the model of equation 3.7 which allows for variation in the magnitude of the elements of S as the range is altered. Thus, by manipulating the detected signal matrix S so that k is independently related to the detected signals, the attenuation of the magnetic fields may be resolved. In order to determine the attenuation factor k which relates the magnitude of the magnetic fields to the range, equation 3.7 may be altered to:

$$\begin{aligned} S^T S &= (kAP^T HP)^T (kAP^T HP) \\ &= (kP^T H^T PA^T) (kAP^T HP) \end{aligned} \quad (3.8)$$

The rotation matrices A and P which are used to rotate the frame of reference are orthonormal and therefore $A^T = A^{-1}$, $P^T = P^{-1}$. H is also diagonal and as a result $H = H^T$. Thus, equation 3.8 can be manipulated into:

$$\begin{aligned} S^T S &= k^2 P^T H^T P A^T A P^T H P \\ &= k^2 P^T H P A^{-1} A P^{-1} H P \\ &= k^2 P^T H^2 P \end{aligned} \quad (3.9)$$

and, expanding the right hand side,

$$k^2 P^T H^2 P = k^2 \begin{bmatrix} P_{11} & P_{21} & P_{31} \\ P_{12} & P_{22} & P_{32} \\ P_{13} & P_{23} & P_{33} \end{bmatrix} \begin{bmatrix} 4 & 0 & 0 \\ 0 & 1 & 0 \\ 0 & 0 & 1 \end{bmatrix} \begin{bmatrix} P_{11} & P_{12} & P_{13} \\ P_{21} & P_{22} & P_{23} \\ P_{31} & P_{32} & P_{33} \end{bmatrix} \quad (3.10)$$

The sum of the components along the diagonal of equation 3.10 is the trace and and may be

expressed as:

$$\begin{aligned}
 Tr(P^T H^2 P) &= k^2 \left[4P_{11}^2 + P_{21}^2 + P_{31}^2 + 4P_{12}^2 + P_{22}^2 + P_{32}^2 + 4P_{13}^2 + P_{23}^2 + P_{33}^2 \right] \\
 &= k^2 \left[4(P_{11}^2 + P_{12}^2 + P_{13}^2) + (P_{21}^2 + P_{22}^2 + P_{23}^2) + (P_{31}^2 + P_{32}^2 + P_{33}^2) \right] \\
 &= k^2 \left[4(\cos^2(A) \cos^2(B) + \sin^2(A) \cos^2(B) + \sin^2(B)) + (\sin^2(A) + \cos^2(A)) \right. \\
 &\quad \left. + (\cos^2(A) \sin^2(B) + \sin^2(A) \sin^2(B) + \cos^2(B)) \right] \\
 &= k^2[4 + 1 + 1] = 6k^2
 \end{aligned} \tag{3.11}$$

Thus, by using the detected signal matrix S , the magnitude of the attenuation factor of the magnetic fields k may be determined as shown in equation 3.13.

$$k^2 = \frac{1}{6} Tr(P^T H^2 P) = \frac{1}{6} Tr(S^T S) \tag{3.12}$$

$$k = \sqrt{\frac{1}{6} Tr(S^T S)} \tag{3.13}$$

If the value of $k = k_0$ is resolved at a known range $r = r_0$, then from equation 3.4 the range may be calculated thereafter by using:

$$r = r_0 \left(\frac{k_0}{k} \right)^{\frac{1}{3}} \tag{3.14}$$

3.1.1 Position Calculation

The sensor position may be determined by resolving the projection of the position vector $\hat{\boldsymbol{p}}$ onto the three co-ordinate axes as shown in Figure 3.2. The calculation of each projected component may be conducted by manipulating the model established in Section 3.1 to separate the P matrix as shown in the following.

$$\begin{aligned}
 S^T S &= (kAP^T HP)^T (kAP^T HP) \\
 &= (kIP^T HPA^T) (kAP^T HP) \\
 &= k^2 P^T H^2 P
 \end{aligned} \tag{3.15}$$

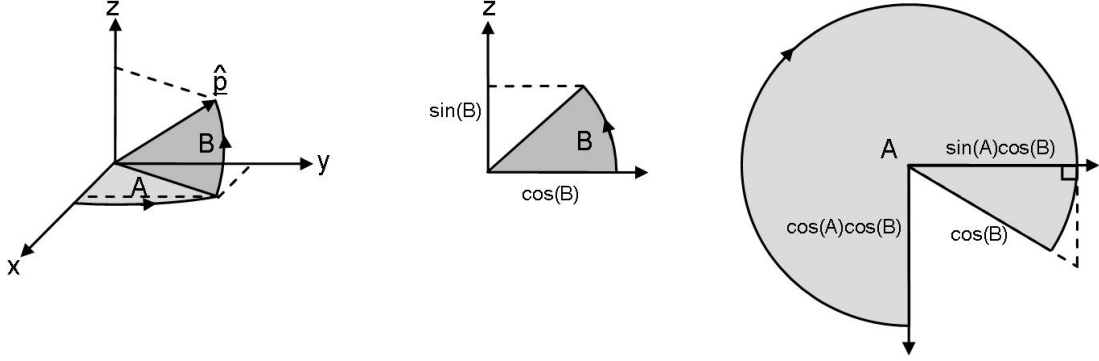


Figure 3.2: Position components in terms of rotation angles A and B.

Noting from equation 3.10 that $H^2 = I + 3E$, where

$$E = \begin{bmatrix} 1 & 0 & 0 \\ 0 & 0 & 0 \\ 0 & 0 & 0 \end{bmatrix}$$

then

$$S^T S = k^2 P^T P + k^2 P^T 3EP \quad (3.16)$$

$$= k^2 I + k^2 P^T 3EP \quad (3.17)$$

In order to identify the required projected components, a position matrix X may be defined which contains the magnitude of the axis components along the diagonal, the polarity of which may be resolved by using the components of the third row as shown in equation 3.18.

$$\begin{aligned} X &= \frac{1}{3} \left(\frac{1}{k^2} S^T S - I \right) = P^T EP \\ &= \begin{bmatrix} \cos(A) \cos(B) & 0 & 0 \\ \sin(A) \cos(B) & 0 & 0 \\ -\sin(B) & 0 & 0 \end{bmatrix} \begin{bmatrix} \cos(A) \cos(B) & \sin(A) \cos(B) & -\sin(B) \\ -\sin(A) & \cos(A) & 0 \\ \cos(A) \sin(B) & \sin(A) \sin(B) & \cos(B) \end{bmatrix} \\ &= \begin{bmatrix} \cos^2(A) \cos^2(B) & \sin(A) \cos(A) \cos^2(B) & -\cos(A) \sin(B) \cos(B) \\ \sin(A) \cos(A) \cos^2(B) & \sin^2(A) \cos^2(B) & -\sin(A) \sin(B) \cos(B) \\ -\cos(A) \sin(B) \cos(B) & -\sin(A) \sin(B) \cos(B) & \sin^2(B) \end{bmatrix} \quad (3.18) \end{aligned}$$

As \hat{p} is a unit vector, the vector components projected onto the x, y, and z axes represent a fractional component of the source-sensor separation distance using equations 3.19, 3.20, and 3.21. The distance along each axis may be resolved by multiplying each fractional component

by the range r from equation 3.14.

$$\left| \frac{x}{r} \right| = \sqrt{X_{(1,1)}} = \cos(A) \cos(B) \quad (3.19)$$

$$\left| \frac{y}{r} \right| = \sqrt{X_{(2,2)}} = \sin(A) \cos(B) \quad (3.20)$$

$$\left| \frac{z}{r} \right| = \sqrt{X_{(3,3)}} = \sin(B) \quad (3.21)$$

A fundamental limitation of a coil-based AC magnetic tracking system is that the magnetic fields are symmetric and for any given position in space two locations exist at which identical sets of magnetic fields can be detected. This is referred to as a ‘hemispheric ambiguity’. As a result of this ambiguity, only the polarity of one co-ordinate may be determined with certainty while the x and z co-ordinates depend on whether x is assigned to be positive or negative. If the polarity of a value is represented as $pol(value)$ then the polarity of the x, y, and z co-ordinates may be represented as shown in equations 3.22, 3.23, and 3.24.

$$pol(x) = pol\left(X_{(1,1)}\right) = pol\left(\pm \sin(B)\right) \quad (3.22)$$

$$\begin{aligned} pol(y) &= pol\left(X_{(2,1)}\right) = pol\left(\sin(A) \cos(A) \cos^2(B)\right) \\ &= pol\left(\sin(A) \cos(A)\right) \cos^2(B) \end{aligned} \quad (3.23)$$

$$\begin{aligned} pol(z) &= pol\left(X_{(3,1)}\right) = pol\left(-\sin(B) \cos(A) \cos(B)\right) \\ &= pol\left(\cos(A) \cos(B)\right) pol(x) \end{aligned} \quad (3.24)$$

The position of the sensor must therefore begin from a known hemisphere (known x polarity) and remain within that hemisphere throughout the duration of the tracked motion. The Fastrak allows external user calibration to be applied so that the initial sensor hemisphere can be specified.

3.1.2 Orientation Calculation

The orientation of the sensor with respect to the source frame can be determined by resolving the orientation matrix A from the detected signal matrix S . The relationship developed in

3.16 may be used to separate the orientation matrix.

$$\begin{aligned}
 S^T S - 2k^2 I &= (k^2 P^T P + 3k^2 P^T E P) - 2k^2 I \\
 &= 3k^2 P^T E P - k^2 P^T I P \\
 &= k^2 P^T H P \\
 &= k A^T S
 \end{aligned} \tag{3.25}$$

If both sides of equation 3.25 are right multiplied by S^{-1} the orientation matrix may be separated from the S matrix as shown in equation 3.26.

$$S^T - 2k^2 S^{-1} = k A^T \tag{3.26}$$

This allows the orientation matrix A to be resolved as shown in equation 3.27.

$$A = \frac{1}{k} S - 2k \left(S^{-1} \right)^T \tag{3.27}$$

The orientation matrix was defined as a three axis rotation matrix, and may be resolved into its component angles of rotation as shown in equation 3.28.

$$\begin{aligned}
 e &= \sin^{-1} \left(-A_{(1,3)} \right) = \sin^{-1} \left(\sin(e) \right) \\
 h &= \tan^{-1} \left(\frac{A_{(1,2)}}{A_{(1,1)}} \right) = \tan^{-1} \left(\frac{\cos(e) \sin(h)}{\cos(e) \cos(h)} \right) \\
 r &= \tan^{-1} \left(\frac{A_{(2,3)}}{A_{(3,3)}} \right) = \tan^{-1} \left(\frac{\cos(e) \sin(r)}{\cos(e) \cos(r)} \right)
 \end{aligned} \tag{3.28}$$

This method of resolving Euler angles from a rotation matrix contains rotation angle ambiguities (multiple sets of Euler angles may be used to represent the same rotation) and is susceptible to gimbal lock (which occurs when $\sin(e) = 1$ and $\cos(e) = 0$). Such topics were not addressed in prior art patents [Kuipers (1988)]. The shortcomings of these methods are discussed further in Section 5.2.2.

Chapter 4

Instrumentation and Signal Processing

4.1 Project Development

The initial development of a tracking system is difficult to achieve without significant precisely constructed hardware requiring extensive time and cost for development. The hardware requirements include signal generation and sensing circuitry, source and sensing coils, as well as a microprocessor capable of undertaking the mathematical operations required by a tracking algorithm. By using components from a previously constructed tracking system, much of this initial development time and effort was avoided and a more direct approach to the testing, analysis and development of a tracking system was undertaken.

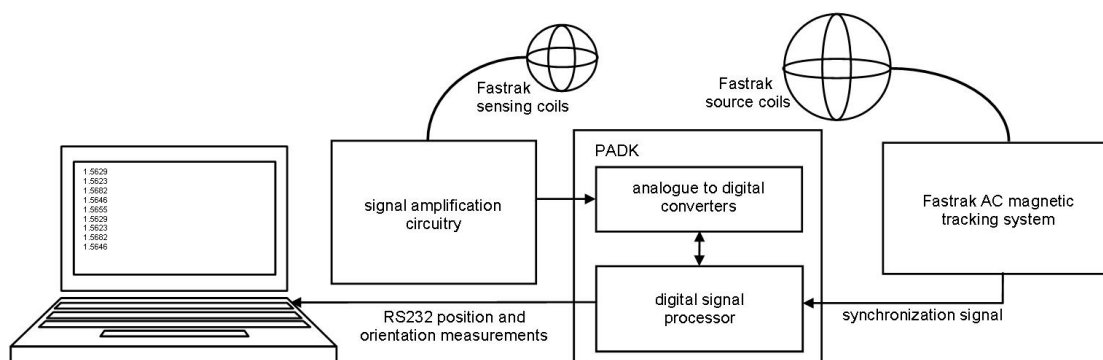


Figure 4.1: System used to interface the professional audio development kit to the Fastrak.

A new tracking system was developed by interfacing a professional audio development kit (PADK) from Lyrtech with a Polhemus Fastrak. The Fastrak was used to generate magnetic fields which were synchronously detected by the PADK using preconstructed sensing coils from the Fastrak as shown in Figure 4.1. The PADK contained a digital signal processor

(DSP) and several precision ADCs capable of accurately sampling an analogue signal at frequencies within the range of tracking operation (0 - 20 kHz). Thus the only hardware required for construction was the signal amplification circuitry which interfaced a set of sensing coils to the PADK.

4.1.1 Signal Amplification, Sampling and Processing

Figure 4.2 is a circuit diagram of a single channel of the detection, amplification, and sampling method used to measure the magnetic fields generated by the Fastrak. A precision wound four coil receiver was connected by a six metre shielded cable to a custom printed circuit board (PCB) containing a three channel amplification and protection system similar to the Fastrak. An RCA connector was used to connect each of the three amplification channels on the PCB to the PADK where biasing and matching techniques interfaced each signal to one channel of a four channel ADC.

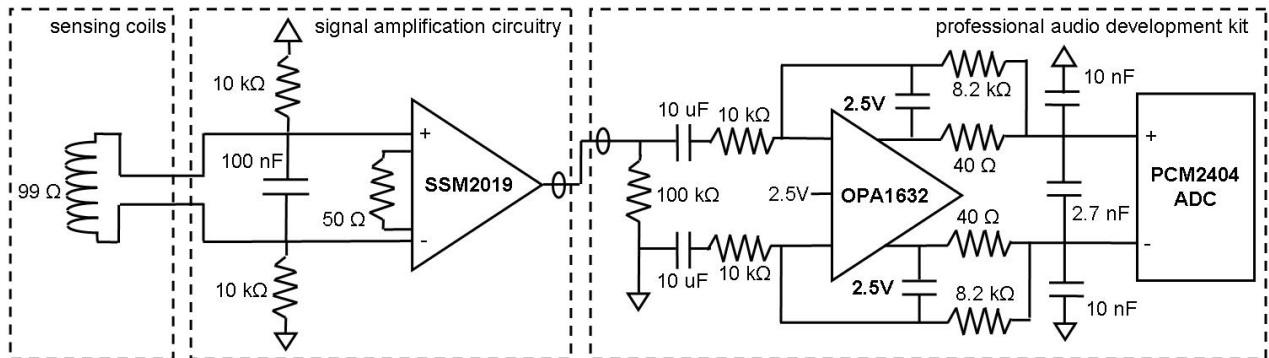


Figure 4.2: Signal sensing circuitry used to detect magnetic fields.

Each inductive coil was interfaced to an SSM2019 instrumentation amplifier with two grounded 10 k Ω resistors to prevent the detected signal from drifting across the voltage range. A capacitor was used to filter unwanted high frequency signals from the instrumentation amplifier. The signal detection circuitry interfaced the PCB to the sensor connector shielding, but did not use a calibration scheme through the fourth coil or use the calibration data located within an IC in the sensor connector - it is anticipated that significant improvements to the measurement scheme may be made by using these methods. The voltage induced on each of the three coils was amplified by a gain of 200, set by a 50 Ω external resistor on the SSM2019 instrumentation amplifier and output voltage limited to $\pm 5\text{V}$ by an SP720AB diode array (not shown).

Each analogue signal was sampled by a 24 bit PCM4204 ADC at 96 kHz and transferred to a floating point Texas Instruments TMS320C6727 DSP via a multiple channel audio serial port (McASP) as shown in Figure 4.3. The configuration of the ADC to DSP interface allowed the sampled data to be transferred into memory via both direct memory access and polled sampling, the latter of which was used to transfer data. A sampling window comprised of the measured signals from the three source coil excitations was taken from each of the three channels simultaneously and separated into a signal set of nine independent measurements as shown in Figure 4.4. Each signal set was processed within the DSP and the position and orientation values were calculated and relayed to a remote computer via a serial RS232 connection where a terminal application was used to view the continuously streaming data.

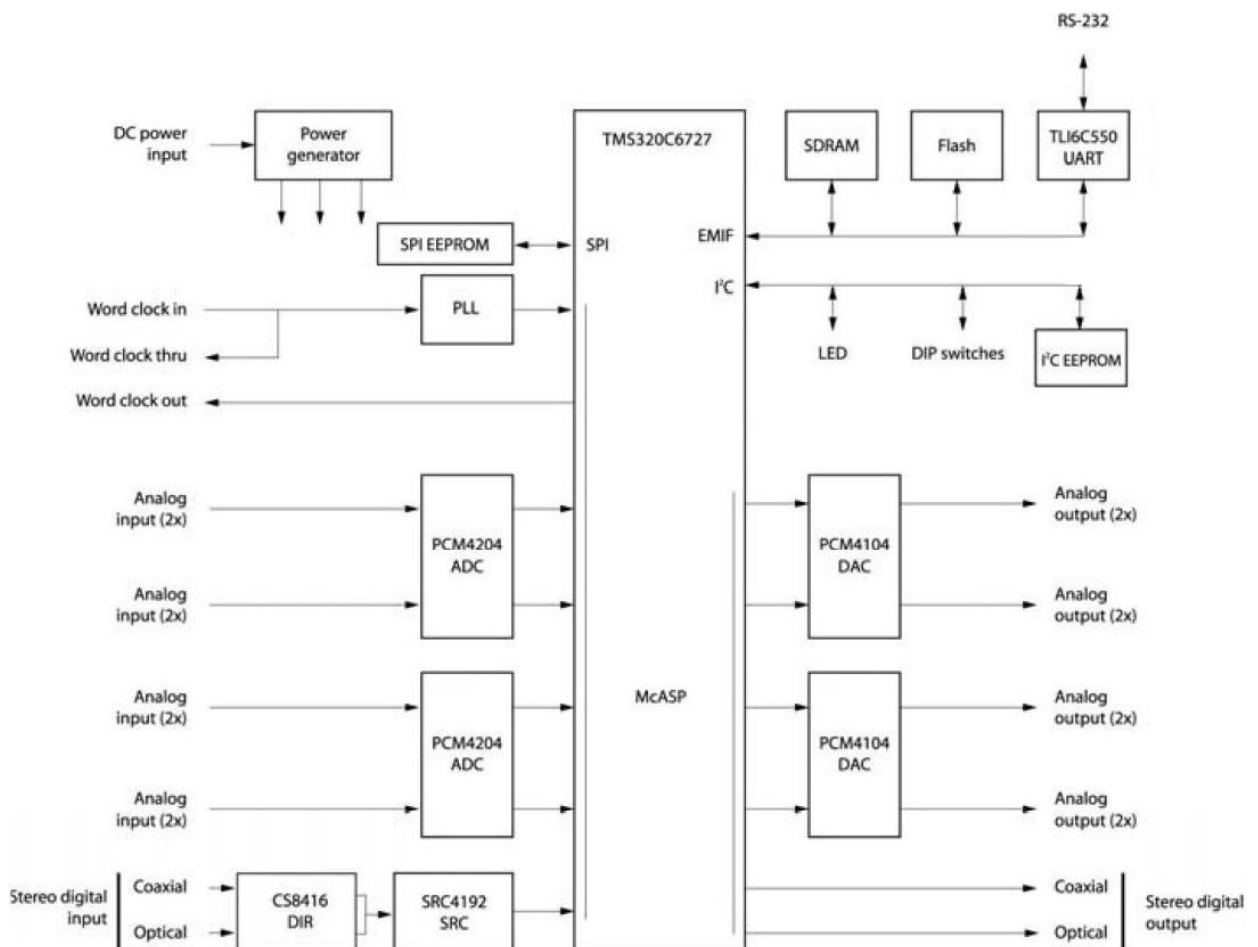


Figure 4.3: Schematic of the PADK development kit used for sampling [Lyrtech (2006)].

4.1.2 System Synchronization

The Polhemus Fastrak provided an external synchronization interface which allowed it to operate as either a ‘master’ providing a ‘Sync Out’ signal at the completion of each new measurement or a ‘slave’ allowing each new measurement to be initiated by a ‘Sync In’ signal. Initially, the Fastrak was configured as a slave, initiating new measurements (thereby generating magnetic fields) at the instruction of the PADK. However, significant timing jitter existed between the ‘Sync In’ signal and the generation of magnetic fields caused the sampling window of the PADK to miss the pulses generated by the Fastrak. Operating the Fastrak as a master significantly reduced the timing jitter between the ‘Sync Out’ signal and the generated magnetic fields and allowed the sampling window to accurately capture the generated signals. A looped polling mechanism in the PADK was used to detect the initiation of each ‘Sync Out’ signal indicating that the previous position measurement was complete and that a new measurement was being taken. The code implemented was not optimized for speed and the Fastrak generated multiple measurements while the PADK was processing the acquired data. As a result, the PADK required the polling mechanism implemented in order to synchronize signal detection with the generation of the next group of magnetic fields.

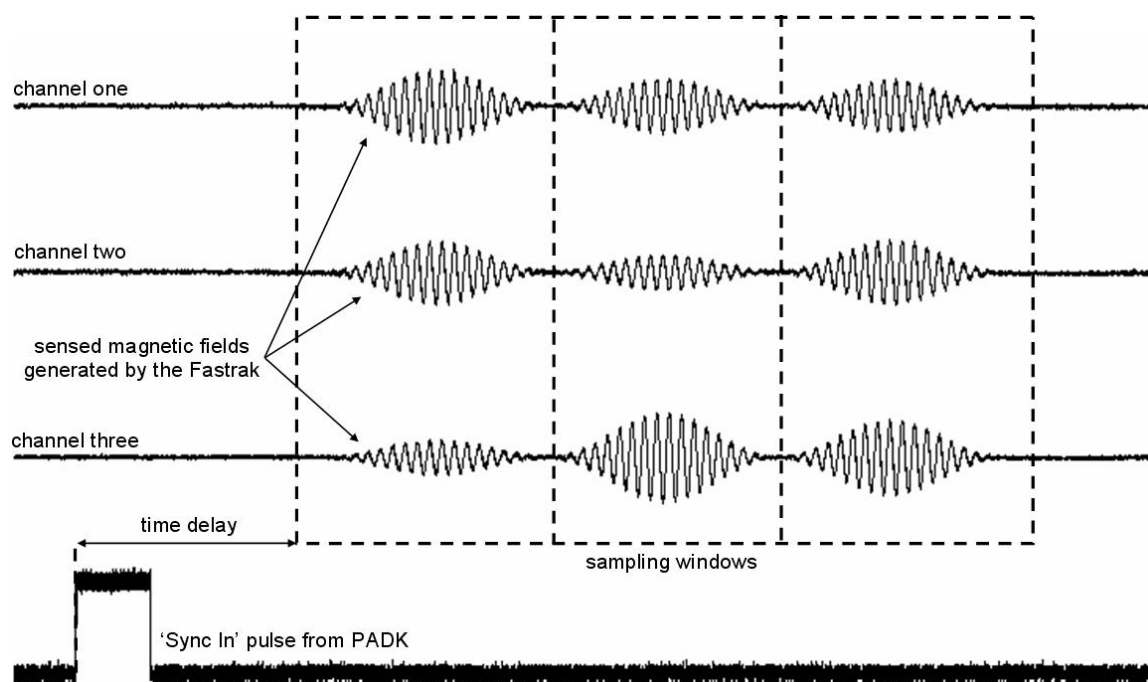


Figure 4.4: Sampling synchronization of the PADK and Fastrak generated magnetic fields.

4.2 Signal Processing and Amplitude Estimation

The amplitude of the voltage signal detected by the ADCs contained both noise and signal distortion. An accurate estimate of the relative signal amplitude s was required. A single pulse of the generated signal may be represented by $p(t)$ as shown in equation 4.1.

$$p(t) = v(t) \sin(2\pi f_e t + \phi) \quad (4.1)$$

where $v(t)$ is a smooth envelope, ϕ is the phase difference between the envelope and the sinusoidal carrier frequency and $f_e(t)$ is the excitation frequency as shown in Figure 4.5.

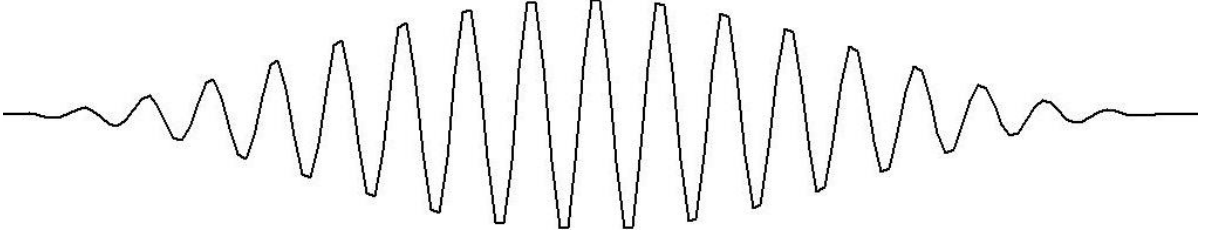


Figure 4.5: Reference template signal used for the generation of magnetic fields.

The signal detected at the source coils contained a number of distorting features including a time delay, envelope distortion, phase distortion and additive noise. If such a signal is detected with delay τ , contains a noise component $\epsilon(t)$ and has an envelope which is distorted to $v'(t)$, then that signal may be modeled by:

$$d(t) = sv'(t + \tau) \sin(2\pi f_e(t + \tau) + \phi) + \epsilon(t + \tau) \quad (4.2)$$

If a sampling frequency $f_s = \frac{1}{T_s}$, which is significantly greater than the Nyquist frequency, is used to sample the signal, then the detected and reference signals can be respectively modeled by:

$$d(nT) = sv'((n + \Delta)T_s) \sin(2\pi f_e(n + \Delta)T_s + \phi) + \epsilon((n + \Delta)T_s) \quad (4.3)$$

$$p(nT) = v(nT_s) \sin(2\pi f_e nT_s + \phi) \quad (4.4)$$

If the envelope distortion is neglected (i.e. $v'(t) \approx v(t)$), then the detected signal may be represented as:

$$\begin{aligned} d(nT) &= sv((n + \Delta)T_s) \sin(2\pi f_e((n + \Delta)T_s) + \phi) + \epsilon((n + \Delta)T_s) \\ &= sp((n + \Delta)T_s) + \epsilon((n + \Delta)T_s) \end{aligned} \quad (4.5)$$

In order to determine the relative amplitude s of the detected signal an accurate estimation technique is required which minimizes the effects of timing error Δ and noise $\epsilon((n + \Delta)T_s)$.

4.3 Frequency Domain Estimation

The frequency domain can be used to accurately estimate the amplitude of the detected signal relative to the generated signal by using the known frequency and envelope characteristics. If the discrete fourier transform (DFT) of the models for the template signal $p(nT)$ and detected signal $d(nT)$ are denoted $P(k)$ and $D(k)$ respectively then the DFT of equation 4.5 may be represented by:

$$D(k) = sP(k)e^{-\frac{j2\pi k\Delta}{N}} + E(k) \quad (4.6)$$

where $D(k)$ contains N samples and $E(k)$ is the DFT of the noise component $\epsilon(t)$. The frequency domain representation of a noisy signal with $f_e = 12$ kHz is illustrated in Figure 4.6.

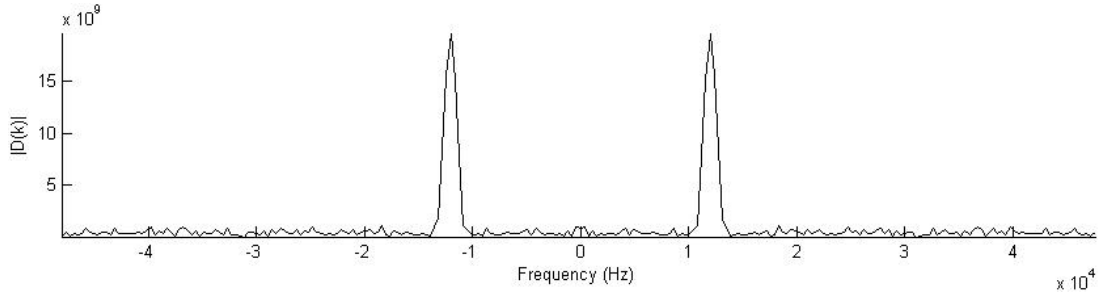


Figure 4.6: Magnitude of the DFT of a noisy signal $D(k)$.

Each new Fastrak measurement was sampled so that each of the nine detected signals were contained within a 512 sample window prior to being converted into the frequency domain using the DFT. Methods of estimating the relative amplitude s using the frequency domain components of the signals are now discussed.

4.3.1 Auto-correlation Estimation

If the signal autocorrelation is undertaken in the time domain as shown in equation 4.7 or the detected signal is multiplied by its conjugate in the frequency domain as shown in equation 4.8, a relationship which may be used to obtain an amplitude estimate is formed.

$$r_{ss}(l) = \sum_{n=0}^{N-1} d(n)d(n+l) \quad (4.7)$$

$$\begin{aligned} R_{ss}(k) &= D(k)D^*(k) \\ &= s^2|P(k)|^2 + sE(k)P^*(k)e^{\frac{j2\pi k\Delta}{N}} + sE^*(k)P(k)e^{-\frac{j2\pi k\Delta}{N}} + |E(k)|^2 \end{aligned} \quad (4.8)$$

Dividing both sides of equation 4.8 by the power of $P(k)$ allows the relative amplitude s to be isolated from the remaining distortion terms as shown in equation 4.9.

$$\frac{R_{ss}(k)}{|P(k)|^2} = s^2 + s\frac{E(k)}{P(k)}e^{\frac{j2\pi k\Delta}{N}} + s\frac{E^*(k)}{P^*(k)}e^{-\frac{j2\pi k\Delta}{N}} + \frac{|E(k)|^2}{|P(k)|^2} \quad (4.9)$$

Although this eliminates the phase dependence from the s^2 term, it is difficult to eliminate the remaining distortion terms from the signal. The resulting calculation for the relative amplitude estimate s_{kac} formed using the k^{th} frequency domain samples in equation 4.10 can cause the distortions to become inherently coupled to the noise estimate, thus:

$$|s_{kac}| = \sqrt{s^2 + s\frac{E(k)}{P(k)}e^{\frac{j2\pi k\Delta}{N}} + s\frac{E^*(k)}{P^*(k)}e^{-\frac{j2\pi k\Delta}{N}} + \frac{|E(k)|^2}{|P(k)|^2}} \quad (4.10)$$

4.3.2 Cross-correlation Estimation

If instead the reference and detected signals are correlated in the time domain (or multiplied element by element in the frequency domain) then the resulting signal is given by $r_{sp}(l)$ in the time domain and $R_{sp}(k)$ in the frequency domain.

$$r_{sp}(l) = \sum_{n=0}^{N-1} d(n)p(n+l) \quad (4.11)$$

$$\begin{aligned} R_{sp}(k) &= D(k)P^*(k) \\ &= s|P(k)|^2e^{-\frac{j2\pi k\Delta}{N}} + E(k)P^*(k) \end{aligned} \quad (4.12)$$

Let s_{kcc} be the relative amplitude of the k^{th} spectral elements calculating using the cross correlation of $D(k)$ and $P^*(k)$. Dividing both sides of equation 4.12 by the power of $P(k)$

produces equation 4.13.

$$\frac{R_{sp}(k)}{|P(k)|^2} = se^{-\frac{j2\pi k\Delta}{N}} + \frac{E(k)}{P(k)} = s_{kcc} \quad (4.13)$$

An alternate but equivalent approach may be taken by directly dividing the spectral components of the detected signal by the corresponding components of the reference spectrum to form the amplitude estimate s_{kd} .

$$\begin{aligned} \frac{D(k)}{P(k)} &= \frac{sP(k)e^{-\frac{j2\pi k\Delta}{N}} + E(k)}{P(k)} \\ &= se^{-\frac{j2\pi k\Delta}{N}} + \frac{E(k)}{P(k)} = s_{kd} = s_{kcc} \end{aligned} \quad (4.14)$$

The resulting measurements of s_{kcc} and s_{kd} both contain real and complex components and without an accurate measure of the phase difference Δ it is difficult to accurately determine s . If the magnitude of either s_{kcc} or s_{kd} is taken as shown in equation 4.15, s may be estimated provided the noise term is small.

$$|s_{kcc}| = \sqrt{s_{kcc}s_{kcc}^*} = \sqrt{s^2 + s\frac{E(k)}{P(k)}e^{\frac{j2\pi k\Delta}{N}} + s\frac{E^*(k)}{P^*(k)}e^{-\frac{j2\pi k\Delta}{N}} + \frac{|E(k)|^2}{|P(k)|^2}} \quad (4.15)$$

Equation 4.15 is equivalent to equation 4.10 and therefore $|s_{kcc}|$, $|s_{kac}|$ and $|s_{kd}|$ are all equal. Given this, the method described in 4.10 was used to determine the magnitude of the relative amplitude for the k^{th} sample corresponding to the carrier frequency of the detected signal and template signals. These methods of amplitude estimation are very similar to previously developed techniques which use the periodogram for amplitude estimation [So (1998)]. If the periodogram of a detected signal $D(k)$ is denoted $I(k)$ then:

$$I(k) = \frac{1}{N}|D(k)|^2 = \frac{1}{N}D(k)D^*(k) \quad (4.16)$$

The periodogram is regarded as a poor method of spectral estimation due to spectral bias resulting from the finite length effects of the detected signal $d(nT_s)$, however these may be eliminated by use of a smoothly varying envelope. It is also important to note that the variance in the noise σ_ϵ is not reduced by increasing the total number of samples N , but can be reduced by averaging multiple spectral samples over which the pulse is spread.

A number of spectral estimation methods exist (e.g. Bartlett and Welch) which allow the

waveform amplitude s to be estimated, however such methods do not use *a priori* knowledge of the frequency and envelope characteristics and do not provide as accurate an estimate as the methods described. The method used to determine the waveform amplitude (equation 4.15) may be further improved by estimating the phase Δ and using equation 4.13 or equation 4.14 to determine s .

4.3.3 Polarity Estimation

The polarity of the detected waveform $d(t)$ may be estimated by using the properties of the envelope of the detected signal. This polarity may be determined by calculating s directly from equation 4.14 which requires that two complex numbers be divided via rationalization of the denominator and assignment of a positive or negative value based on the phase of the frequency domain components $\frac{D(k)}{P(k)}$.

An alternative, but simpler approach to identification of the polarity of the detected signal may be found by determining the polarity of the signal directly from the detected waveform envelope. The time and frequency domain representations for the Hanning window function are shown in equations 4.17 and 4.18.

$$v(n) = 0.5 \left(1 - \cos \left(\frac{2\pi n}{N} \right) \right) \quad (4.17)$$

$$V(k) = -0.25\delta \left(k + \frac{k}{N} \right) + 0.5\delta(k) - 0.25\delta \left(k - \frac{k}{N} \right) \quad (4.18)$$

The polarity of the detected signal may therefore be estimated by determining whether the $V(k)$ is larger than $V(\frac{k}{N})$ and $V(-\frac{k}{N})$, all of which will be scaled by s and degraded by noise $E(k)$ as the waveform envelope forms part of the reference signal $P(k)$ shown in equation 4.6. Thus, because the difference between the spectral components $0.5\delta(k) - (-0.25\delta(-\frac{k}{N}))$ is greater than that of the spectral size of the detected signal $0.5\delta(k)$ this is a more appropriate method of resolving the signal polarity. The modulation of this envelope onto f_e transfers $V(k)$ to another frequency and thus the baseband envelope analysis shown in equation 4.18 must be determined at the k^{th} element corresponding to f_e .

In order to minimize the effects of an incorrectly resolved polarity, a FIFO buffer was used which stored the polarity of the most recently detected signals so that the most common polarity could be used to assign the polarity of s .

4.3.4 Bandlimiting the Signal

If a detected signal contained within a set of N samples and with carrier frequency f_e is sampled at f_s and transformed into the discrete frequency domain, the spectral peak will occur at the i^{th} bin in the discrete spectrum. The value of i may be calculated using:

$$i = \frac{N f_e}{2 f_s} = \frac{512 \cdot 12 \times 10^3}{2 \cdot 96 \times 10^3} = 32 \quad (4.19)$$

A pulse bandwidth tradeoff exists when estimating the relative amplitude of the signal s . As the spectral width corresponding to the envelope increases, the number of samples over which an average may be taken increases, but so too does the noise contribution. Similarly if the envelope bandwidth decreases, the number of samples over which the amplitude estimate can be averaged decreases, but the noise term also decreases.

The implemented tracking system received and interpreted a modulated pulse signal generated by the Fastrak, and as such did not control the form of the pulse envelope. The detected envelope appeared to closely match the characteristics of the Hanning window as shown in Figure 4.7. Some envelope distortion may have occurred during the excitation of the envelope due to the resonant circuits, however only the form of the detected signal is relevant as it is the detected envelope that will be transferred into the frequency domain and analyzed.

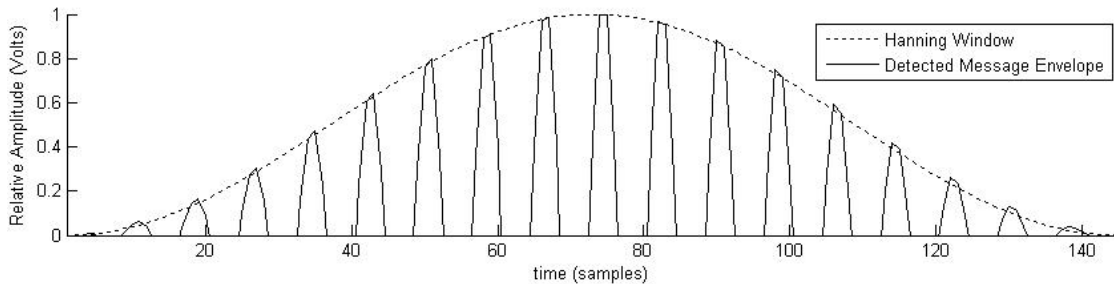


Figure 4.7: Comparison between the detected pulse envelope and a window function.

Each signal was sampled at 96 kHz and contained within a 512 sample window, the significant components for which were contained within five spectral samples. Using all of the spectral components within this frequency range allowed a more accurate estimate of the relative amplitude s to be determined. The spectral components corresponding to the highest and lowest

bins in these frequencies are a and b as shown in equations 4.20 and 4.21.

$$f_{low} = \frac{2af_s}{N} = \frac{2 \cdot 30 \cdot 96 \times 10^3}{512} = 11.250 \times 10^3 \quad (4.20)$$

$$f_{high} = \frac{2bf_s}{N} = \frac{2 \cdot 34 \cdot 96 \times 10^3}{512} = 12.750 \times 10^3 \quad (4.21)$$

4.3.5 Estimation Using Weighted Averaging

The envelope of the detected signal is spread over multiple spectral samples in the discrete frequency domain allowing multiple estimates of the relative amplitude of the detected waveform to be made. If the assumption is made that the noise power spectral density is approximately constant such as is the situation in Figure 4.8, then the effect of the noise component $E(k)$ on each spectral estimate can be made.

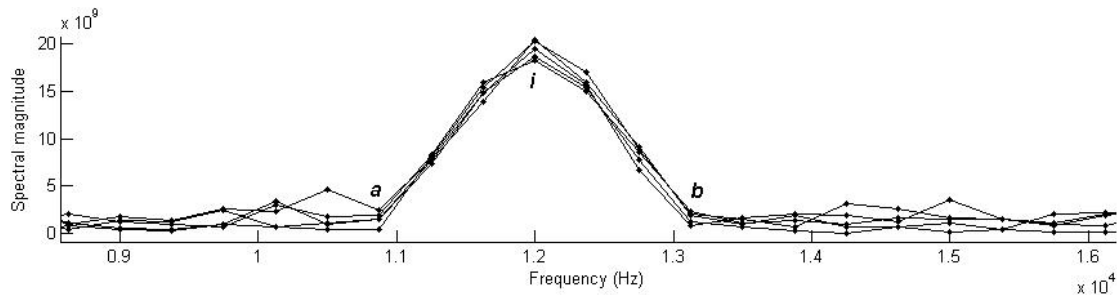


Figure 4.8: FFT of several noisy detected signals.

Equation 4.10 illustrates that if each spectral component contains an equal amount of noise then spectral samples which have a greater magnitude of $P(k)$ will contain less noise error. Therefore by using multiple samples within the bandlimited range between a and b each sample may be weighted according to the magnitude of $P(k)$ corresponding to that frequency as shown in equation 4.22.

$$|s_{estimate}| = \sum_{k=a}^b |s_{kac}| U(k) \quad (4.22)$$

where a is the index of the first spectral sample of the envelope, b is the index of the last spectral sample of the envelope, and s_{kac} is the estimate of the relative amplitude of the detected waveform produced using equation 4.10. The weighting function $U(k)$ may be calculated

according to the magnitude of $P(k)$ as shown:

$$U(k) = \frac{|P(k)|}{\sum_{j=a}^b |P(j)|} \quad (4.23)$$

The resulting coefficients $U(k)$ used to calculate $|s_{estimate}|$ are shown in Table 4.1.

Element number k	30	31	32	33	34
Weight coefficient $U(k)$	0.0590	0.2495	0.3835	0.2482	0.0598

Table 4.1: Weighting coefficients used for amplitude estimation.

4.4 Time Domain Estimation

A narrow-band finite or infinite impulse response filter may be used to resolve the relative amplitude of the detected signal with averaging over a number of measurements. Phase errors may occur, however such phase errors would remain constant as the signal propagation delay would not vary significantly although the interface between the ADC and DAC may cause detectable phase differences.

In order to avoid this, phase alignment techniques may be used after the application of filters to align the reference and detected signals at the zero crossing points of the modulated envelope. Although such an approach may work well for regions in which the SNR is significant, a lower SNR may prevent the detected signal from correct phase alignment with the reference signal causing incorrect estimates to be made. For this reason, frequency domain techniques are more appropriate for the purposes of resolving an amplitude estimate for magnetic fields with a low SNR. Such estimates are significant as low SNR magnetic fields depend on both the range source and sensor coil alignment and thus poor estimates of a low SNR signal may cause significant position and orientation measurement distortion.

4.5 Post Estimation Averaging

If an update rate is used which significantly exceeds the rate of change in position and orientation subsequent estimates may be used to average the amplitude estimates $s_{estimate}$. This does not however, guarantee the elimination of error from the signal as the magnitude of the detected signal may contain spectral bias, however it does allow subsequent estimates to be

smoothed. This method can also cause problems if the polarity of the signal is incorrectly resolved. Averaging a series of detected samples of this nature can significantly skew the average as shown in Figure 4.9.

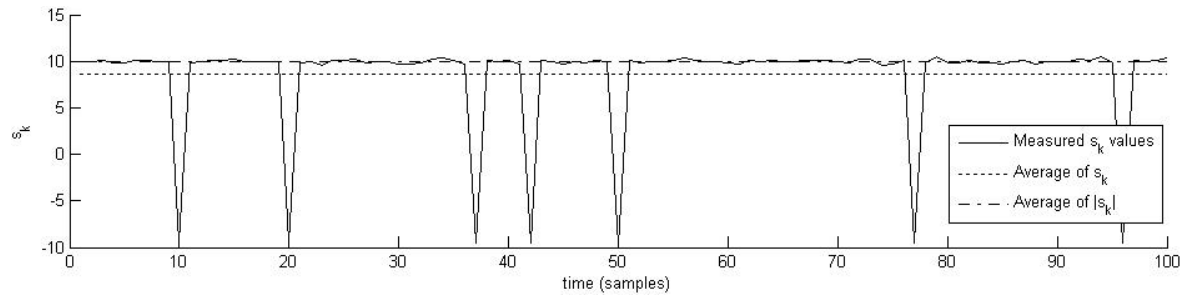


Figure 4.9: Detected signals containing multiple sign errors and the resulting mean.

If instead the magnitude of the signal is averaged and the result is assigned to have the polarity selected according to the majority of the estimates the resulting distortion of the mean can be eliminated. This is inappropriate for signals which are close to zero as the average magnitude can skew the result away from zero in the positive or negative direction as shown in Figure 4.10.

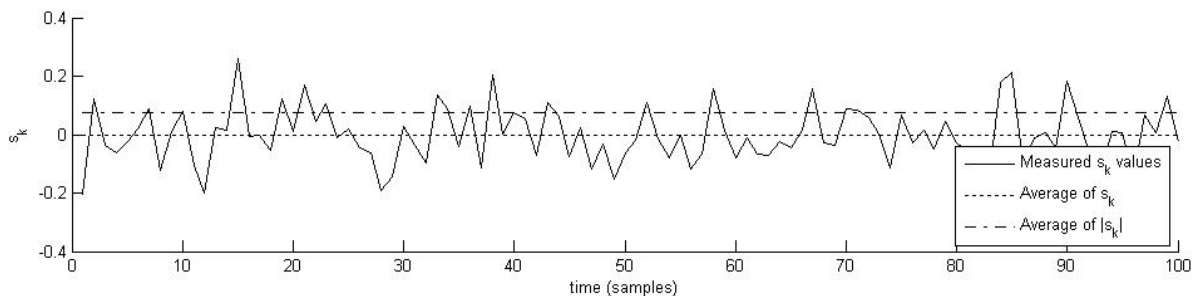


Figure 4.10: Bias error due to averaging the magnitude of small signals.

The most direct solution to solving this problem is to increase the robustness of the polarity estimation so that an averaging process may be implemented. This is difficult for systems which cannot synchronize the signal generation and detection to a high level of accuracy (such as the test jig implemented), however such errors may be significantly reduced or eliminated in a full implementation of an AC magnetic tracking system.

Chapter 5

Estimation of Position and Orientation

The estimation of position and orientation requires an accurate mathematical description of the behavior of magnetic fields which are induced by a coil of wire. The coupled coils analysis in Appendix B presents a method of relating the magnetic field $\mathbf{B}(r, \theta)$ at a point in space to the current I within a thin loop of wire of radius a which induced that field. The relationship developed is shown in equation 5.1 and expresses the magnetic field in terms of spherical coordinates r and θ with respect to the frame of the conducting loop. It is accurate for positions in space for which $r \gg a$.

$$\mathbf{B}(r, \theta) = \frac{\mu_0 m \cos(\theta)}{2\pi r^3} \hat{\mathbf{i}}_r + \frac{\mu_0 m \sin(\theta)}{4\pi r^3} \hat{\mathbf{i}}_\theta \quad (5.1)$$

where μ_0 is the permeability of free space and m ($= \pi a^2 I$) is the magnetic dipole moment. Equation 5.1 is valid for stationary magnetic fields but can also be applied to time varying magnetic fields as long as the frequency of oscillation is sufficiently low. The time variation in the generated magnetic field may be expressed in terms of a sinusoidal function oscillating at frequency ω with phase shift ϕ and an envelope function $v(t)$ which varies slowly compared to ω as shown in equation 5.2.

$$\mathbf{B}(r, \theta, t) = \mathbf{B}(r, \theta) v(t) \sin(\omega t + \phi) \quad (5.2)$$

A measurement of the relative position and orientation of an object in space may be determined by using three mutually orthogonal ‘source coils’ centered in a single frame of reference defined as the *source frame* and three mutually orthogonal ‘sensor coils’ centered in another frame of reference defined as the *sensor frame*. The relative position and orientation of the sensor frame with respect to the source frame may be described by using six independent variables - the source frame position coordinates x , y and z , and the Euler angles of rotation

α , β and γ which represent rotations about the x, y and z source frame axes. If each of the three source coils generates a magnetic field which may be uniquely identified by each of the three sensor coils, a total of nine magnetic field measurements may be made. Although the magnetic fields generated by the source coils vary in time, a scalar constant Λ may be used to relate $\mathbf{B}(r, \theta)$ to the amplitude estimate s . Faraday's Law of electromagnetic induction allows the voltage induced across a sensor coil containing N turns to be related to the change in magnetic field passing through that loop as shown in equation 5.3.

$$\varepsilon = -N \frac{\partial \int \mathbf{B}(r, \theta, t) \cdot d\mathbf{A}}{\partial t} \quad (5.3)$$

where \mathbf{A} is a vector directed perpendicular to the plane of the loop with a magnitude equal to the cross sectional area of the sensor coil, \mathbf{A} , and $\mathbf{B}(r, \theta, t)$ is the magnetic field at the sensor position. If the magnetic field component perpendicular to a sensor coil is denoted $B_{\perp} \sin(\omega t + \phi)$ then equation 5.3 may be simplified.

$$\begin{aligned} \varepsilon &= -NA \frac{\partial B_{\perp} v(t) \sin(\omega t + \phi)}{\partial t} \\ &= -NAB_{\perp} \omega v(t) \cos(\omega t + \phi) - NAB_{\perp} \sin(\omega t + \phi) \frac{\partial v(t)}{\partial t} \\ &\approx -NAB_{\perp} \omega v(t) \cos(\omega t + \phi) \end{aligned} \quad (5.4)$$

Equation 5.4 illustrates that although the amplitude estimate s is calculated from the derivative of the magnetic field $\mathbf{B}(r, \theta, t)$, frequency domain estimation will allow s to be directly related to the magnetic field detected by a sensor coil. Thus:

$$s = \Lambda B_{\perp} \quad (5.5)$$

where the scalar constant Λ represents the change in magnitude resulting from the ideal conversion of a magnetic field passing through the sensor coil into a dimensionless amplitude estimate s using the estimation technique expressed in equation 4.10.

5.1 Resolution of Position Magnitude

The sensor is constructed from three orthogonal coils so that each coil will measure a different magnetic field component allowing the magnitude and direction of the magnetic field at the sensor position to be determined in the sensor frame. The magnitude of the magnetic field

during a given source coil excitation may be calculated from equation 5.1 as:

$$|\mathbf{B}_Z| = \sqrt{\left(\frac{\mu_0 m \cos(\theta)}{2\pi r^3}\right)^2 + \left(\frac{\mu_0 m \sin(\theta)}{4\pi r^3}\right)^2} \quad (5.6)$$

where \mathbf{B}_Z is the magnetic field at the sensor location during the z source coil excitation. If each of the three mutually orthogonal sensor coils detect an orthogonal magnetic field component, then the sum of the squares of the detected magnetic fields will be equal to $|\mathbf{B}_Z|^2$ which will be invariant of the sensor orientation. Equation 5.6 can therefore be rearranged in terms of $\cos(\theta)$ as:

$$\cos(\theta) = \pm \sqrt{\frac{1}{3} \left(\left(\frac{|\mathbf{B}_Z| 4\pi r^3}{\mu_0 m} \right)^2 - 1 \right)} \quad (5.7)$$

where θ is the angle between the z axis perpendicular to the plane of the z source coil and the direction of the sensor position. It is therefore apparent that $\cos(\theta)$ may be expressed as the fractional projection of the sensor position onto the z axis of the source frame as shown in equation 5.8 and illustrated in Figure 5.1(a).

$$\frac{z}{r} = \pm \sqrt{\frac{1}{3} \left(\left(\frac{|\mathbf{B}_Z| 4\pi r^3}{\mu_0 m} \right)^2 - 1 \right)} \quad (5.8)$$

where z is the sensor position coordinate in the source frame. The use of the magnetic field magnitude to calculate the sensor position may also be considered intuitively. The magnetic field generated by each source coil will be constant over a surface in space and thus by calculating the magnitude of the magnetic field during a source coil excitation, the sensor position is resolved to a point on that surface. If each coil is excited sequentially, three different surfaces will be formed all of which will intersect at common points, one of which is the sensor position. The symmetry of the source coils will cause one point of intersection to exist in each octant of the source frame and thus the magnitude of the position coordinates ($|x|, |y|, |z|$) may be determined. An illustration of this is shown in Figure 5.1(b).

This method of resolving the position coordinate may also be applied to the x and y source coils allowing the magnitude of the x, y and z position coordinates to be expressed as shown in equations 5.9, 5.10 and 5.11.

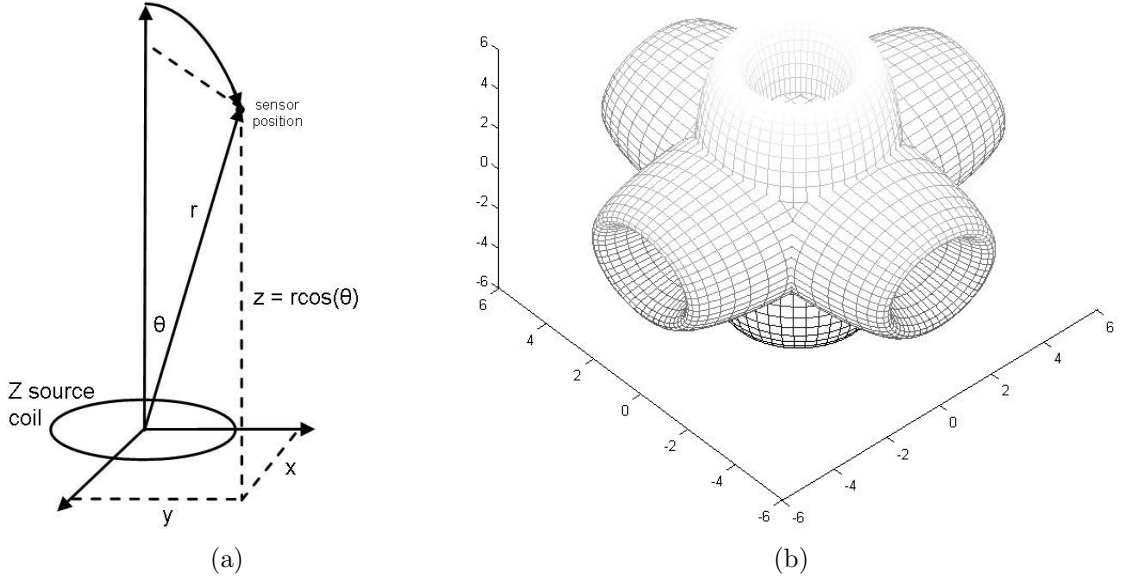


Figure 5.1: (a) Sensor position with respect to the z source frame in terms of spherical coordinates r and θ , (b) Three magnetic field constant magnitude surfaces generated by three orthogonal source coils.

$$x = \pm r \sqrt{\frac{1}{3} \left(\left(\frac{|\mathbf{B}_{XD}| 4\pi r^3}{\mu_0 m} \right)^2 - 1 \right)} \quad (5.9)$$

$$y = \pm r \sqrt{\frac{1}{3} \left(\left(\frac{|\mathbf{B}_{YD}| 4\pi r^3}{\mu_0 m} \right)^2 - 1 \right)} \quad (5.10)$$

$$z = \pm r \sqrt{\frac{1}{3} \left(\left(\frac{|\mathbf{B}_{ZD}| 4\pi r^3}{\mu_0 m} \right)^2 - 1 \right)} \quad (5.11)$$

where $|\mathbf{B}_{XD}|$, $|\mathbf{B}_{YD}|$, and $|\mathbf{B}_{ZD}|$ are the magnetic field magnitudes detected when the x, y, and z source coils are excited. The resulting magnitude of the magnetic field detected by the three sensor coils during a source coil excitation will be independent of the sensor orientation and may be calculated using equations 5.12, 5.13 and 5.14.

$$|\mathbf{B}_{XD}| = \sqrt{B_{XxD}^2 + B_{XyD}^2 + B_{XzD}^2} \quad (5.12)$$

$$|\mathbf{B}_{YD}| = \sqrt{B_{YxD}^2 + B_{YyD}^2 + B_{YzD}^2} \quad (5.13)$$

$$|\mathbf{B}_{ZD}| = \sqrt{B_{ZxD}^2 + B_{ZyD}^2 + B_{ZzD}^2} \quad (5.14)$$

where B_{XxD} , B_{XyD} and B_{XzD} represent the magnetic field detected on the x, y and z sensor

coils, when the x source coil is excited.

If equations 5.9, 5.10, and 5.11 are substituted into Pythagoras' theorem, the range r may be calculated by using equation 5.15.

$$r = \sqrt{x^2 + y^2 + z^2} = \sqrt[6]{6 \left(\frac{\mu_0 m}{4\pi} \right)^2 \frac{1}{|\mathbf{B}_{XD}|^2 + |\mathbf{B}_{YD}|^2 + |\mathbf{B}_{ZD}|^2}} \quad (5.15)$$

The calculation of r can be made directly from the detected magnetic fields and may therefore be used to calculate the sensor position coordinates in equations 5.9, 5.10 and 5.11.

5.2 Resolution of Sensor Orientation

The orientation of the sensor relative to the source frame may be resolved by comparing the set of nine detected magnetic field measurements to the set of nine predicted field measurements that a sensor would detect if it had an identical orientation to the source. If B_D and B_P are 3×3 matrices that represent the set of nine detected and predicted magnetic fields respectively then the rotation required to rotate B_P to match B_D may be resolved using either quaternions or rotation matrices. The three rows in the B_D and B_P matrices represent the x, y, and z source coil excitations, while the three columns represent the x, y and z sensor coil measurements as defined in the equations in 5.16.

$$B_D = \begin{bmatrix} B_{XxD} & B_{XyD} & B_{XzD} \\ B_{YxD} & B_{YyD} & B_{YzD} \\ B_{ZxD} & B_{ZyD} & B_{ZzD} \end{bmatrix} \quad B_P = \begin{bmatrix} B_{XxP} & B_{XyP} & B_{XzP} \\ B_{YxP} & B_{YyP} & B_{YzP} \\ B_{ZxP} & B_{ZyP} & B_{ZzP} \end{bmatrix} \quad (5.16)$$

5.2.1 Magnetic Field Prediction

The magnetic fields at a point in space may be predicted by using equation 5.1 however a more useful method of calculating the magnetic fields may be determined if the magnetic field is converted into rectangular coordinates. If the magnetic field components B_r and B_θ are defined as shown in equation 5.17, then the magnetic field at a point in space may be represented by \mathbf{B} as shown in equation 5.18.

$$B_r = \frac{\mu_0 m \cos(\theta)}{2\pi r^3} \quad B_\theta = \frac{\mu_0 m \sin(\theta)}{4\pi r^3} \quad (5.17)$$

5. ESTIMATION OF POSITION AND ORIENTATION

$$\mathbf{B} = B_r \hat{\mathbf{i}}_r + B_\theta \hat{\mathbf{i}}_\theta \quad (5.18)$$

Figure 5.2 illustrates the direction and magnitude of each magnetic field component in terms of the spherical coordinates r and θ .

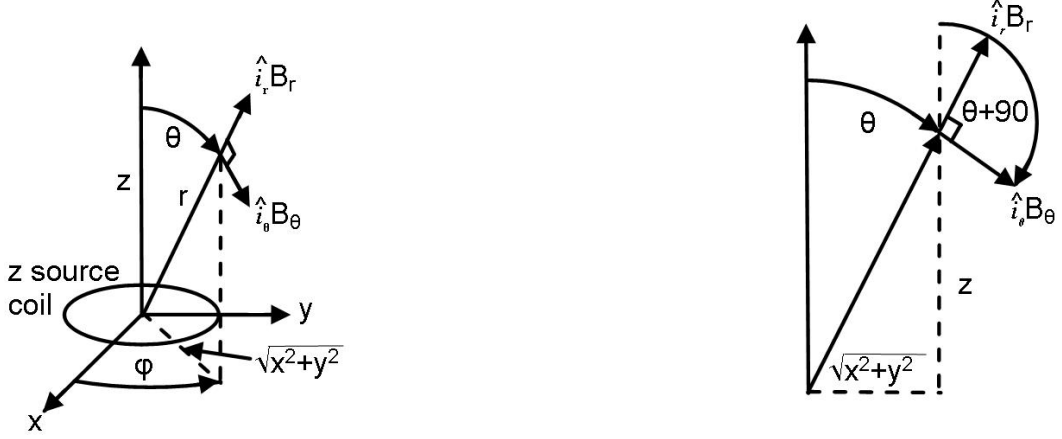


Figure 5.2: Magnetic field components in terms of rectangular and spherical coordinates.

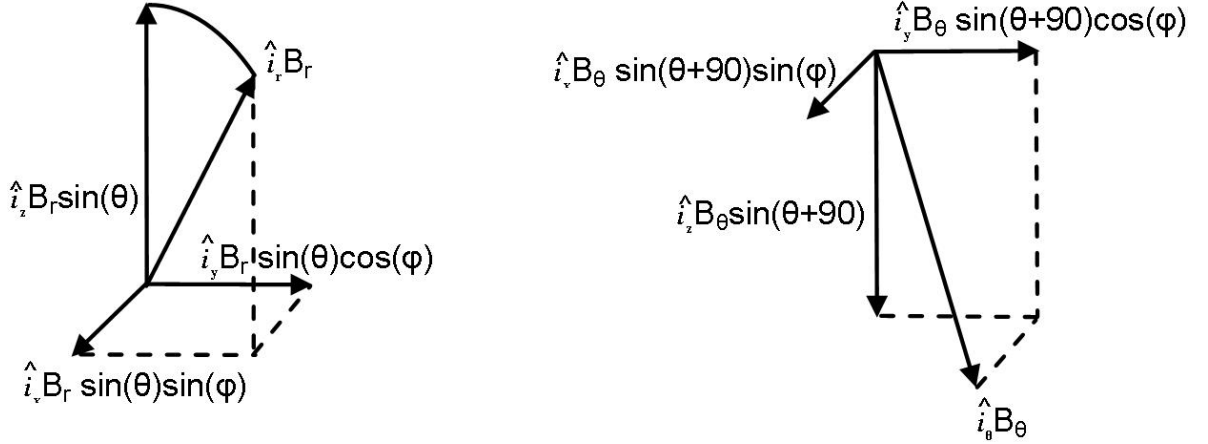


Figure 5.3: Projection of B_r and B_θ onto the rectangular coordinate system.

The projection of each magnetic field onto the x , y and z source frame axes are shown in Figure 5.3. The coordinate transformations required to convert a magnetic field component B from spherical into cartesian coordinates may be calculated by using the standard transformations of equation 5.19.

$$B_x \hat{\mathbf{i}}_x = B \sin(\theta) \cos(\phi) \hat{\mathbf{i}}_x \quad B_y \hat{\mathbf{i}}_y = B \sin(\theta) \sin(\phi) \hat{\mathbf{i}}_y \quad B_z \hat{\mathbf{i}}_z = B \cos(\theta) \hat{\mathbf{i}}_z \quad (5.19)$$

These transformations may be applied to both the B_r and B_θ components allowing the magnetic field induced by a z source coil to be calculated in rectangular coordinates as shown in equations 5.20, 5.21 and 5.22.

$$B_{Zx}\hat{\mathbf{i}}_x = B_r \sin(\theta) \cos(\phi)\hat{\mathbf{i}}_x + B_\theta \sin(\theta + 90) \cos(\phi)\hat{\mathbf{i}}_x \quad (5.20)$$

$$B_{Zy}\hat{\mathbf{i}}_y = B_r \sin(\theta) \sin(\phi)\hat{\mathbf{i}}_y + B_\theta \sin(\theta + 90) \sin(\phi)\hat{\mathbf{i}}_y \quad (5.21)$$

$$B_{Zz}\hat{\mathbf{i}}_z = B_r \cos(\theta)\hat{\mathbf{i}}_z + B_\theta \cos(\theta + 90)\hat{\mathbf{i}}_z \quad (5.22)$$

This can be simplified further as the spherical coordinates r and θ may be converted into the x , y and z rectangular coordinates by using trigonometry as shown in equations 5.23 and 5.24.

$$\theta = \cos^{-1}\left(\frac{z}{r}\right) = \sin^{-1}\left(\frac{\sqrt{x^2 + y^2}}{r}\right) \quad (5.23)$$

$$\phi = \tan^{-1}\left(\frac{y}{x}\right) = \cos^{-1}\left(\frac{x}{\sqrt{x^2 + y^2}}\right) = \sin^{-1}\left(\frac{y}{\sqrt{x^2 + y^2}}\right) \quad (5.24)$$

By applying the rectangular equivalent of r and θ to equations 5.20, 5.21 and 5.22 the magnetic fields can be expressed as shown.

$$B_{Zx}\hat{\mathbf{i}}_x = B_r \frac{x}{r}\hat{\mathbf{i}}_x + B_\theta \frac{zx}{r\sqrt{x^2 + y^2}}\hat{\mathbf{i}}_x \quad (5.25)$$

$$B_{Zy}\hat{\mathbf{i}}_y = B_r \frac{y}{r}\hat{\mathbf{i}}_y + B_\theta \frac{zy}{r\sqrt{x^2 + y^2}}\hat{\mathbf{i}}_y \quad (5.26)$$

$$B_{Zz}\hat{\mathbf{i}}_z = B_r \frac{z}{r}\hat{\mathbf{i}}_z - B_\theta \frac{\sqrt{x^2 + y^2}}{r}\hat{\mathbf{i}}_z \quad (5.27)$$

If the definitions of B_r and B_θ are substituted into equations 5.25, 5.26 and 5.27 then the magnetic field may be expressed in terms of the rectangular coordinates of the source frame.

$$B_{Zx}\hat{\mathbf{i}}_x = \frac{3\mu_0 m}{4\pi r^3} \frac{zx}{r^2}\hat{\mathbf{i}}_x \quad (5.28)$$

$$B_{Zy}\hat{\mathbf{i}}_y = \frac{3\mu_0 m}{4\pi r^3} \frac{zy}{r^2}\hat{\mathbf{i}}_y \quad (5.29)$$

$$B_{Zz}\hat{\mathbf{i}}_z = \frac{\mu_0 m}{2\pi r^3} \frac{z^2}{r^2}\hat{\mathbf{i}}_z - \frac{\mu_0 m}{4\pi r^3} \frac{x^2 + y^2}{r^2}\hat{\mathbf{i}}_z \quad (5.30)$$

The rectangular coordinates from which these magnetic fields have been calculated may be applied according to the orientation of each source coil as shown in Figure 5.4. This allows the frame of each source coil to be defined with respect to the frame of the source so that the

5. ESTIMATION OF POSITION AND ORIENTATION

predicted magnetic fields can be calculated with respect to the same frame of reference.

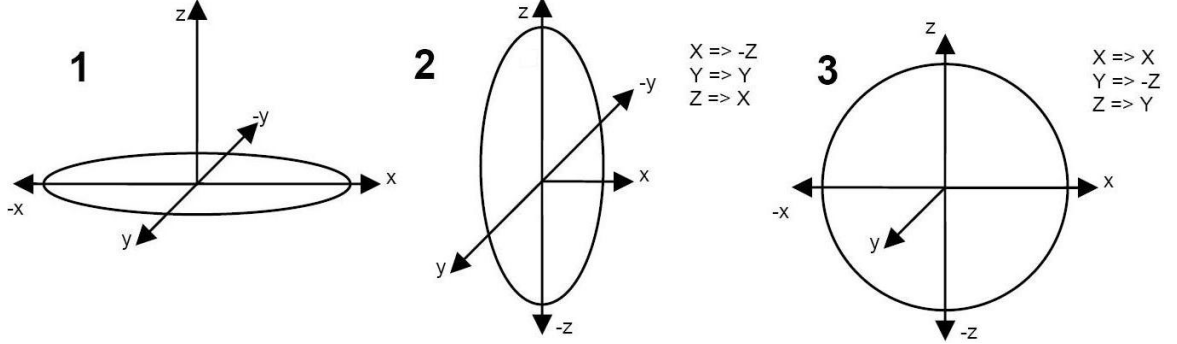


Figure 5.4: Mutually perpendicular coil orientations.

The predicted magnetic fields may therefore be calculated in the frame of the source using equations 5.31, 5.32 and 5.33.

$$\begin{aligned}
 B_{XxP} &= \frac{\mu_0 m}{2\pi r^3} \frac{x^2}{r^2} - \frac{\mu_0 m}{4\pi r^3} \frac{z^2 + y^2}{r^2} \\
 B_{XyP} &= \frac{3\mu_0 m}{4\pi r^3} \frac{xy}{r^2} \\
 B_{XzP} &= \frac{3\mu_0 m}{4\pi r^3} \frac{xz}{r^2}
 \end{aligned} \tag{5.31}$$

$$\begin{aligned}
 B_{YxP} &= \frac{3\mu_0 m}{4\pi r^3} \frac{yx}{r^2} \\
 B_{YyP} &= \frac{\mu_0 m}{2\pi r^3} \frac{y^2}{r^2} - \frac{\mu_0 m}{4\pi r^3} \frac{x^2 + z^2}{r^2} \\
 B_{YzP} &= \frac{3\mu_0 m}{4\pi r^3} \frac{yz}{r^2}
 \end{aligned} \tag{5.32}$$

$$\begin{aligned}
 B_{ZxP} &= \frac{3\mu_0 m}{4\pi r^3} \frac{zx}{r^2} \\
 B_{ZyP} &= \frac{3\mu_0 m}{4\pi r^3} \frac{zy}{r^2} \\
 B_{ZzP} &= \frac{\mu_0 m}{2\pi r^3} \frac{z^2}{r^2} - \frac{\mu_0 m}{4\pi r^3} \frac{x^2 + y^2}{r^2}
 \end{aligned} \tag{5.33}$$

where B_{XyP} represents the magnetic field predicted to be detected by the y sensor coil when the x source coil is excited and the sensor is located at a the position (x,y,z) with the same orientation as the source.

The predicted magnetic fields are based on the x, y, and z sensor position coordinates which are resolved using the detected magnetic fields. The predicted magnetic fields may therefore be directly determined from the detected magnetic fields.

5.2.2 Euler Angle Resolution

The 3×3 matrices B_P and B_D represent the magnetic fields that are predicted to be detected and those that are detected by a sensor at a given location. If the predicted magnetic fields are accurate, then B_P will differ from B_D only by the rotation of the sensor frame which may be represented by a rotation matrix R as shown in equation 5.34.

$$B_D = RB_P \quad (5.34)$$

The rotation matrix R is a 3×3 matrix which rotates the frame of the source into that of the sensor by a sequence of three rotations γ , β , and α about the x, y_γ and $z_{\gamma\beta}$ axes. The y_γ axis represents the y axis in the sensor frame after rotation through angle γ about the x axis while $z_{\gamma\beta}$ represents the z axis after a subsequent rotation through angle β about y_γ . The relationship between the rotation matrix R and the Euler angles is shown in equation 5.36.

$$R = \begin{bmatrix} \cos(\gamma) \cos(\beta) & \sin(\gamma) \cos(\alpha) + \cos(\gamma) \sin(\beta) \sin(\alpha) & \sin(\gamma) \sin(\alpha) - \cos(\gamma) \sin(\beta) \cos(\alpha) \\ -\sin(\gamma) \cos(\beta) & \cos(\gamma) \cos(\alpha) - \sin(\gamma) \sin(\beta) \sin(\alpha) & \cos(\gamma) \sin(\alpha) + \sin(\gamma) \sin(\beta) \cos(\alpha) \\ \sin(\beta) & -\sin(\alpha) \cos(\beta) & \cos(\alpha) \cos(\beta) \end{bmatrix}$$

$$= R_\gamma R_\beta R_\alpha \quad (5.35)$$

$$= R(\alpha, \beta, \gamma) \quad (5.36)$$

where R_α , R_β and R_γ are 3×3 rotation matrices which rotate the coordinate frame about the axes of the preceding frame by the angles γ , β and α respectively.

$$R_\alpha = \begin{bmatrix} 1 & 0 & 0 \\ 0 & \cos(\alpha) & \sin(\alpha) \\ 0 & -\sin(\alpha) & \cos(\alpha) \end{bmatrix}, \quad R_\beta = \begin{bmatrix} \cos(\beta) & 0 & -\sin(\beta) \\ 0 & 1 & 0 \\ \sin(\beta) & 0 & \cos(\beta) \end{bmatrix}, \quad R_\gamma = \begin{bmatrix} \cos(\gamma) & \sin(\gamma) & 0 \\ -\sin(\gamma) & \cos(\gamma) & 0 \\ 0 & 0 & 1 \end{bmatrix}$$

If the position of the sensor is known and the predicted magnetic fields B_P can be accurately calculated, then the rotation matrix R can be determined by equation 5.37 as long as B_P remains nonsingular.

$$R = B_D B_P^{-1} \quad (5.37)$$

Previously developed methods [Slabaugh (1999)] may be used to resolve each of the angles of rotation however the order of rotation must not be changed. Multiple rotation sequences will exist due to the trigonometric ambiguity of the $\sin(x)$ function, as shown in equations 5.38, 5.39 and 5.40.

$$\beta_1 = \sin^{-1}(R(3, 1)), \quad \beta_2 = \pi - \beta_1 \quad (5.38)$$

$$\alpha_1 = \operatorname{atan2}\left(\frac{R(3, 2)}{\cos(\beta_1)}, \frac{R(3, 3)}{\cos(\beta_1)}\right), \quad \alpha_2 = \operatorname{atan2}\left(\frac{R(3, 2)}{\cos(\beta_2)}, \frac{R(3, 3)}{\cos(\beta_2)}\right) \quad (5.39)$$

$$\gamma_1 = \operatorname{atan2}\left(\frac{R(2, 1)}{\cos(\beta_1)}, \frac{R(1, 1)}{\cos(\beta_1)}\right), \quad \gamma_2 = \operatorname{atan2}\left(\frac{R(2, 1)}{\cos(\beta_2)}, \frac{R(1, 1)}{\cos(\beta_2)}\right) \quad (5.40)$$

where $\operatorname{atan2}(y, x)$ is an arctangent function which uses the sign of both x and y to determine the quadrant of the angle calculated from $\operatorname{atan}(\frac{y}{x})$. These methods are ineffective in situations for which $\beta = \frac{\pi}{2}$, or $\beta = \frac{3\pi}{2}$, as R simplifies to:

$$R = \begin{bmatrix} 0 & -\sin(\alpha + \gamma) & -\cos(\alpha + \gamma) \\ 0 & \cos(\alpha + \gamma) & -\sin(\alpha + \gamma) \\ 1 & 0 & 0 \end{bmatrix}, \quad (5.41)$$

Although α and γ may be related by equation 5.42 an infinite number of solutions will exist.

$$\alpha = \gamma - \operatorname{atan2}(R(1, 2), R(1, 3)) \quad (5.42)$$

This phenomena which is known as ‘gimbal lock’ and cannot be resolved. Quaternion rotation does not suffer from such effects and may be used to resolve the sensor orientation without such discontinuities.

5.2.3 Resolving Position Polarity

Section 5.1 presents a method of calculating sensor position to one of eight locations. The sensor position cannot be resolved with certainty as the magnetic fields generated by the source will be identical at two locations in the tracking space. This implies that the rotation matrix R in equation 5.34 will not exist for the alternate six positions as no rotation sequence will allow B_P to match B_D . This may be tested by the orthogonality of the resolved rotation matrix R .

Given a sensor that detects magnetic fields B_D and has an orientation that may be represented by R , eight different possibilities exist for the predicted magnetic matrix B_P according

to the eight different possible positions which may be substituted into equations 5.31, 5.32 and 5.33. Consider that an incorrect position is used in the calculation of B_P , thus forming the matrix B'_P , resolved rotation matrix R will not be valid as shown in the following:

$$\begin{aligned} R^T R &= (B_D B'_P{}^{-1})^T (B_D B'_P{}^{-1}) \\ &= (B'_P{}^T)^{-1} B_D^T B_D B'_P{}^{-1} \end{aligned}$$

The detected magnetic fields may be represented by the rotation matrix $B_D = R B_P$ as this describes the *true* orientation of the sensor.

$$\begin{aligned} R^T R &= (B'_P{}^T)^{-1} B'_P{}^T R^T R B_P B'_P{}^{-1} \\ &= (B'_P{}^T)^{-1} B'_P{}^T B_P B'_P{}^{-1} \\ &\neq I \quad \text{unless } B_P = B'_P \end{aligned} \tag{5.43}$$

The predicted signal matrix can therefore only be calculated using one of two sensor locations: the actual sensor position and the position in the octant with the opposite polarity of x and z as shown in Figure 5.5. The remaining six locations will not produce valid rotation matrices and may therefore be discarded as incorrect.

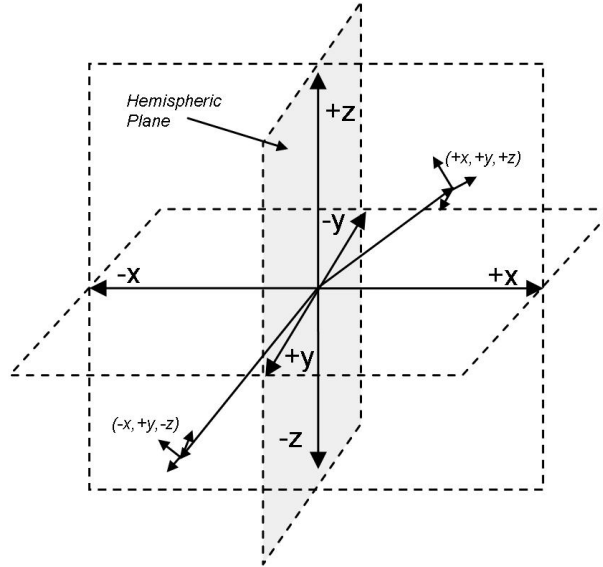


Figure 5.5: Octant regions into which the tracking space is divided.

This method is fragile as it relies on a precise measurement of the sensor position and can be corrupted by noise. It is therefore suggested that a more robust method of position calculation

be determined in future research.

5.2.4 Orientation Continuity

The resolution of the two position (hemispheric) ambiguity requires a reference calibration or an assumption to be made as to which hemisphere the sensor is in. If the sensor is always assumed to retain the same polarity of x , then the incorrect polarity of x and z will be resolved if the sensor moves through the hemispheric plane as shown in Figure 5.5. An estimate may be made as to whether this occurs in order to prevent such errors. If the sensor is positioned on or close to the hemispheric plane and the sensor orientation is known, the orientation can be used by future calculations to identify whether the sensor changes hemisphere. The resolved orientation for the two positions on opposite sides of the hemispheric plane may differ significantly causing a discontinuity at the boundary allowing identification of the correct position.

If a sensor located within an octant in the positive hemisphere $(+x, |y|, |z|)$ moves across the hemispheric plane changing the polarity of x $(-x, |y|, |z|)$, but does not change the polarity of z , then the resolved sensor orientation may differ significantly (or be invalid) under the assumption that the sensor has not changed octant. The positive and negative hemisphere rotation matrices R_+ and R_- produced from a single detected magnetic field matrix B_D , but differing predicted position matrices B_{P+} and B_{P-} can be used to identify the resulting orientation discontinuity as shown in equation 5.44.

$$\begin{aligned} R_{(+,+,+)} - R_{(+,+,-)} &= B_D B_{P+}^{-1} - B_D B_{P-}^{-1} \\ &= B_D (B_{P+}^{-1} - B_{P-}^{-1}) \end{aligned} \tag{5.44}$$

Chapter 6

Calibration

Calibration is the process of adjusting the theoretical models to account for the physical imperfections in the system which distort the resulting position and orientation calculations. The best method of model correction is to take into account the imperfections in each parameter separately and introduce an adjustment factor to alter each parameter to its true value.

An alternative approach could be implemented by using a lookup table to associate the detected magnetic fields with the correct position and orientation. A direct implementation of this method is infeasible as the number of positions and orientations within the tracking space are infinite, however the generation of a distortion ‘map’ of each component may be possible. The disadvantage to such an approach is the significant time required to map the component distortions and the complexity associated with ensuring that the distortion map is restricted solely to the component under test. If each component is not calibrated independently the resulting tracking system will not allow component interchangeability which other systems such as the ‘Fastrak’, ‘Flock of Birds’, and ‘Wintracker’ allow. Figure 6.1 provides a block diagram of the major components which require independent calibration in a coil-based magnetic tracking system.

The tracking environment in which the tracker operates may contain metallic or magnetic objects which distort the magnetic field and which are difficult to accurately model without precise knowledge of the disturbing object. The presence of such objects is therefore considered a limiting factor in magnetic tracking rather than a correctable physical distortion.

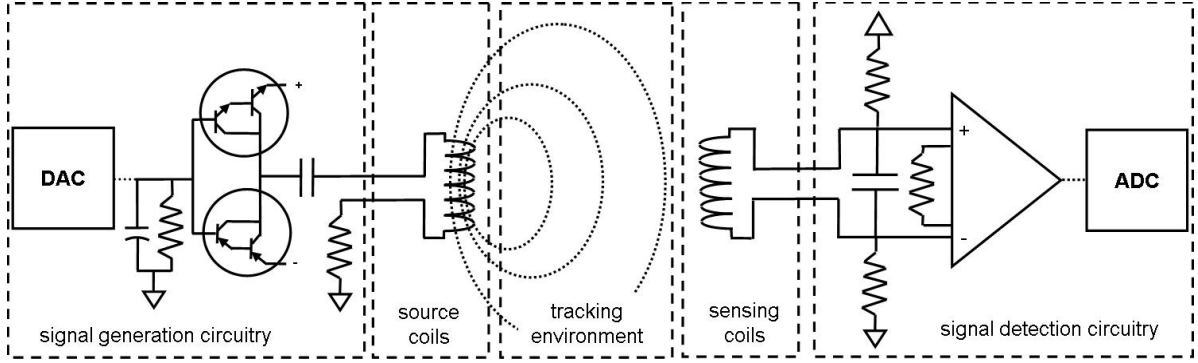


Figure 6.1: Block diagram of the hardware components introducing distortion.

6.1 Sources of Distortion

The following sections outline the primary forms of distortion within an AC magnetic tracking system.

6.1.1 Coil Position Offsets

The sensor and source components within a magnetic tracking system can be constructed from a set of three mutually orthogonal coils and are generally defined as each being concentric about a single separate location. The positions of the three coils used to construct each component may not be perfectly aligned (or ‘non-concentric’) to the specified location of the component and may thus cause the detected signal to appear distorted. Defining a frame of reference containing position offsets for each coil with respect to the ideal source or sensor location allows elimination of the distorting effect. The source position offsets $P_{\Delta X}$, $P_{\Delta Y}$, $P_{\Delta Z}$ defined in equation 6.1 represent the position offsets of the frame of the x, y, and z source coils from the centre of the ideal source position (in the frame of the source).

$$P_{\Delta X} = \begin{bmatrix} \Delta x_X \\ \Delta y_X \\ \Delta z_X \end{bmatrix}, \quad P_{\Delta Y} = \begin{bmatrix} \Delta x_Y \\ \Delta y_Y \\ \Delta z_Y \end{bmatrix}, \quad P_{\Delta Z} = \begin{bmatrix} \Delta x_Z \\ \Delta y_Z \\ \Delta z_Z \end{bmatrix} \quad (6.1)$$

Similarly the sensor position offsets $P_{\Delta x}$, $P_{\Delta y}$, $P_{\Delta z}$ defined in equation 6.2 represent the position offsets of the frame of the x, y, and z sensor coils from the centre of the ideal sensor

position in the frame of the sensor.

$$P_{\Delta x} = \begin{bmatrix} \Delta x_x \\ \Delta y_x \\ \Delta z_x \end{bmatrix}, \quad P_{\Delta y} = \begin{bmatrix} \Delta x_y \\ \Delta y_y \\ \Delta z_y \end{bmatrix}, \quad P_{\Delta z} = \begin{bmatrix} \Delta x_z \\ \Delta y_z \\ \Delta z_z \end{bmatrix} \quad (6.2)$$

An illustration of the source and sensor offsets may be seen in Figure 6.2, however it should be noted that in this diagram the sensor frame orientation is the same as that of the source. This is a special case as the sensor offsets are defined with respect to the sensor coordinate system and must be converted into the source co-ordinate frame for processing.

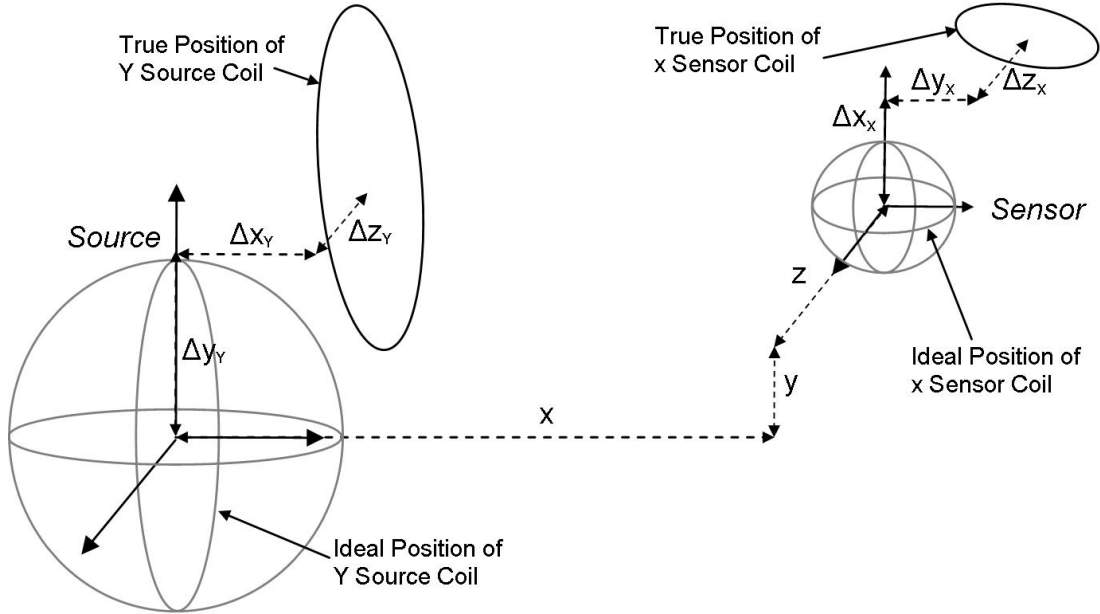


Figure 6.2: Sensor and source coil position offsets.

6.1.2 Coil Orientation Offsets

The frame of each source or sensor coil may be rotated with respect to the ideal source or sensor frame to describe the orientation of that coil. The orientation of each sensor coil must be known precisely as the size of the current induced within each coil depends on the alignment of the magnetic field and the plane of the coil. Three sensor orientation offset matrices R_x, R_y, R_z may be used to adjust the orientation frame of the x, y and z sensor coils

6. CALIBRATION

with respect to the sensor frame as defined in equations 6.3.

$$R_x = R(\Delta\alpha_x, \Delta\beta_x, \Delta\gamma_x), \quad R_y = R(\Delta\alpha_y, \Delta\beta_y, \Delta\gamma_y), \quad R_z = R(\Delta\alpha_z, \Delta\beta_z, \Delta\gamma_z) \quad (6.3)$$

where the angles α, β and γ represent the Euler angles of rotation about the x, y, and z axes and the function $R(\alpha, \beta, \gamma)$ represents the matrix of 6.4.

$$\begin{bmatrix} \cos(\gamma) \cos(\beta) & \sin(\gamma) \cos(\alpha) + \cos(\gamma) \sin(\beta) \sin(\alpha) & \sin(\gamma) \sin(\alpha) - \cos(\gamma) \sin(\beta) \cos(\alpha) \\ -\sin(\gamma) \cos(\beta) & \cos(\gamma) \cos(\alpha) - \sin(\gamma) \sin(\beta) \sin(\alpha) & \cos(\gamma) \sin(\alpha) + \sin(\gamma) \sin(\beta) \cos(\alpha) \\ \sin(\beta) & -\sin(\alpha) \cos(\beta) & \cos(\alpha) \cos(\beta) \end{bmatrix} \quad (6.4)$$

The orientation of the X, Y and Z source coils may require adjustment to correct differences in orientation with respect to the frame of the source. Source orientation offset matrices R_X, R_Y, R_Z defined in equation 6.5 may be used to transfer each source coil from the frame of the source into the frame of each source coil.

$$R_X = R(\Delta\alpha_X, \Delta\beta_X, \Delta\gamma_X), \quad R_Y = R(\Delta\alpha_Y, \Delta\beta_Y, \Delta\gamma_Y), \quad R_Z = R(\Delta\alpha_Z, \Delta\beta_Z, \Delta\gamma_Z) \quad (6.5)$$

Figure 6.3 illustrates the method by which the angles of rotation are used to rotate one frame into another. The order of euler rotations must follow a specific order α, β, γ and each transformation occurs with respect to the coordinate frame generated by the previous rotation.

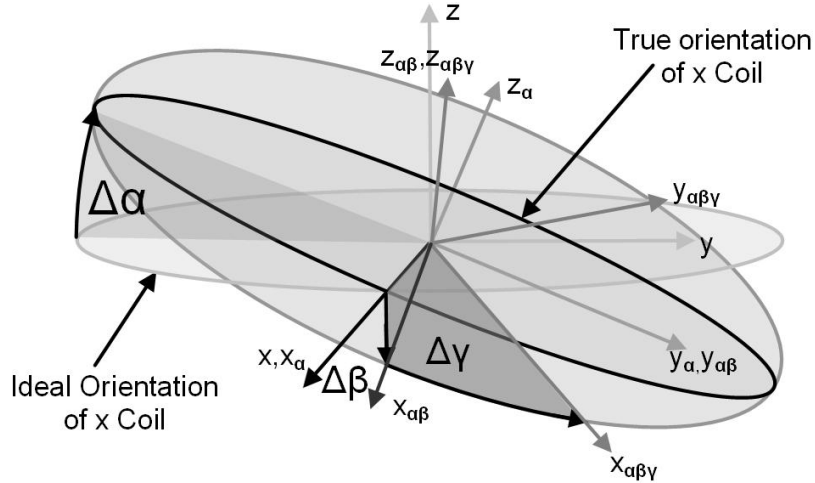


Figure 6.3: Coil transformations resulting from rotations $\Delta\alpha, \Delta\beta, \Delta\gamma$. Coordinates are transformed from $(x, y, z) \rightarrow (x_\alpha, y_\alpha, z_\alpha) \rightarrow (x_{\alpha\beta}, y_{\alpha\beta}, z_{\alpha\beta}) \rightarrow (x_{\alpha\beta\gamma}, y_{\alpha\beta\gamma}, z_{\alpha\beta\gamma})$ as the rotations are applied sequentially.

The source and sensing coils can be wound to a high level of precision and the orientation offsets may be used to represent only slight changes of the coil reference frame. As a result, it may be possible to express the orientation offset matrices more simply by using a two Euler angle rotation matrix $R(\alpha, \gamma)$. It should be noted that because all three coils lie along one of the axial planes, one euler rotation will always be in the plane of the coil.

6.1.3 Variations in Sensed and Detected Magnetic Fields

The physical variations in resistance, cross sectional area and number of turns within each coil can cause the the amount of magnetic field which is generated by a source coil or detected by a sensor coil to vary. The current within a coil may be related to the magnetic field by equation 6.6.

$$\mathbf{B}_X(r, \theta) = a^2 N \frac{V}{R} \left[\frac{\mu_0}{2} \left(\frac{\cos(\theta)}{r^3} \hat{\mathbf{i}}_r + \frac{\sin(\theta)}{2r^3} \hat{\mathbf{i}}_\theta \right) \right] \quad (6.6)$$

Here a is the radius of the coil, N is the number of coil turns, V is the voltage across the coil and R is the coil resistance. The magnetic field in equation 6.6 is therefore proportional to a^2 , N and R allowing the variations in these factors to be modeled with a single scaling factor.

If the theoretical magnetic fields for the source and sensor coils are denoted \mathbf{B} and the modified values denoted \mathbf{B}_M then equations 6.7 and 6.8 may be used to relate these quantities using scale factors ϵ_X, κ_Y and η_Z for the source and ϵ_x, κ_y and η_z for the sensor.

$$\mathbf{B}_{MX} = \epsilon_X \mathbf{B}_X, \quad \mathbf{B}_{MY} = \kappa_Y \mathbf{B}_Y \quad \mathbf{B}_{MZ} = \eta_Z \mathbf{B}_Z \quad (6.7)$$

$$\mathbf{B}_{Mx} = \epsilon_x \mathbf{B}_x, \quad \mathbf{B}_{My} = \kappa_y \mathbf{B}_y \quad \mathbf{B}_{Mz} = \eta_z \mathbf{B}_z \quad (6.8)$$

where uppercase subscripts X, Y and Z denote the magnetic fields generated by the x, y, and z source coils, and lowercase subscripts x, y and z denote the magnetic fields generated by the x, y, and z sensor coils.

6.1.4 Internal Inter-Coil Coupling Factors

The source and sensor within the tracking system implemented were each constructed from three orthogonal coils that were designed to be independent and without cross-coupling. In reality imperfections in the coil alignment and significant wiring connections caused voltages to be induced within ‘orthogonal’ coils. The inductance L of each coil can be used to relate

6. CALIBRATION

the voltage induced on a coil resulting from a change in the flow of current in another coil as shown in the equations in 6.9.

$$V_z = L_{zy} \frac{di_y}{dt}, \quad V_y = L_{yz} \frac{di_z}{dt}, \quad V_x = L_{xz} \frac{di_z}{dt}, \quad V_z = L_{zx} \frac{di_x}{dt}, \quad V_x = L_{xy} \frac{di_y}{dt}, \quad V_y = L_{yx} \frac{di_x}{dt} \quad (6.9)$$

where V_x , V_y and V_z are the open-loop voltages induced on the x, y and z sensor coils, i_x , i_y and i_z are the currents passing through the x, y and z sensor coils inducing those voltages, and L_{xy} , L_{xz} , L_{yz} , L_{yx} , L_{zx} , and L_{zy} are the mutual inductances between the x, y and z sensor coils. The mutual inductance between two coils of wire may related by *Nuemann's formula* which is expressed in equation 6.10 [Guru (1998)].

$$L_{xy} = \frac{\mu_y N_x N_y}{4\pi} \oint_{s_x} \oint_{s_y} \frac{\vec{dl}_x \cdot \vec{dl}_y}{r} \quad (6.10)$$

where N_x and N_y are the number of turns in the x and y coils, s_x and s_y are the contours of the x and y coils respectively, dl_x and dl_y are the infinitesimal elements of the x and y coils and r is the displacement between those elements. Ideally, the coils within the source and sensor would be orthogonal and $\oint_{s_x} \oint_{s_y} \vec{dl}_x \cdot \vec{dl}_y = 0$, however a position or orientation offset can change this as shown in figure 6.4.

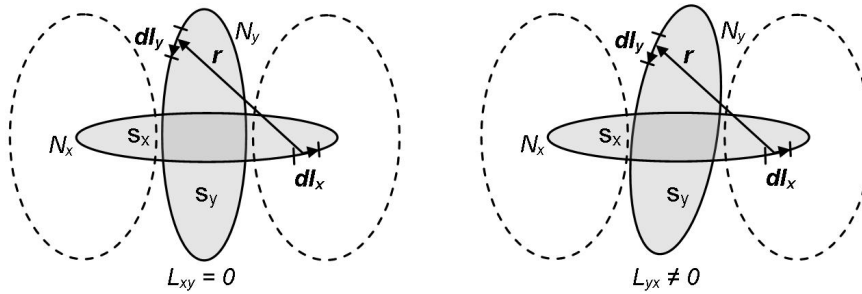


Figure 6.4: Orthogonal coils x and y located within the source or sensor.

The internal alignment of the source and sensor coils is fixed at the time of construction and therefore the mutual inductances between the coils (L_{xy} , L_{yx} , L_{xz} , L_{zx} , L_{yz} , L_{zy}) remain unchanged. The equations in 6.9 illustrate that the open-loop voltages induced by the change in current in another coil can be related by these mutual inductances. If proportionality constants are introduced to relate the voltage induced in a coil to the change in voltage in another coil a more accurate description of the system may be produced. Equation 6.11 relates the voltage induced in the y and z sensor coils resulting from a change in voltage in the x sensor coil, equation 6.12 relates the voltage induced on the x and z sensor coils to the

change in voltage on the y sensor coil and 6.13 relates the voltage induced on the x and y sensor coils to the change in voltage on the z sensor coil.

$$V_y = \tau_{yx} \frac{\partial V_x}{\partial t} \quad V_z = \tau_{zx} \frac{\partial V_x}{\partial t} \quad (6.11)$$

$$V_x = \tau_{xy} \frac{\partial V_y}{\partial t} \quad V_z = \tau_{zy} \frac{\partial V_y}{\partial t} \quad (6.12)$$

$$V_x = \tau_{xz} \frac{\partial V_z}{\partial t} \quad V_y = \tau_{yz} \frac{\partial V_z}{\partial t} \quad (6.13)$$

The six constants of proportionality for the sensor are defined to allow the open loop voltage in one sensor coil to be directly related to the change in open loop voltage in another as shown in equation 6.14.

$$\tau_{xy} = \frac{L_{xy}}{R_y}, \quad \tau_{yx} = \frac{L_{yx}}{R_x}, \quad \chi_{xz} = \frac{L_{xz}}{R_z}, \quad \chi_{zx} = \frac{L_{zx}}{R_x}, \quad \kappa_{yz} = \frac{L_{yz}}{R_z}, \quad \kappa_{zy} = \frac{L_{zy}}{R_y} \quad (6.14)$$

The circuitry within the sensor is not open loop, as shown in figure 6.1, however the adjustments required to model each coil as a closed loop are taken into account by the factors which describe the variations in sensed and detected magnetic fields. A set of proportionality constants may also be described for the source (τ_{XY} , τ_{YX} , χ_{XZ} , χ_{ZX} , κ_{YZ} , κ_{ZY}), however these cannot be defined in the same manner as the signal generation circuitry uses active circuitry to drive the voltage across the source coils to zero whenever the coils are not excited as shown in Figure 2.2. Equations 6.15, 6.16 and 6.13 may be used to relate the voltage induced on a source coil to the change in voltage in the x, y and z source coils respectively.

$$V_Y = \tau_{YX} \frac{\partial V_X}{\partial t} \quad V_Z = \tau_{ZX} \frac{\partial V_X}{\partial t} \quad (6.15)$$

$$V_X = \tau_{XY} \frac{\partial V_Y}{\partial t} \quad V_Z = \tau_{ZY} \frac{\partial V_Y}{\partial t} \quad (6.16)$$

$$V_X = \tau_{XZ} \frac{\partial V_Z}{\partial t} \quad V_Y = \tau_{YZ} \frac{\partial V_Z}{\partial t} \quad (6.17)$$

Here V_X , V_Y and V_Z are the voltages on the x, y and z source coils. The scaling factors may be defined as being proportional to the mutual inductances between the source coils as shown in equations 6.18. The scaling factors are difficult to define more accurately without a detailed analysis of the circuitry used to eliminate induced voltages.

$$\tau_{XY} \propto \frac{L_{XY}}{R_Y} \quad \tau_{YX} \propto \frac{L_{YX}}{R_X} \quad \chi_{XZ} \propto \frac{L_{XZ}}{R_Z} \quad \chi_{ZX} \propto \frac{L_{ZX}}{R_X}, \quad \kappa_{YZ} \propto \frac{L_{YZ}}{R_Z} \quad \kappa_{ZY} \propto \frac{L_{ZY}}{R_Y} \quad (6.18)$$

where L_{XY} represents the mutual inductance which relates the voltage on the x source coil to the change in voltage on the y source coil and R_X , R_Y and R_Z are the resistances of the source coils when those coils are not in use.

6.1.5 Hardware Circuitry

Tolerance variations in the analogue generation and detection circuitry can cause differences in the magnetic fields generated and detected by the source and sensor. The analogue hardware associated with the system must be either directly calibrated or sampled through a feedback loop in order to account for such variations. Variations in the signal generation circuitry can alter the gain, frequency and phase of the generated signal. Similarly, variations between the gain of the instrumentation amplifiers can scale the voltages detected by the ADC's. Previously developed systems measure and calibrate such variations in real-time allowing measurements to be made of the assembled hardware configuration used for tracking. By using these techniques, adjustments to the calibration factors which represent the generated and detected magnetic fields may be made and included in the algorithm to account for changes in the performance of the analogue circuitry. A gain adjustment for source (G_X, G_Y, G_Z) and sensor (G_x, G_y, G_z) amplification circuitry may be defined which accounts for variations from the theoretical value. Similarly phase offset for each of the source ($\Delta_X, \Delta_Y, \Delta_Z$) and sensor circuits ($\Delta_x, \Delta_y, \Delta_z$) as shown in equations 6.19 and 6.20.

$$V_{Mx} = G_x V_x(t + \Delta_x) \quad V_{My} = G_y V_y(t + \Delta_y) \quad V_{Mz} = G_z V_z(t + \Delta_z) \quad (6.19)$$

where V_{Mx} , V_{My} and V_{Mz} are the adjusted values of the detected voltages.

$$V_{MX} = G_X V_X(t + \Delta_X) \quad V_{MY} = G_Y V_Y(t + \Delta_Y) \quad V_{MZ} = G_Z V_Z(t + \Delta_Z) \quad (6.20)$$

6.1.6 Aperture Correction

The magnetic field generated by a loop of wire may be accurately approximated as a point source when the radius of the coil is much smaller than the separation distance between the source and sensor. This approximation is inappropriate for use outside of these limitations however and correction is required in order to take into account the finite radius, height, and width of the coil. One approach to resolve this inaccuracy is to represent the magnetic fields generated by the current loop dipole using Legendre polynomials and an infinite series of terms [Arfken (1968)]. This series, when correctly truncated, allows accurate calculation of the magnetic field vectors when the radius of the source coil is comparable to the separation

between the sensor and source.

6.1.7 Environmental Effects

The effects of localized metallic and ferromagnetic objects have a significant effect on the magnetic fields and can cause the resolved position and orientation measurements to be heavily distorted. Such effects are extremely difficult to calibrate, and require a precise knowledge of the tracking environment. The implementation of such a distortion correction system is far from practical for anything other than a fixed purpose tracking system (such as a pilot's helmet or surgeon's knife), although the development of a system which uses multiple fixed-alignment sensors and an *a posteriori* data set to construct a distortion map of the magnetic fields is an active area of research.

6.1.8 Complicated Coil Distortion Effects

The source and sensor coils within the current implementation both rely on the use of three mutually orthogonal coils wound about an air core with a high degree of precision. In spite of the time and effort spent on the precision winding of the coils, other practical effects within the system will also distort the magnetic field generated, many of which are too complex to correct. If the wires wound in the form of three mutually perpendicular solenoids do not act as perfect loops with a fixed offset position and orientation, the magnetic fields will be distorted significantly and the resulting magnetic field will likely be too complex to describe with a simple mathematical model. Other imperfections such as the connection of the wire to the sensor or source and the winding of the coils (three perpendicular coils wound directly over one another will cause at least one of those coils to contain a disproportionate breadth and width) which can distort the magnetic field generated or detected as shown in Figure 6.5.

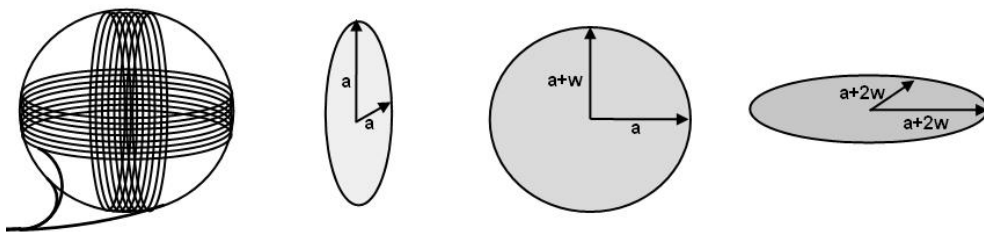


Figure 6.5: Distortion of coil widths due to sequential coil windings given a coil radius of a and a coil width of w .

6.2 Measurement of Distortion Parameters

The parameter adjustments of Section 6.1 provide descriptions of how many of the physical imperfections of each component may be modeled by introducing correction factors. If the correction factors are known and can be used to accurately predict the magnetic fields detected by a sensor then the models for calibrating the system components may be verified. Equations 5.31, 5.32 and 5.33 may be used to predict the magnetic fields at a point in space and by modifying these equations to include correction factors, a set of calibrated predicted signals may be calculated and compared to the detected signals. The mathematics required to calculate and verify the distortion parameters will not be covered as the hardware to allow verification of these models with sufficient accuracy was not constructed, however a brief outline of methods which could be used for measuring the distortion within the system components is given in the following.

6.2.1 Source Coil Position and Orientation Offsets

The offset in the position and orientation of each source coil may be measured by aligning each source coil with a stationary set of detecting coils. If the source is rotated so that the coils are aligned along both sides of the coil axes, the offset in the coil position may be calculated by determining the difference in the detected magnetic fields as shown in figure 6.6. The separation distance between the source and sensor must be sufficiently large so as to avoid aperture distortion in the magnetic fields generated by the source and the detection coils must be exactly aligned with the axis of source rotation.

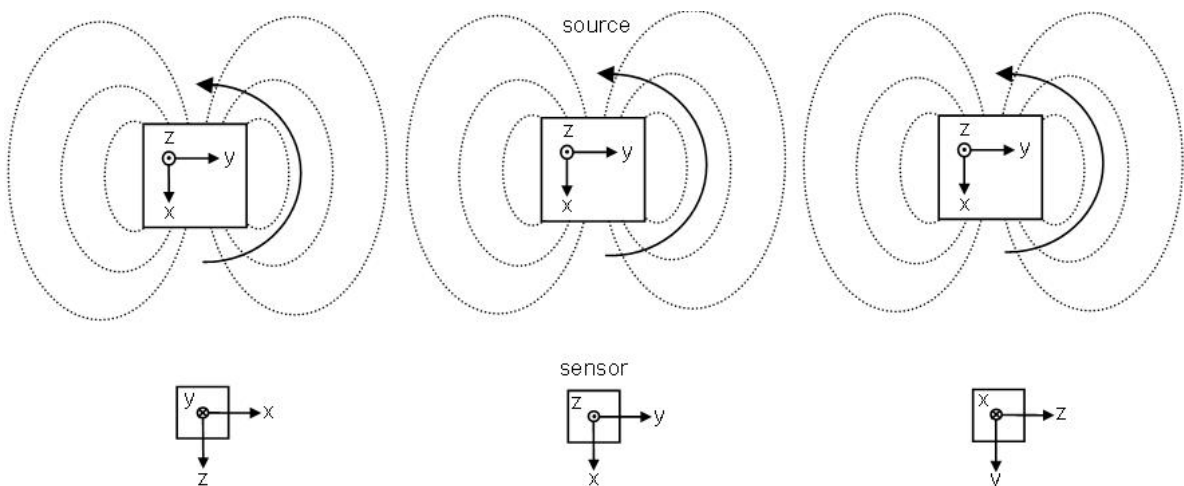


Figure 6.6: Proposed method of sensor coil calibration.

6.2.2 Internal Source Coil Coupling and Gain Variations

A small amount of mutual inductance between source coils can cause the generation of significant current in the orthogonal coils. In order to eliminate the generation of magnetic fields, orthogonal coils are driven to zero when not driving a source coil. Thus mutual inductance between the source coils will not change, however the effects of mutual inductance is minimized by the use of active circuitry. The current passing through each coil may be measured in real-time in order to determine the size of the current passing through the coil being excited and the orthogonal coils. This allows a measure to be made of the magnetic fields being generated by each coil so that the algorithm may be adjusted accordingly. The source must be calibrated in real-time as a number of different components are combined to construct the excitation circuitry including the resonant capacitors, source coils and signal generation circuitry. The most accurate measure of the system is obtained by real-time measurement of the current. The internal coil coupling within the source is a significant source of error which the Fastrak has been designed to counteract, and while measures have also been implemented to produce an identical current magnitude within all the source coils, differences of the order of 25% remain within the detected signals.

6.2.3 Sensor Coil Position and Orientation Offsets

In order to determine the sensor coil position and orientation offsets each sensor coil may be accurately aligned with a calibrated source coil at a number of positions and orientations. This method is difficult to implement as the properties of the both the source coil and the test jig must be known very accurately to prevent the sensor coil offsets from being incorrectly determined. It may be easier to use a single independent coil thereby eliminating all possibility of internal source coil coupling of orthogonal coils during the source coil excitation. The resulting affects appear to provide a small (1%) but significant contribution to the resulting imperfections in detected magnetic fields.

6.2.4 Internal Sensor Coil Coupling and Gain Variations

The internal sensor coil coupling may be measured by passing a current through each coil at the excitation frequency and measuring the induced voltage signals on all three sensing coils as shown in Figure 6.7. Each sensor coil is connected to an instrumentation amplifier and the voltages measured across each amplifier will represent the magnetic fields induced through variations in resistance, self inductance and mutual inductance between the coils. This method of calibration does however rely on the signal gain and conversion detected

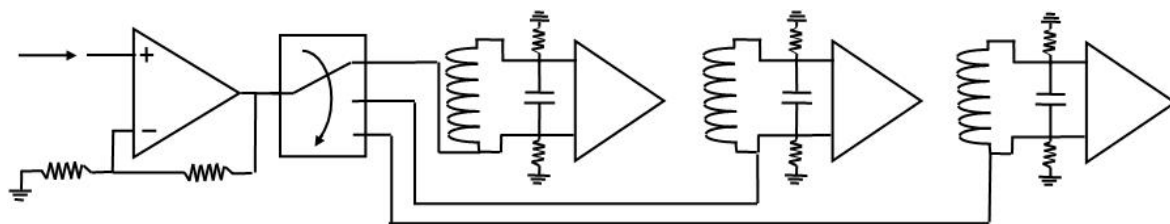


Figure 6.7: Proposed internal sensor coil coupling test jig.

signal be known. This may be measured by generating three identical voltages across the inputs of each instrumentation amplifier so that the characteristics of the signal detection circuitry are known. Thus the gain of each sensor coil and the coupling factors resolved by the test jig provide a direct measurement of the distortion within the sensing coils. The use of precisely wound sensor coils allows the mutual and self inductance of the distortion in the sensor coils to be limited to approximately 5% of the detected signals.

6.2.5 Verifying the Calibration Model

The calibration data obtained from the test jigs for the source and sensor allow a model to be used to predict the magnetic fields detected by the sensor at any given position in space. In order to verify this model the source and sensor must be accurately aligned at a number of positions and orientations in order to ensure that the distortions have been correctly measured and applied in a valid manner. A final test jig may be used to perform these measurements at a number of different sensor positions and orientations over the tracking range as shown in Figure 6.8.

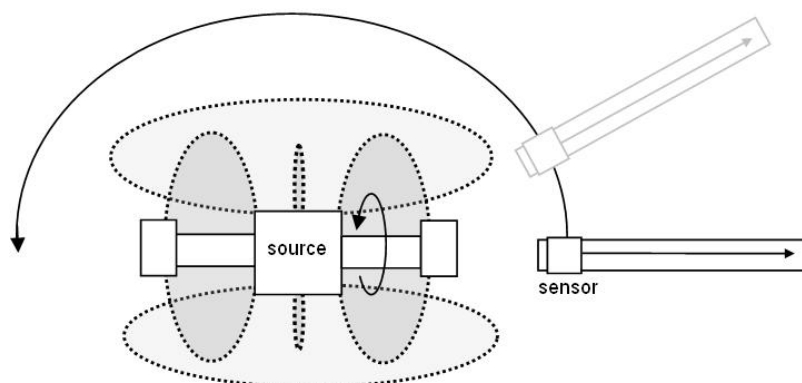


Figure 6.8: Proposed test jig used to verify measurement model.

If the source is rotated about the y axis and the sensor is moved on an arm radially about the source in the xy plane, the source and sensor coils will align in a number of different combinations which allow any inaccuracies in the model describing the magnetic fields to be observed. Once the model has been verified, methods of correction may be applied to the detected signals and to the algorithms used to resolve the position and orientation calculation algorithms thereby implementing a calibration system.

6. CALIBRATION

Chapter 7

Results

7.1 Test Jig Construction

The verification of the algorithms described in Chapter 5 was conducted by using two test jigs for analysis. The first allowed variation of the source orientation (about the z axis) and the sensor separation distance and was called the *source rotation test jig*. The second allowed variation of the the sensor orientation (about the z axis) and the source separation distance and was called the *sensor rotation test jig*. The separation distances were measured at intervals of 15 mm ($\pm 1\text{mm}$), while the source and sensor rotations were measured at 10° ($\pm 1^\circ$) intervals.

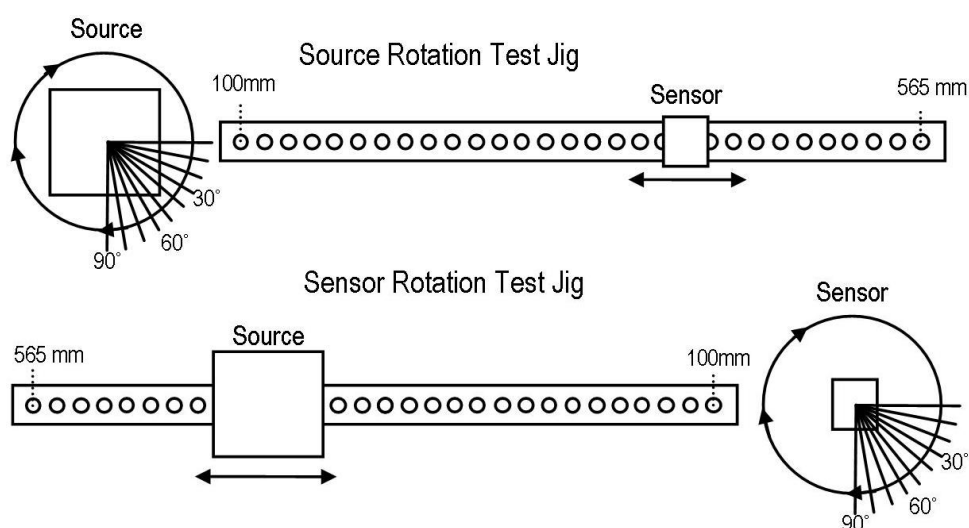


Figure 7.1: Initial test jigs used for the verification of theory and testing of simplified calibration models.

The test jig apparatus was constructed from wood with minimal metallic components and raised from the floor to avoid interference from metal within the building structure. Angular measurements were made with the aid of a 360° plastic compass fixed to each jig and the separation distances were varied by using a hole-peg arrangement.

7.2 Theoretical Models and Practical Data

Equations 5.31, 5.32 and 5.33 which were developed in Section 5.2 allow the prediction of magnetic fields that will be detected at a given sensor position and orientation, and can be compared against those detected using either of the test jigs. The detected magnetic fields varied with respect to the frame of the source and thus rotating the source had an identical effect to rotating the sensor along a circular arc about the source position. The source and sensor were rotated clockwise in their respective test jigs which caused an effective anticlockwise rotation of the sensor in the ‘source rotation test jig’ as shown in Figure 7.2.

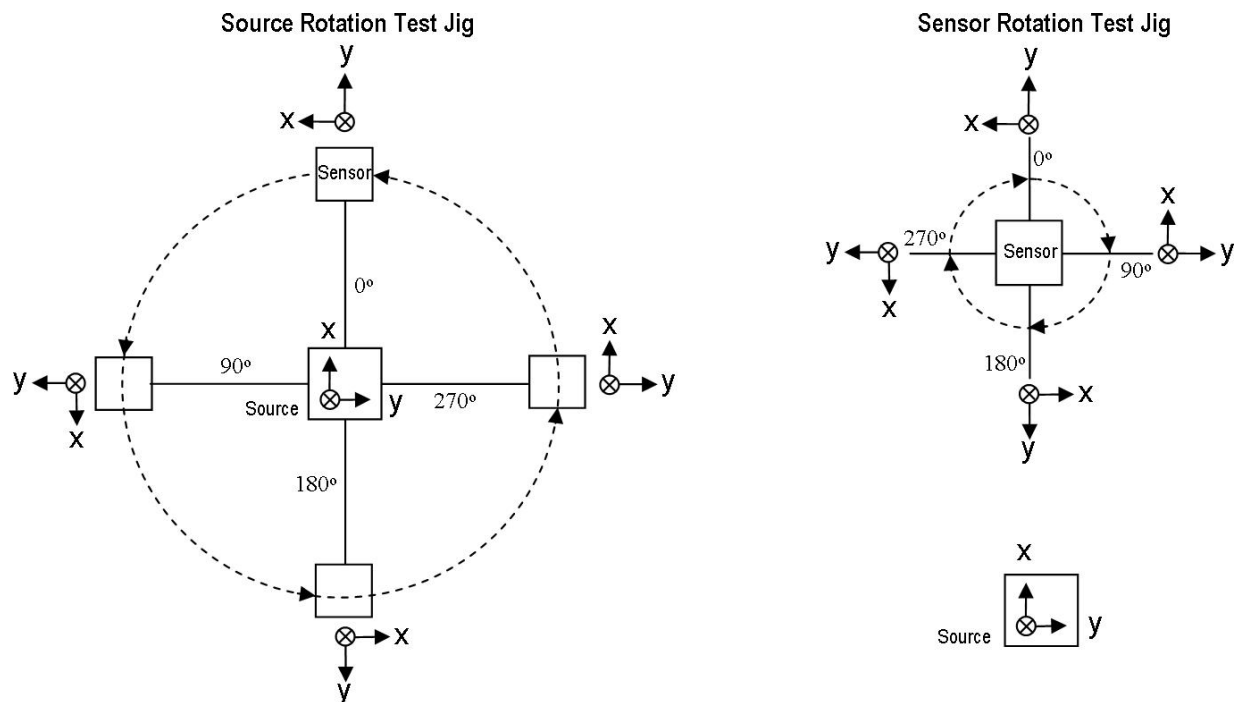


Figure 7.2: Sensor position and orientation with respect to the frame of the source in the source and sensor rotation test jigs.

7.2.1 Source Rotation Test Jig Data

The relative amplitude of the signals detected by the sensor in the source rotation test jig shown in Figures 7.3 and 7.5 are colour and marker coded according to the source and sensor coils involved in the generation and detection of the magnetic fields. The magnetic fields detected during the excitation of each source coil are coloured green (x source coil), red (y source coil), and blue (z source coil). The data sets detected by the sensor coils are denoted with three data markers ‘o’ (x sensor coil), ‘.’ (y sensor coil), and ‘∇’ (z sensor coil). The magnetic field measurements predicted by equations 5.31, 5.32 and 5.33 are dashed, while the detected measurements obtained from the test jigs are solid.

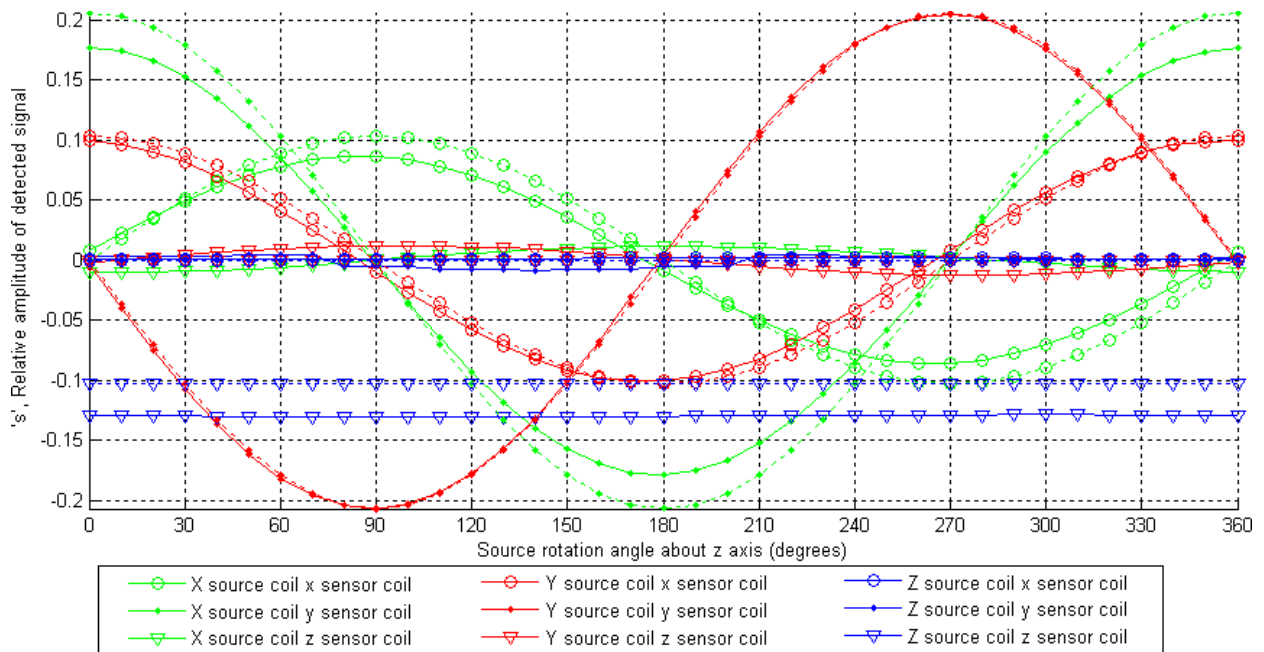


Figure 7.3: Comparison of the predicted and detected signals for the source rotation test jig.

Consider the case at 0° . If the x source coil (green) is excited, the y sensor coil (‘.’) will be co-axially aligned and the coupling will be at a relative maximum. The x (‘o’) and z (‘∇’) sensor coils will both be orthogonal to the direction of the magnetic field and will have a coupling that is ideally zero. If the y source coil (red) is excited at 0° the x sensor coil (‘o’) will have a coplanar coupling, which will be half that of two co-axially aligned coils. The y (‘.’) and z (‘∇’) sensor coils will both be orthogonal to the direction of the magnetic field and should not detect any magnetic fields. If the z source coil (blue) is excited, the z sensor coil (‘∇’) will share a coplanar alignment while the x (‘o’) and y (‘.’) sensor coils will be orthogonal to the magnetic field which will not change as the source rotates about the z axis. A positive

signal polarity indicates that the voltage induced across a sensor coil has the same polarity as the current which induced it. Therefore, a positive coaxial coupling indicates that the source and sensor coils face the same direction, while a positive coplanar coupling indicates that the coils face opposing directions as shown in Figure 7.4.

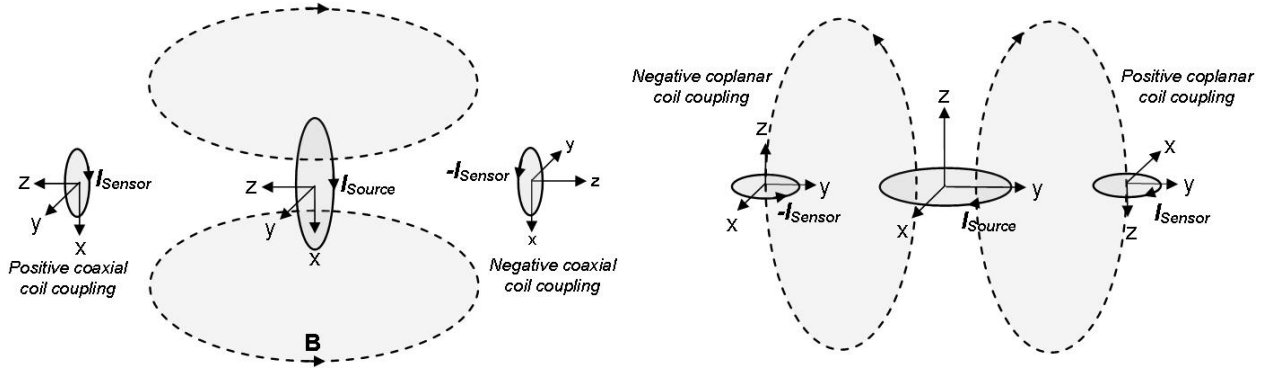


Figure 7.4: Coil alignment and current direction associated with coaxial and coplanar coupling.

As the source rotates to 90° , the y source coil (red) will become negatively coaxially aligned with the y sensor coil (\cdot), and the x source coil (green) will share a positive coplanar alignment with the x sensor coil (\circ) causing a positive signal to be detected. These descriptions of source and sensor coil couplings may be used to explain the coil couplings at the remaining angles of source rotation.

7.2.2 Sensor Rotation Test Jig Data

The sensor did not change position in the sensor rotation test jig and thus only the x source coil (green) could be coaxially aligned with the sensor coils.

The alignment of the sensor along the x axis of the source frame caused the x (\circ) and y (\cdot) sensor coils to alternate in and out of coaxial alignment with the x source coil (green), and in and out of coplanar alignment with the y source coil (red) as shown in Figure 7.5. The sensor was rotated clockwise about the z axis and as a result there is no coupling variation in the z sensor coil (∇) which remained in coplanar alignment with the z source coil. Similarly, the x (\circ) and y (\cdot) sensor coils remained orthogonal to the z source coil and correspondingly detected almost no current.

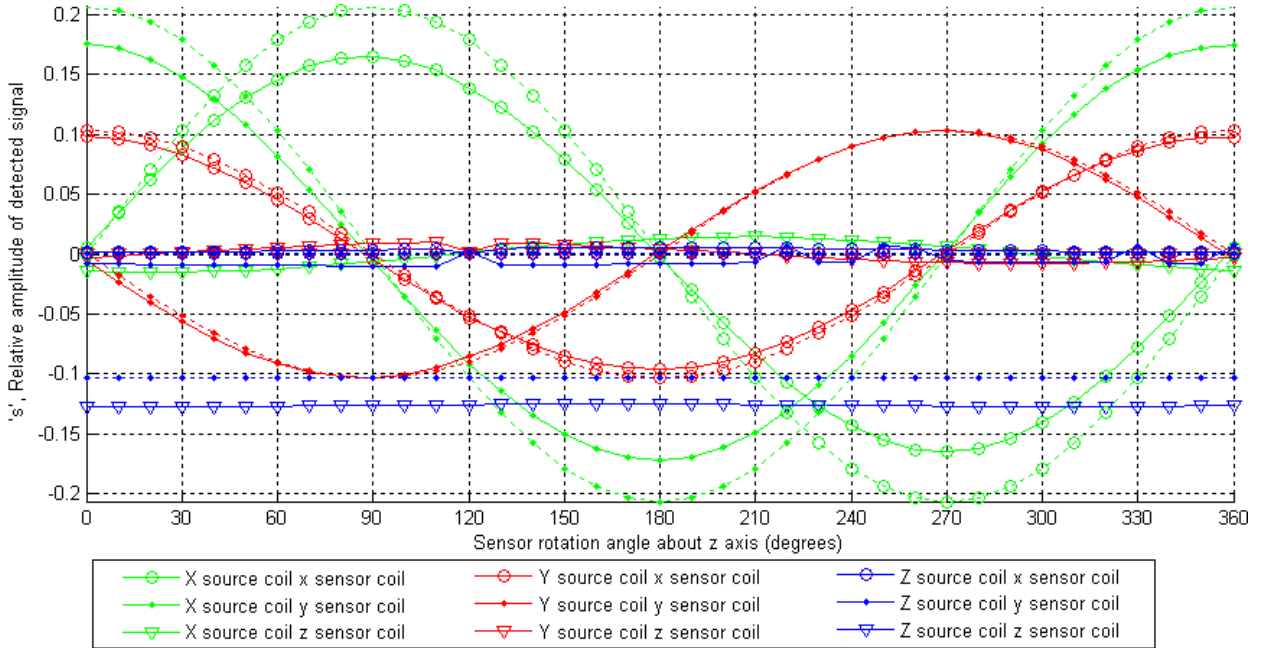


Figure 7.5: Comparison of the predicted and detected signals for the sensor rotation test jig.

7.2.3 Test Jig Alignment

The source and sensor in each test jig were located in the same position and orientation at 0° (as shown in Figure 7.2) and thus an identical set of magnetic fields were detected at this angle in both test jigs. As the sensor was rotated (in the sensor rotation test jig) to 180° , the magnetic fields matched those detected by the sensor at a source rotation angle of 180° (in the source rotation test jig) *even though the sensor was in a position on the opposite side of the yz plane in the source frame*. This result demonstrates the hemispheric ambiguity that prevents the polarity of the x co-ordinate from being determined due to identical magnetic fields being detected at positions of $(+x, |y|, \pm z)$ and $(-x, |y|, \mp z)$ as discussed in Section 5.2.4. (The source and sensor were rotated in the xy plane for which $z = 0$.)

7.3 Theoretical Model Calibration

Figures 7.3 and 7.5 demonstrate that the magnetic fields may be modeled by equations 5.31, 5.32 and 5.33, but also illustrate the differences between the predicted and detected magnetic fields in each of the test jigs due to the physical imperfections described in Section 6.1. Precision calibration test jigs were not constructed due to the extensive accuracy and expense requirements, however it was possible to demonstrate the effectiveness of the calibration tech-

niques by a trial and error estimate of some of the distortion parameters.

The distortion effects most prominent within the measured data were the variations in the self inductance of the source and sensor coils and the presence of mutual inductance between the sensor coils. Several simple correction models were developed to describe such imperfections and help demonstrate the increase in accuracy that can be achieved when the imperfections of the system components are taken into account.

7.3.1 Development of A Simple Calibration Model

A simple method of modeling the system distortion was to adjust the calibration model to distort the predicted signals in the same manner as the detected signals. Once ‘correctly distorted’ the reverse process could be applied to the detected signals so that the distortion was removed and the detected signals matched the original (distortionless) predicted signals. The process could be verified by using two test jigs. If the calibration model was incorrectly applied to provide a good match between the predicted and detected signals for one test jig, it would be unlikely that the calibration model would also provide a match for a completely different motion in another test jig.

The calibration model was based on the application of two correction methods to the predicted signal matrix S_P to adjust it to match the detected signal matrix S_D . The predicted signal matrix S_P shown in equation 7.1 was composed of elements calculated from the equations 5.31, 5.32 and 5.33, while the detected signal matrix was composed of signals sampled from the test jigs.

$$S_P = \begin{bmatrix} s_{XxP} & s_{XyP} & s_{XzP} \\ s_{YxP} & s_{YyP} & s_{YzP} \\ s_{ZxP} & s_{ZyP} & s_{ZzP} \end{bmatrix} = \Lambda R \begin{bmatrix} B_{XxP} & B_{XyP} & B_{XzP} \\ B_{YxP} & B_{YyP} & B_{YzP} \\ B_{ZxP} & B_{ZyP} & B_{ZzP} \end{bmatrix} \quad (7.1)$$

$$S_D = \begin{bmatrix} s_{XxD} & s_{XyD} & s_{XzD} \\ s_{YxD} & s_{YyD} & s_{YzD} \\ s_{ZxD} & s_{ZyD} & s_{ZzD} \end{bmatrix} \quad (7.2)$$

where the columns of S_P and S_D correspond to the signals detected from the x, y and z sensor coils, and the rows correspond to signals detected during x, y and z source coil excitations. The scalar constant Λ represents the change in magnitude resulting from the ideal conversion of a magnetic field passing through a sensor coil into a dimensionless amplitude estimate s

using the estimation techniques described in Chapter 4. The rotation matrix R represents the sensor orientation with respect to the frame of the source as defined in equation 5.36.

The first method of correction was to take into account the imperfections in the sensing coils. By treating each coil as ideal, the coupling of each sensor coil could be accounted for by the mutual inductance between the coils. This adjustment could be applied to the predicted signal matrix S_P by applying a sensor coupling distortion matrix D_{SNSRC} as shown in equation 7.3.

$$D_{SNSRC} = \begin{bmatrix} 1 & d_{xy} & d_{xz} \\ d_{yx} & 1 & d_{yz} \\ d_{zx} & d_{zy} & 1 \end{bmatrix} \quad (7.3)$$

Here $d_{xy} \propto L_{xy}$ and relates the signal induced on the x sensor coil to the signal detected on the y sensor coil. This approach relies on the signal s_x resolved from the signal on the x sensor coil increasing in a directly proportional manner to the signal s_y resolved from the signal on the y sensor coil. Such a premise is valid even though the voltage induced on the x sensor coil is proportional to the *change* in current on the y sensor coil because s is estimated using a phase independent technique (equation 4.10) from a sample set which includes the entire pulse interval. The sample set from the x sensor coil will therefore contain a sinusoidal signal that is directly proportional in size to the sinusoidal signal on the y sensor coil.

The second method of correction was to adjust the self inductance of each sensing coil. If distortion factors proportional to the self inductance of each sensor coil are defined for the x, y and z sensing coils as d_{xx} , d_{yy} and d_{zz} , then each of these factors can be used to scale the signals detected by the x, y and z sensor coils. This may be achieved by inserting these values into the diagonal of D_{SNSRC} to create a new matrix describing all of the sensor distortion D_{SNSR} as shown in equation 7.4.

$$D_{SNSR} = \begin{bmatrix} d_{xx} & d_{xy} & d_{xz} \\ d_{yx} & d_{yy} & d_{yz} \\ d_{zx} & d_{zy} & d_{zz} \end{bmatrix} \quad (7.4)$$

Although the factors d_{xx} , d_{yy} and d_{zz} are proportional to the self inductance of each sensing coil, they may also take into account variations within the signal amplification and detection circuitry (such as gain). Thus, each value of s will be adjusted according to the sensing circuitry from which the corresponding signal was obtained.

7. RESULTS

The sensor distortion matrix D_{SNSR} can therefore be used to modify the predicted signal matrix S_P to include sensor distortion via matrix multiplication as shown in equation 7.5.

$$S_P D_{SNSR} = \begin{bmatrix} s_{XxP} & s_{XyP} & s_{XzP} \\ s_{YxP} & s_{YyP} & s_{YzP} \\ s_{ZxP} & s_{ZyP} & s_{ZzP} \end{bmatrix} \begin{bmatrix} d_{xx} & d_{xy} & d_{xz} \\ d_{yx} & d_{yy} & d_{yz} \\ d_{zx} & d_{zy} & d_{zz} \end{bmatrix} \quad (7.5)$$

The three columns of S_P (which represent the signals detected by the x, y and z sensor coils) will be scaled by d_{xx} , d_{yy} , and d_{zz} , and the elements in each row (which represent the signals detected during common source coil excitations) will be combined according to level of coupling between the sensor coils.

A similar approach may also be used to modify the predicted signal matrix S_P to account for distortions within the source coils. A source distortion matrix D_{SRC} may be developed as shown in equation 7.6.

$$D_{SRC} = \begin{bmatrix} d_{XX} & 0 & 0 \\ 0 & d_{YY} & 0 \\ 0 & 0 & d_{ZZ} \end{bmatrix} \quad (7.6)$$

The diagonal elements d_{XX} , d_{YY} and d_{ZZ} are proportional to the variations in self inductance in each of the source coils, and like the sensor may also account for gain adjustments in the hardware circuitry. The source distortion matrix D_{SRC} may be used to modify the predicted signal matrix S_P to account for the imperfections in the source by multiplication as shown in equation 7.7. Each row of S_P (corresponding to the signals detected during the x, y and z source excitations) will be scaled by the diagonal elements d_{XX} , d_{YY} and d_{ZZ} to account for variations in the self inductance of each source coil.

$$D_{SRC} S_P = \begin{bmatrix} d_{XX} & 0 & 0 \\ 0 & d_{YY} & 0 \\ 0 & 0 & d_{ZZ} \end{bmatrix} \begin{bmatrix} s_{XxP} & s_{XyP} & s_{XzP} \\ s_{YxP} & s_{YyP} & s_{YzP} \\ s_{ZxP} & s_{ZyP} & s_{ZzP} \end{bmatrix} \quad (7.7)$$

A new calibrated predicted signal matrix S_{PC} may be constructed which can be used to include these imperfections within the system components. The calibrated predicted signal matrix may be calculated by using both the source and sensor distortion matrices D_{SRC} and

D_{SNSR} as shown in equation 7.8.

$$\begin{aligned}
 S_{PC} &= D_{SRC} S_P D_{SNSR} \\
 &= \begin{bmatrix} d_{XX} & 0 & 0 \\ 0 & d_{YY} & 0 \\ 0 & 0 & d_{ZZ} \end{bmatrix} \begin{bmatrix} s_{XxP} & s_{XyP} & s_{XzP} \\ s_{YxP} & s_{YyP} & s_{YzP} \\ s_{ZxP} & s_{ZyP} & s_{ZzP} \end{bmatrix} \begin{bmatrix} d_{xx} & d_{xy} & d_{xz} \\ d_{yx} & d_{yy} & d_{yz} \\ d_{zx} & d_{zy} & d_{zz} \end{bmatrix} \quad (7.8)
 \end{aligned}$$

The calibrated predicted signal matrix S_{PC} does not account for a number of other imperfections within the system including position and orientation offsets and mutual inductance within the source. Such adjustments cannot be made without an analysis as to how these imperfections affect the generation of the magnetic fields - the effect of which will differ according to the sensor position and orientation. Similarly, the sensor position and orientation offsets cannot be corrected using such a simple model as knowledge of the sensor position and orientation are required in order to resolve the exact magnetic field passing through each coil.

7.3.2 Implementation of the Simple Calibration Model

The distortion parameters within the source and sensor distortion matrices D_{SRC} and D_{SNSR} were estimated by examining the differences between S_P and S_D using Figures 7.3 and 7.5. Each form of distortion exhibited a different characteristic within the measured data. Variations in the self inductance of each source coil caused those signals which share a common colour in the figures to differ in magnitude by a scale factor (d_{XX} , d_{YY} , or d_{ZZ}). Variations in the self-inductance of each sensor coil caused those signals which share a common symbol in the figures to differ in magnitude by a scale factor (d_{xx} , d_{yy} and d_{zz}).

Mutual inductance between the sensor coils caused an offset in the signal detected on each coil which was proportional to the signals detected on the orthogonal coils during the same source coil excitation. These effects are clearest at angles of 0° , 90° , 180° , and 270° , where certain sensor coils detected a signal in spite of being orthogonally aligned with the magnetic field at the sensor position. The effects of source position and orientation offsets were also observable within the measured data, made apparent by the difference in the magnitude of the magnetic fields detected when a coil was aligned at opposite sides of a source coil at different points of the source rotation.

The diagonal elements of D_{SRC} and D_{SNSR} were estimated by adjusting the scaling factors of the source and sensor coils at sensor positions axially aligned with the x and y source coils so

that S_{XxP} , S_{XyP} , S_{YxP} and S_{YyP} matched S_{XxD} , S_{XyD} , S_{YxD} and S_{YyD} . At such positions the magnetic field detected by a sensor coil was ideally at a maximum and directly proportional to the scalar factors (e.g. $s_{XyD} \propto d_{XX}d_{yy}$ at 0°). The signals detected by the z sensor coil during the z source excitation were invariant of the angle or rotation and thus d_{ZZ} and d_{zz} were assigned scale factors based on this limited data. The off-diagonal elements of D_{SNSR} were estimated at sensor positions for which the sensor was orthogonal to the source coils for which a sensor coil did not ideally detect a signal. Hence by correlating the signal detected on an orthogonal sensor coil at a point for which another sensor coil detected a maximum magnetic field, the coupling between the sensor coils could be estimated. The values determined using these techniques are shown in equations 7.9.

$$D_{SRC} = \begin{bmatrix} 0.84 & 0 & 0 \\ 0 & 0.98 & 0 \\ 0 & 0 & 1.25 \end{bmatrix}, \quad D_{SNSR} = \begin{bmatrix} 0.96 & -0.034 & -0.01 \\ 0.034 & 1.00 & -0.06 \\ 0.01 & 0.06 & 1.00 \end{bmatrix} \quad (7.9)$$

Although the calibration estimates shown above were obtained using an ‘ad hoc’ method, iterative techniques may be implemented as an automated process to minimize the mean square error (MSE) between S_{PC} and S_D using more accurate test jigs. Although this may allow some increase in the accuracy of the resolved parameters, the effects of the parameters not accounted for would still distort the signal significantly.

7.3.3 Source Rotation Test Jig Calibration

The application of the distortion models reduced the error between the calibrated predicted signal matrix S_{PC} and the detected signal matrix S_D by an order of magnitude. Figure 7.6 illustrates the difference between S_{PC} and S_D both before calibration (*in red*) and after calibration (*in black*). Several outliers appear in Figure 7.6 due to noise affecting the polarity estimation method as outlined in Section 4.3.3. The application of the distortion correction matrices D_{SRC} and D_{SNSR} reduced the MSE from 6.2×10^{-3} to 4.7×10^{-4} .

The effects of the source distortion parameters not accounted for (mutual inductance between the source coils, coil position and orientation offsets) must be compensated for in order to reduce the error further. This is supported by Figure 7.6, where the remaining errors do not appear to be random but to have systematic dependence on the angle of source rotation, indicative of the presence of uncalibrated parameters within the models.

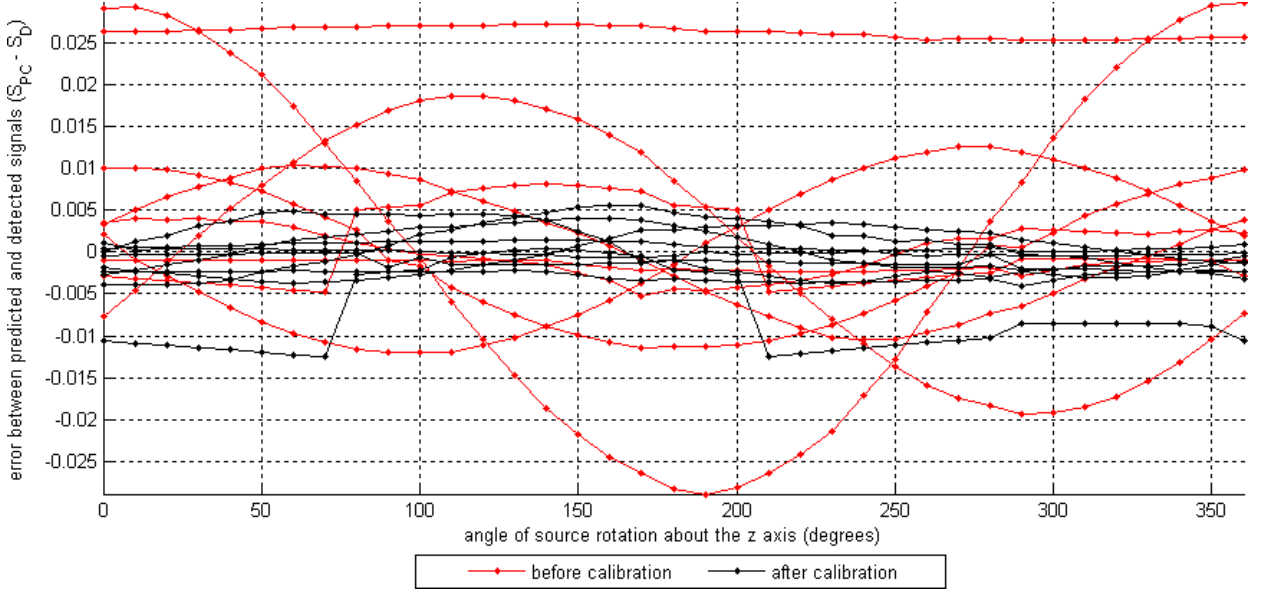


Figure 7.6: Difference between the calibrated and detected magnetic fields in the source rotation test jig.

7.3.4 Sensor Rotation Test Jig Calibration

The use of a second test jig constructed from an identical source and sensor but moved through a different motion allowed the estimated calibration parameters to be verified by using different combinations of source and sensor coil coupling. The same calibration parameters reduced the systematic errors between S_{PC} and S_D from an MSE of 9.1×10^{-3} before calibration (*in red*) to 3.8×10^{-4} after calibration (*in black*).

The sensor rotation test jig exhibited a slightly lower degree of MSE than the source rotation test jig which may be attributed to the large offsets caused by polarity errors in the detected measurements of the source rotation test jig (shown in Figure 7.6). It is also possible that because the calibration model takes into account the mutual and self inductance of the sensor coils, but only takes into account the self inductance of the source coils, greater differences occur when the sensor coils become coupled with different source coils.

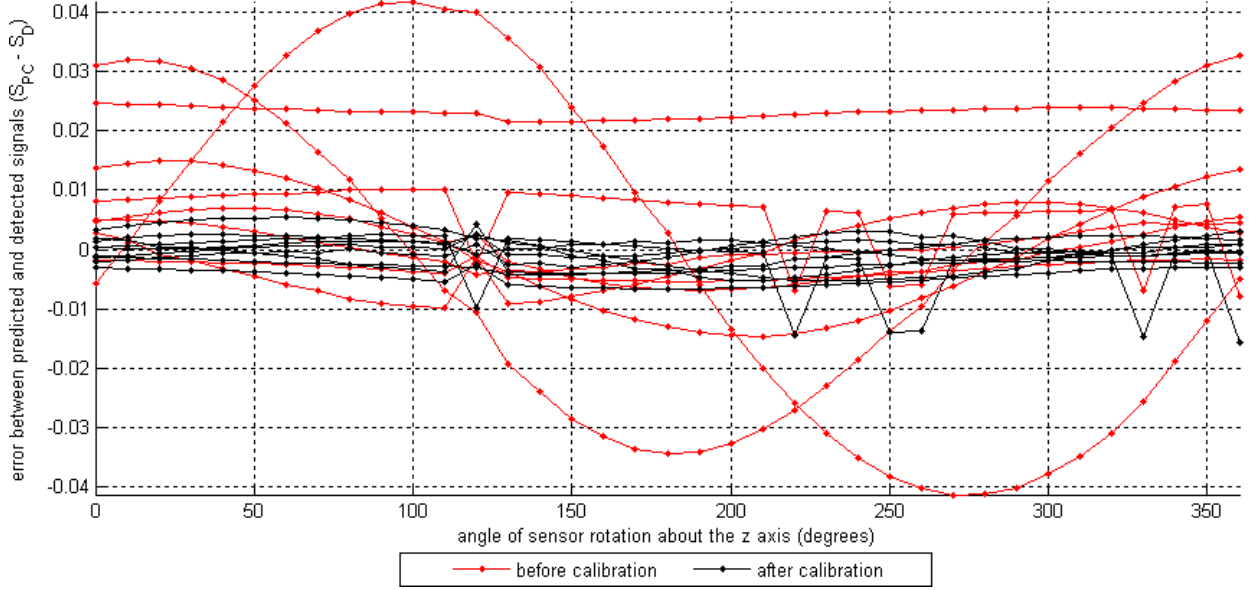


Figure 7.7: Matching the theoretical and practical models for the coils.

7.4 Practical Data Calibration

The calibration method outlined in Section 7.3.1 described a method of matching a theoretical model of the signals S_{PC} to the detected signals S_D . The inverse process may be applied to S_D to compensate for system distortions and allow the position and orientation algorithms to be applied to the detected signals. The relationship developed in equation 7.8 can be used to obtain a calibrated detected signal matrix S_{CD} as shown in equation 7.10.

$$S_{CD} = D_{SRC}^{-1} S_D D_{NSR}^{-1} \quad (7.10)$$

This method requires that two matrix inverse calculations be performed, however the risk of singularity is relatively low as the calculation need only be performed once (at the time of coil calibration) and the data used for calibration must be very accurate and free of noise. D_{SRC} will be nonsingular as it is a diagonal matrix which must contain nonzero diagonal elements in order to allow the signals detected from each excitation to be resolved. It is unlikely that D_{NSR} will be singular as this would require that two sensor coils are perfectly coupled (that is coaxially aligned in space and have a mutual inductance of unity) and share exactly the same mutual inductance with the third coil.

The application of equation 7.10 to the detected signals S_D obtained from the source and

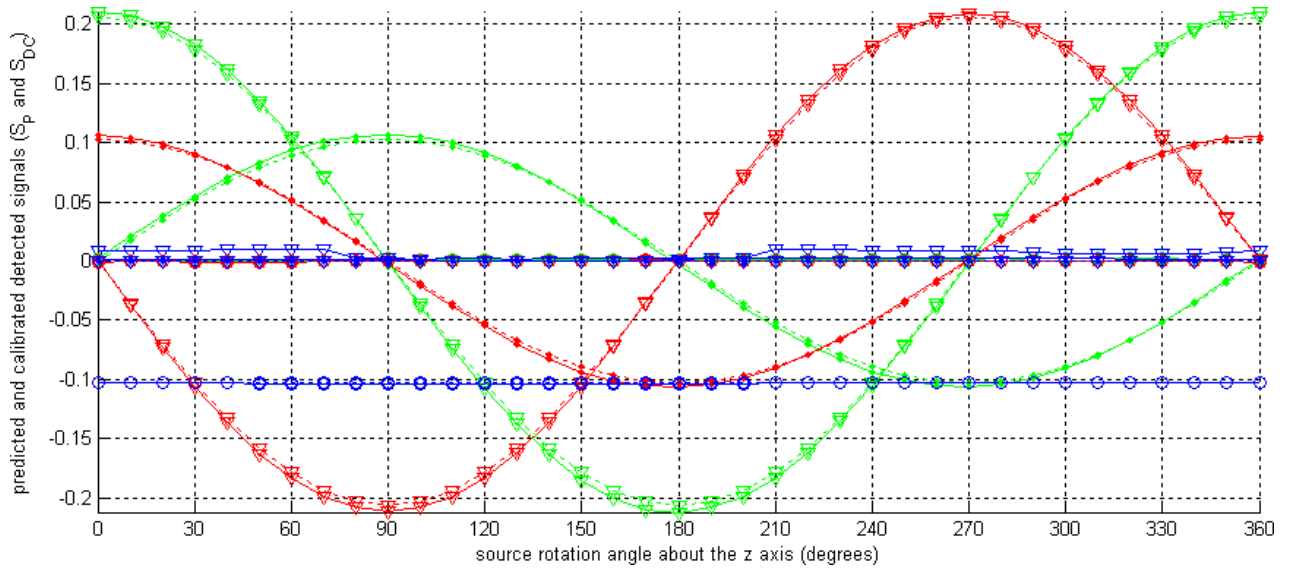


Figure 7.8: Comparison of the calibrated measured magnetic fields with the theoretical model for the source rotation test jig.

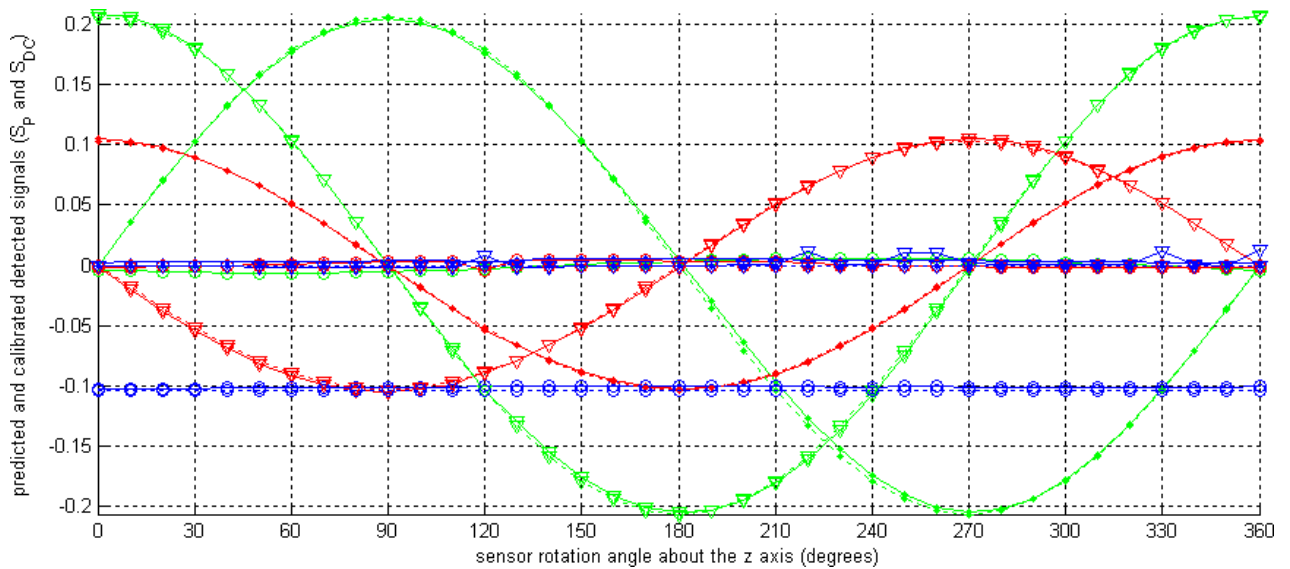


Figure 7.9: Comparison of the calibrated measured magnetic fields with the theoretical model for the sensor rotation test jig.

sensor rotation test jigs in Figures 7.8 and 7.9 demonstrates the effectiveness of calibration on the detected signals. The signals predicted by equation 7.1 are dashed, while the calibrated detected signals calculated from equation 7.10 are solid. The degree of fit provided by the calibration methods shows a good improvement on the differences between the results of Figures 7.3 and 7.5, however differences between the predicted and calibrated detected signals are still apparent. It is possible that the source of the remaining errors is primarily the position offsets in the source and sensor, which cause more or less magnetic field to be detected depending on the position and orientation of the sensor relative to the source. Some amplitude offsets are also apparent, and these may be due to the effects of mutual inductance between the source coils, however without a detailed analysis it is difficult to confirm the cause.

The MSE between the calibrated measured signals and the predicted signals in the source and sensor rotation test jigs were 3.9×10^{-4} and 3.4×10^{-4} . The MSE values resulting from the calibrated signals detected on the test jigs require still significant reduction in order to allow the resolved position and orientation measurements to meet the specified accuracy requirements, a subject that is discussed further in chapter 8.

7.5 Tracking Speed and Update Rate

The samples illustrated in Figures 7.8 and 7.9 were obtained from a set of 10 ‘magnitude averaged’ measurements to minimize the effects of noise. The polarity of each sample was assigned according to the polarity of the majority of the 10 sample set (as described in Section 4.3.3) with equal majority measurements of 5 positive and 5 negative samples being assigned a negative polarity. Although this reduced the effect of errors within the magnetic field measurements, the increased computation significantly affected the tracking speed and update rate. The update rate for the position and orientation calculation (without averaging) was 65 updates per second, however the overhead required for averaging the data lowered the update rate to 40 updates per second. Code profiling was not available due a lack of support by the JTAG debugger, however because a poll waiting method was used to acquire the data, the measurements were calculated sequentially and had an average latency of 15 milliseconds. This latency value may be calculated by inference - if the update rate of a polled system is 65 updates per second then 15 milliseconds is the average time which is required by the PADK to wait for, sample and process each Fastrak signal. Although these specifications are significantly lower than that of the Fastrak, adjustments to the software implementation may result in significant performance improvements as will be outlined in Chapter 8.

Chapter 8

Tracking System Performance

The performance analysis of a tracking system must take into account the accuracy, resolution, update rate and latency - all of which are stated in Table 1.1 for the Polhemus Fastrak. These specifications represent the minimum design requirements that must be met for all position and orientation measurements over the range in which the tracking system is specified to operate (760 mm). The latency and update rate can be improved by using more efficient processing techniques while the resolution may be enhanced with low noise circuitry and advanced filtering systems. An increase in accuracy is more difficult to achieve, however, as it is affected by bias which can be introduced through incorrect calibration or noise within the system. The methods of measuring the accuracy outlined by Polhemus [Polhemus (2004)] is used to determine the system performance, however a slightly different resolution specification is used due to the incomplete description provided by Polhemus.

8.1 Resolution

The translational and angular resolution specify the smallest resolvable changes in sensor position and orientation. In the context of AC magnetic tracking the resolution represents the smallest difference that may be determined between two measurements before those measurements are obscured by noise. Thus, because the precision is a measure of the spread of repeated measurements, the translational and angular resolution of the system depends on the precision of the calculated position and orientation.

The relationships between the detected magnetic fields and the position and orientation measurements can be complex and as a result, the relationships between the noise in the detected magnetic fields and the noise in the position and orientation measurements can also

be complex. One approach to solve this problem is to use a ‘black box’ testing method. The resolution is measured at a number of different sensor locations to determine the translational and angular resolution at a given range.

8.1.1 Translational Resolution.

The translational resolution represents the smallest difference in sensor position which may be determined for a given range r . It can be calculated as the root mean square (RMS) of the variance in all three position coordinates as shown in equation 8.1.

$$\text{Translational Resolution at } r = \sqrt{\sigma_x^2 + \sigma_y^2 + \sigma_z^2} \tag{8.1}$$

where σ_x , σ_y and σ_z are equal to one standard deviation of the spread of the x , y and z position coordinates respectively. Thus, because the position coordinates are calculated from the detected magnetic fields which decrease in SNR with an inverse cube relationship to r , the variation in the resolved position coordinates will increase in a manner proportional to r^3 as shown in Figure 8.1.

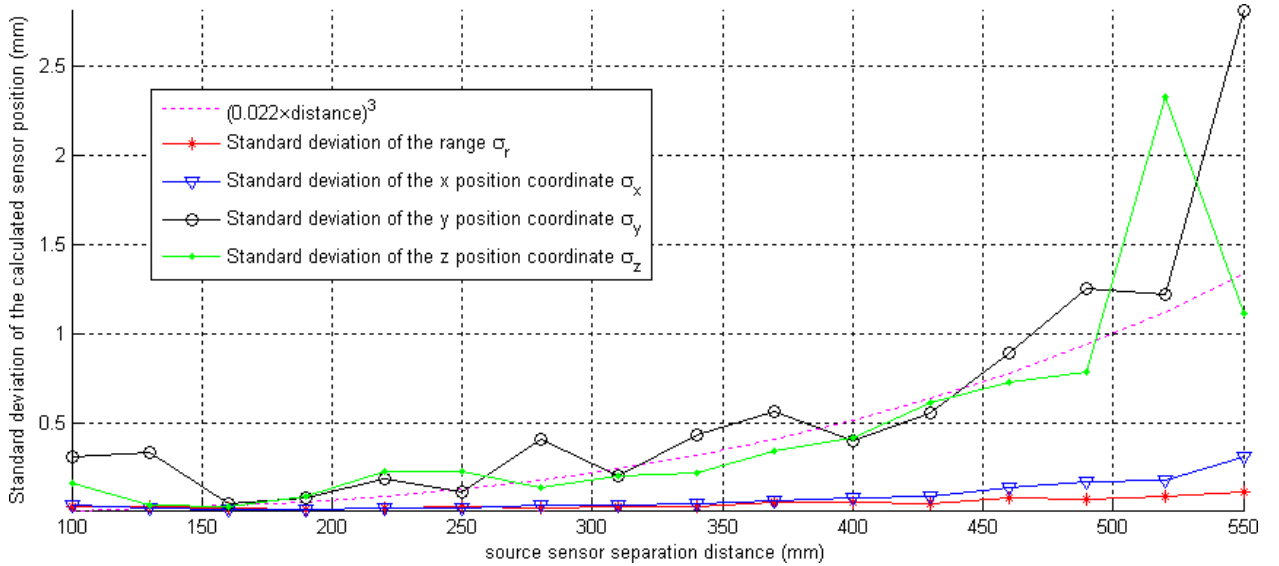


Figure 8.1: Variation in the resolved position coordinates as the sensor position is varied along the x axis of the source frame.

The definition of translational resolution in equation 8.1 differs from the definition stated by Polhemus Ltd [Polhemus (2004)] and although it is only specified for a single range, it is a clearer method which has been used by others when analyzing tracking systems [Rousseau

(2002)]. The variation in the position coordinates may be reduced by averaging the detected magnetic field measurements the standard deviation of which can be calculated by dividing the standard deviation of the sample set by the square root of the number of samples over which the average has been calculated [McClave (2000)]. Thus, because the position coordinates are calculated from the detected magnetic fields, the variation in the resolved position coordinates will also decrease.

$$\sigma_{BN} = \frac{\sigma_B}{\sqrt{N}} \quad (8.2)$$

where σ_B is equal to one standard deviation of the variance in the measured magnetic fields and σ_{BN} represents one standard deviation of the measured magnetic fields after an N sample time average has been applied. The translational resolution of the tracking system was analyzed by collecting 10000 static position coordinates calculated from raw and averaged magnetic field measurements. Three sets of position coordinates were collected for comparison and were calculated using raw magnetic field measurements ($N = 1$), magnetic fields measurements averaged over 10 samples ($N = 10$), and magnetic field measurements averaged over 100 samples ($N = 100$) as shown in Figure 8.2.

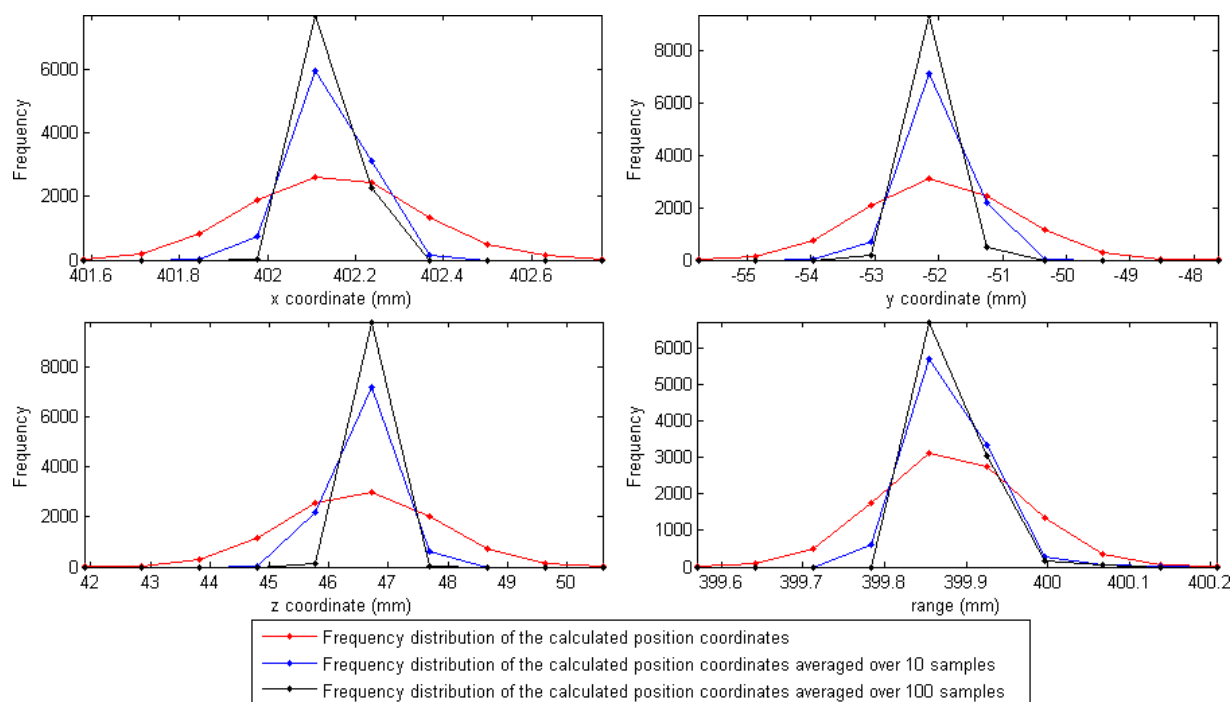


Figure 8.2: Frequency distribution of 10000 position measurements at a sensor position of (400,0,0) with a 270° rotation about the z axis with respect to the source frame.

8. TRACKING SYSTEM PERFORMANCE

The method outlined in equation 8.1 was used to determine the translational resolution of the position measurements at different sensor positions along the x axis of the source frame, as shown in Figure 8.3.

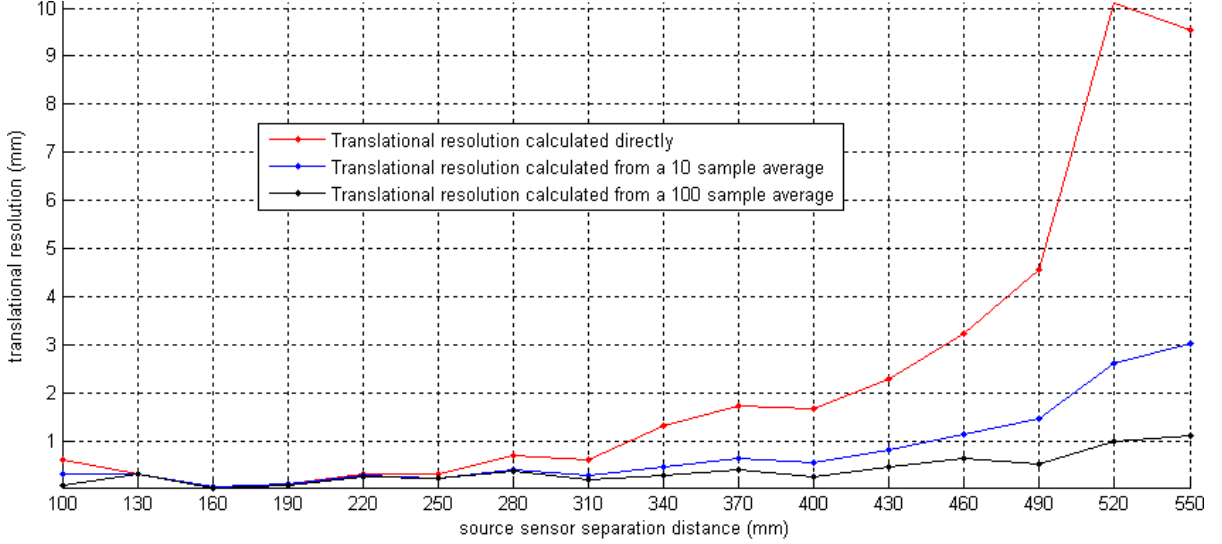


Figure 8.3: Variation of translation resolution with range r .

The choice of sensor position is important when conducting such measurements as the translational resolution will change according to the SNR of the detected magnetic fields which vary according to the source and sensor coil coupling. The samples were collected at a reference position of (400mm,0mm,0mm) with an orientation of (0°,0°,270°) - the initial position of the source and sensor rotation test jigs in Chapter 7.

	σ_x	σ_y	σ_z	σ_r
Unfiltered resolution	0.2 mm	1.1 mm	1.2 mm	0.09 mm
Filtered resolution (N = 10)	0.07 mm	0.4 mm	0.4 mm	0.04 mm
Filtered resolution (N = 100)	0.04 mm	0.2 mm	0.2 mm	0.03 mm

Table 8.1: Translational resolution of the resolved position coordinates for a sensor located at (400mm,0mm,0mm) with an orientation of (0°,0°,270°).

The translational resolution of the system calculated from Table 8.2 and equation 8.1 was 1.7mm, however this could be improved to 0.6mm with a 10 sample time average of the magnetic fields and further improved to 0.3mm with a 100 sample time average.

8.1.2 Angular Resolution

The angular resolution of the tracking system represents the smallest possible orientation measurement which may be resolved and is dependent upon the SNR of the detected magnetic fields. The method of orientation calculation described in equation 5.37 involves matrix inversion and relies on accurate calculation of the sensor position in order to determine the predicted signal matrix B_P . The introduction of noise therefore affects both the detected signal matrix B_D and the predicted signal matrix in the orientation calculation. The effects of this are not straightforward to analyze. Figure 8.4 illustrates the frequency distribution of the resolved Euler angles α , β and γ for both rotation sequence solutions to R . The resolved Euler angles were calculated from a sample set of 10000 raw magnetic field measurements ($N = 1$), magnetic fields measurements averaged over 10 samples ($N = 10$), and magnetic field measurements averaged over 100 samples ($N = 100$).

Equation 8.3 was used to determine the angular resolution of the tracking system.

$$\text{Angular Resolution at } r = \sqrt{\sigma_\alpha^2 + \sigma_\beta^2 + \sigma_\gamma^2} \quad (8.3)$$

where σ_α , σ_β and σ_γ are equal to one standard deviation of the variation in the resolved α , β and γ angles respectively. Equation 8.3 is valid provided the variations in the angles about their mean values are relatively small.

The calculation of the sensor orientation requires that both the magnitude and polarity of the detected magnetic fields and the sensor position be known. The polarity estimation method described in Section 4.3.3 was not robust, and thus at positions for which the SNR of the detected magnetic fields was small the direction of the magnetic fields could be incorrectly estimated causing an invalid orientation to be calculated. This caused difficulties in the analysis of the system resolution as incorrect polarity estimation often resulted in the generation of a completely different rotation sequence causing the resolved Euler angles to vary significantly. Such errors can be minimized by improvement of the polarity estimation technique. The calculated variations in α , β and γ for the sensor position (400mm,0mm,0mm) and an orientation of (0°,0°,270°) are shown in Table 8.2.

From these values, the angular resolution of the tracking system was calculated as 0.63°. This could be reduced to 0.16 ° by averaging the detected magnetic fields using a 10 sample average, and reduced further to 0.014° by using a 100 sample average.

8. TRACKING SYSTEM PERFORMANCE

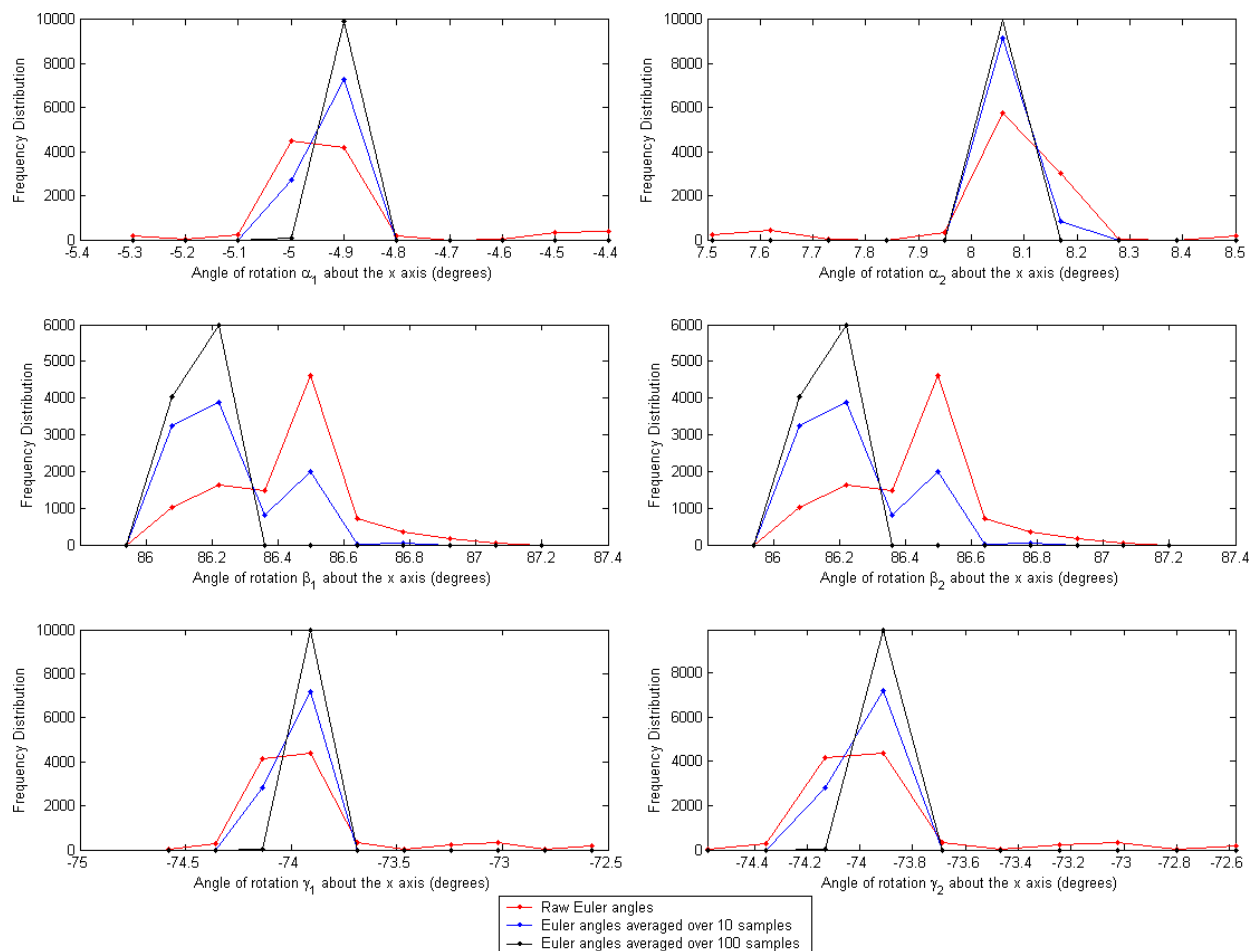


Figure 8.4: Frequency distribution of 10000 Euler angle measurements at a sensor position of (400mm,0mm,0mm) and an orientation of $(0^\circ, 0^\circ, 270^\circ)$ with respect to the source.

8.2 Accuracy

The tracking accuracy represents the error between the position and orientation values calculated by the tracker and the true sensor position and orientation. The translational and angular accuracy are therefore one of the most important specifications for a tracking system, however due to the complexity of the algorithms it is appropriate to use ‘black box’ testing methods to resolve the accuracy at a number of positions and determine a final value. Static position and orientation values calculated from a set of averaged magnetic field measurements were obtained for a number of sensor positions to determine the translational and angular accuracy specifications for the system.

	σ_α	σ_β	σ_γ
Unfiltered resolution	0.3°	0.2°	0.5°
Filtered resolution (N = 10)	0.02°	0.2°	0.05°
Filtered resolution (N = 100)	0.006°	0.004°	0.05°

Table 8.2: Standard deviation of the resolved Euler angles for a sensor located at (400mm,0mm,0mm) with a rotation of (270°,0°,0°).

The accuracy was calculated from three data sets at a total of 106 sensor positions. This included 37 positions in the source rotation test jig (0° → 360° in 10° intervals), 37 positions in the sensor rotation test jig (0° → 360° in 10° intervals) and 32 positions along the x axis of the source frame (100mm→565mm in 15mm intervals). At each location the position and orientation were resolved using a 100 sample average of the detected magnetic fields and were compared to the position coordinates (α_M , β_M , γ_M) and angles of rotation (α_M , β_M , γ_M) measured directly from the test jig.

8.2.1 Translational Accuracy

The translational accuracy of the tracking system is dependent upon the validity of the calibration parameters and the SNR of the detected magnetic fields. The translational accuracy was calculated as the root mean square error between the actual measurement value and that calculated by the tracking system using equation 8.4.

$$\text{Translational Accuracy} = \sqrt{\Delta x^2 + \Delta y^2 + \Delta z^2} \quad (8.4)$$

where Δx , Δy and Δz are the RMS errors in the x , y and z position coordinates determined from the measurements at a number of sensor locations. The error in each position coordinate may be calculated using equation 8.5.

$$\Delta x = \sqrt{\frac{\sum_{i=1}^{106} (x_{iM} - \bar{x}_i)^2}{106}} \quad \Delta y = \sqrt{\frac{\sum_{i=1}^{106} (y_{iM} - \bar{y}_i)^2}{106}} \quad \Delta z = \sqrt{\frac{\sum_{i=1}^{106} (z_{iM} - \bar{z}_i)^2}{106}} \quad (8.5)$$

where x_{iM} , y_{iM} and z_{iM} are the known x , y and z position coordinates at the i^{th} position and \bar{x}_i , \bar{y}_i and \bar{z}_i are the time average of 100 calculated position coordinates x , y and z resolved at the i^{th} position. Figure 8.5 illustrates the measured position magnitude as the source was rotated clockwise about the z axis from (0°,0°,270°) in 10° increments.

8. TRACKING SYSTEM PERFORMANCE

As the sensor becomes aligned with an axis the errors in the position coordinates orthogonal to that axis become significant. Hence, at 0° and 180° the sensor is aligned along the x axis, and the position coordinate errors Δy and Δz increase, reflecting a greater sensitivity to noise in the magnetic fields as a position coordinate approaches zero. The resolved position coordinate along the z axis remains below zero throughout the duration of the source rotation. This is a result of small error in the calibration of the detected magnetic fields which causes the argument of the square root (in equation 5.9) to be slightly less than zero. The z calculated position has been correspondingly calculated as a real negative number, the reasons for which will be explained later. Multiplication by r causes this error to increase and because the source sensor coupling along the z axis does not change, the error remains constant.

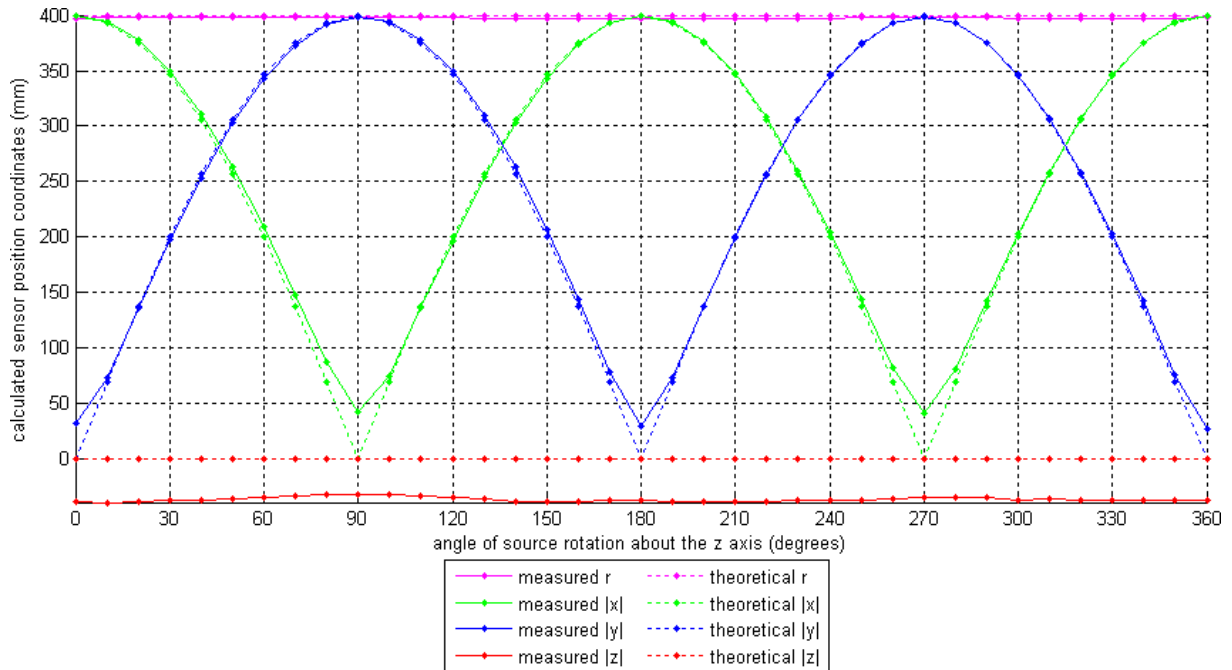


Figure 8.5: Sensor position coordinates calculated from the source rotation test jig.

The total magnitude of the magnetic field detected by the sensor at a fixed range r will be smallest for positions in which the sensor is in coplanar alignment with a source coil and largest for positions in which the sensor is in coaxial alignment (as shown in Figure 7.4). If an approximately equal amount of noise is present in all magnetic field measurements at the same range, the SNR in the detected magnetic fields will correspondingly be highest when the sensor is in coaxial alignment with a source coil (equivalent to a position coordinate of r), and smallest when the sensor is in coplanar alignment with a source coil (equivalent to a position coordinate of 0). Furthermore as the range r increases the SNR of the detected mag-

netic fields will decrease causing an increase in variation in the estimated x , y and z position coordinates. This effect should not however affect the accuracy which is calculated from \bar{x} , \bar{y} and \bar{z} (assuming the number of samples over which the average is taken is sufficiently large).

Averaging the detected magnetic fields before calculating the position coordinates eliminates the amplification of the error ΔB by the size of the field B , reducing the overall averaged error in the system. The impact of averaging is particularly important if the position coordinates are averaged rather than the magnetic fields. The presence of noise within the position calculation can cause the argument of the square root to be negative and therefore the implemented code must use the absolute value of the argument to prevent a complex position coordinate from being resolved. This is shown in equation 8.6.

$$\text{argument} = \frac{1}{3} \left(\frac{\mu_o m B_Z^2}{4\pi r^3} - 1 \right) \quad \frac{z}{r} = \sqrt{\left| \frac{1}{3} \left(\frac{\mu_o m B_Z^2}{4\pi r^3} - 1 \right) \right|} \quad (8.6)$$

Thus, as the resolved value of x is restricted to positive values, any averaging process will bias the mean and cause all argument values that might be below zero to be mirrored into the positive domain as shown in Figure 8.6.

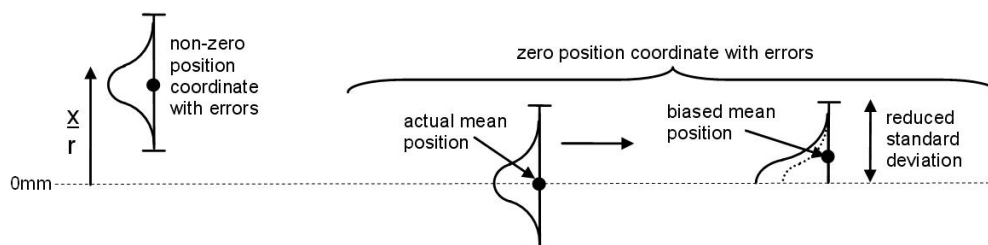


Figure 8.6: Average and Statistical Range Variation with Sensor-Source Separation

Such bias effects may be eliminated by allowing a negative position to be applied to the result when the argument is less than zero thereby eliminating the mean bias and correcting the output. Thus the position coordinates may be averaged, but if careful consideration is not given to the method of calculation, a bias will be introduced when a position coordinate approaches zero. The resulting position coordinate errors Δx , Δy and Δz reflect the system dependence on the SNR of the detected magnetic fields. The RMS error of each position coordinate was calculated from the data collected from the source rotation test jig and is shown in Table 8.3.

The error in the z coordinate reflects the effects of low SNR signals on the calculation of the

8. TRACKING SYSTEM PERFORMANCE

	Δx	Δy	Δz	Δr
Source rotation test jig coordinate errors	11.0mm	8.9mm	37.2mm	2.2mm
Sensor rotation test jig coordinate errors	1.6mm	41.1mm	39.4mm	0.8mm
Direction test jig coordinate errors	1.9mm	34.3mm	29.8mm	1.8mm

Table 8.3: Translational accuracy of the resolved sensor position coordinates.

position coordinates while the range calculation illustrates that if the SNR is high, accuracy of the order of 2mm can be achieved. The sensor position coordinates alternate between $|x| = r, |y| = 0$ and $|x| = 0, |y| = r$ as the source is rotated and thus the RMS errors Δx and Δy are between 2.2mm and 37.2mm.

These observations are also apparent in the results obtained from the sensor rotation test jig. During the sensor rotation the sensor was located along the x axis at (400mm,0mm,0mm) resulting in large Δy and Δz position coordinate errors but a minimal Δx position coordinate error as shown in Figure 8.7.

The accuracy specifications for the tracking system were required to apply for all regions within the tracking space. Thus as the range increases the variations in the position measurement may increase but the mean of each position coordinate resolved should remain unbiased. The error in the x position coordinate Δx demonstrates that for positions in which the SNR is high (which correspond to magnetic fields coaxially aligned with the axis), the position coordinate errors (Δx) will be small. At positions for which the SNR is small the resulting position coordinate errors (Δy and Δz) will be significant.

The variation in the translation accuracy with range was tested by holding the sensor orientation constant as the range was increased across available source-sensor separation distances as shown in Figure 8.8.

The results illustrate that the decreasing SNR of the detected magnetic fields significantly affects the accuracy of position coordinates close to zero, but has minimal effect on the accuracy of position coordinates which approach r . The position coordinate error along the x axis Δx does not show any significant difference in accuracy whether $r = 100\text{mm}$ or $r = 565\text{mm}$ whereas the errors within the y and z position coordinates are significantly affected by the increase in range and corresponding decrease in the SNR of the detected magnetic fields. The error within the y position coordinate Δy appears to increase in a manner proportional to r^3 ,

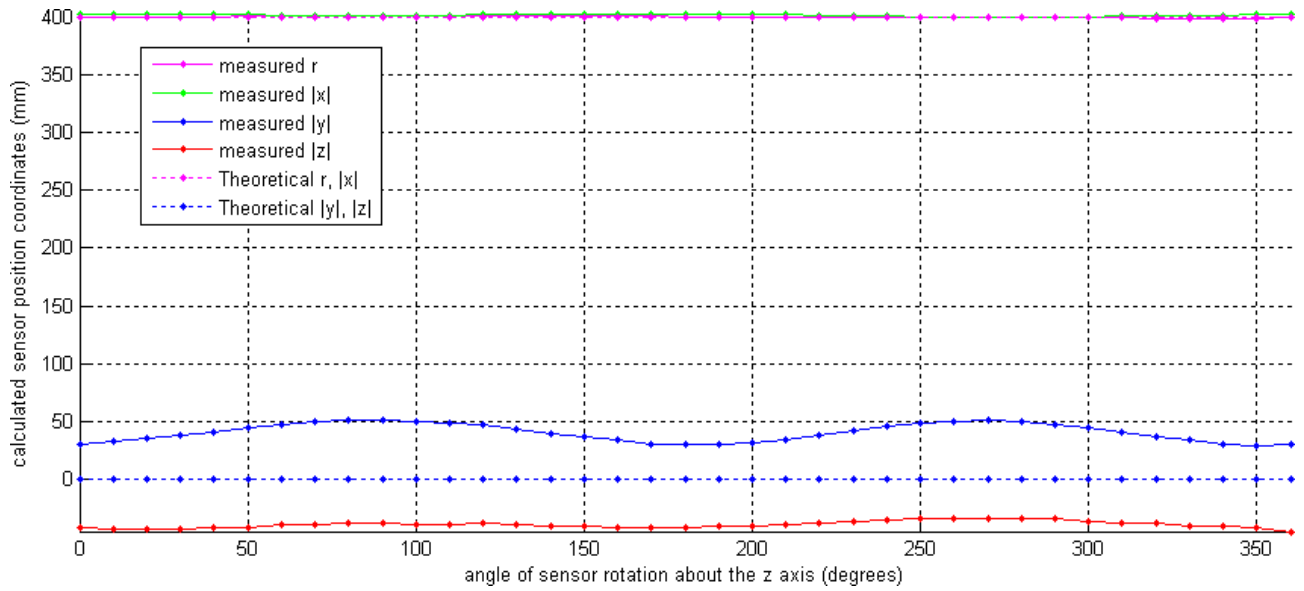


Figure 8.7: Calculated sensor position as the sensor is rotated 360° clockwise from $(90^\circ, 0, 0)$

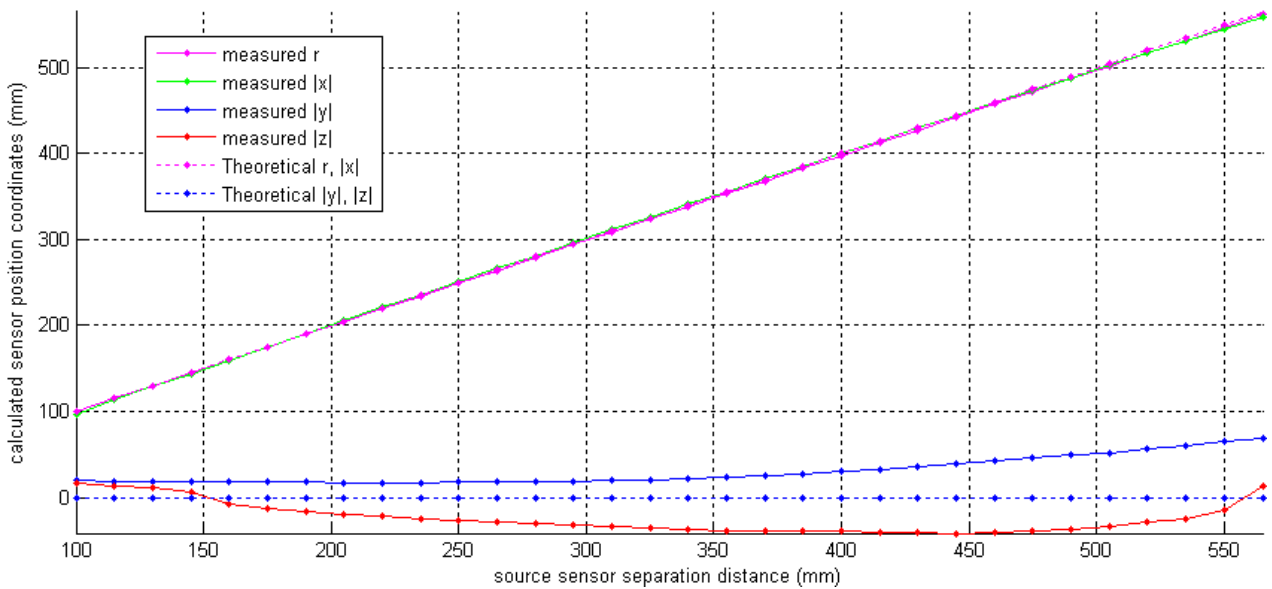


Figure 8.8: Position coordinates resolved as the sensor moves from $(100\text{mm}, 0\text{mm}, 0\text{mm})$ to $(565\text{mm}, 0\text{mm}, 0\text{mm})$ in 15mm increments at an orientation of $(0^\circ, 0^\circ, 270^\circ)$.

while the error within the z position coordinate Δz is also significantly affected but differs in behavior due to the presence of a small calibration imperfection.

The dependence of the position coordinate errors Δx , Δy and Δz illustrate that the SNR of the detected magnetic only affects the calculation of position coordinates close to zero and that the errors in position coordinates close to r will be largely immune to such effects. The position coordinate error along the x axis Δx does not show any significant difference between the largest and smallest source-sensor separation distances in spite of the SNR of the detected magnetic fields decreasing with an inverse cube relationship. Thus, as the SNR of the detected magnetic fields used to calculate x at $r = 550\text{mm}$ will be less than the SNR of the magnetic fields used to calculate the y and z coordinates at $r = 100\text{mm}$ the effects of SNR in the detected magnetic fields have significant effects. This is also reflected in the behavior of the resolved y and z position coordinates which appear to increase in bias in a manner proportional to r^3 . Although the Δz position coordinate error increases, the behavior is different to that of Δy as the argument becomes positively biased from its previously negative value.

The translational accuracy of the tracking system (calculated from all three test jigs) is 47.9mm and is equal to the RMS accuracy of the Δx , Δy and Δz position coordinate errors in all three test jigs. This value is large primarily due to the position coordinates at which the magnetic fields were detected, all of which contained at least one zero position coordinate ($x = 0$, $y = 0$ or $z = 0$).

8.2.2 Angular Accuracy

The accuracy of the orientation calculation is dependent upon the translational accuracy as the position coordinates are used to predict the magnetic fields at the sensor position. Thus, unless the position calculation is accurate the magnetic fields will be predicted for a different position affecting the calculated orientation. The sensor orientation was therefore analyzed using two different methods, the first used the detected magnetic fields to calculate B_P and B_D for determination of the sensor orientation, while the second used a corrected sensor position (an ideal B_P) and the detected magnetic fields B_D . The angular accuracy from each of the test jigs was determined by calculating the RMS error for a number of sensor positions

and orientations using equation 8.7.

$$\Delta\alpha = \sqrt{\frac{\sum_{i=1}^{106}(\alpha_{iM} - \bar{\alpha}_i)^2}{106}} \quad \Delta\beta = \sqrt{\frac{\sum_{i=1}^{106}(\beta_{iM} - \bar{\beta}_i)^2}{106}} \quad \Delta\gamma = \sqrt{\frac{\sum_{i=1}^{106}(\gamma_{iM} - \bar{\gamma}_i)^2}{106}} \quad (8.7)$$

where $\Delta\alpha$, $\Delta\beta$ and $\Delta\gamma$ are the RMS errors in the α , β and γ Euler angles determined at each sensor location and α_{iM} , β_{iM} and γ_{iM} are the Euler angles of sensor orientation measured from the test jig at the i^{th} position, and $\bar{\alpha}_i$, $\bar{\beta}_i$ and $\bar{\gamma}_i$ are the mean of each of the angles at each position. Figure 8.9 illustrates the resolved Euler angles α , β and γ from the source rotation test jig at $r = 400\text{mm}$.

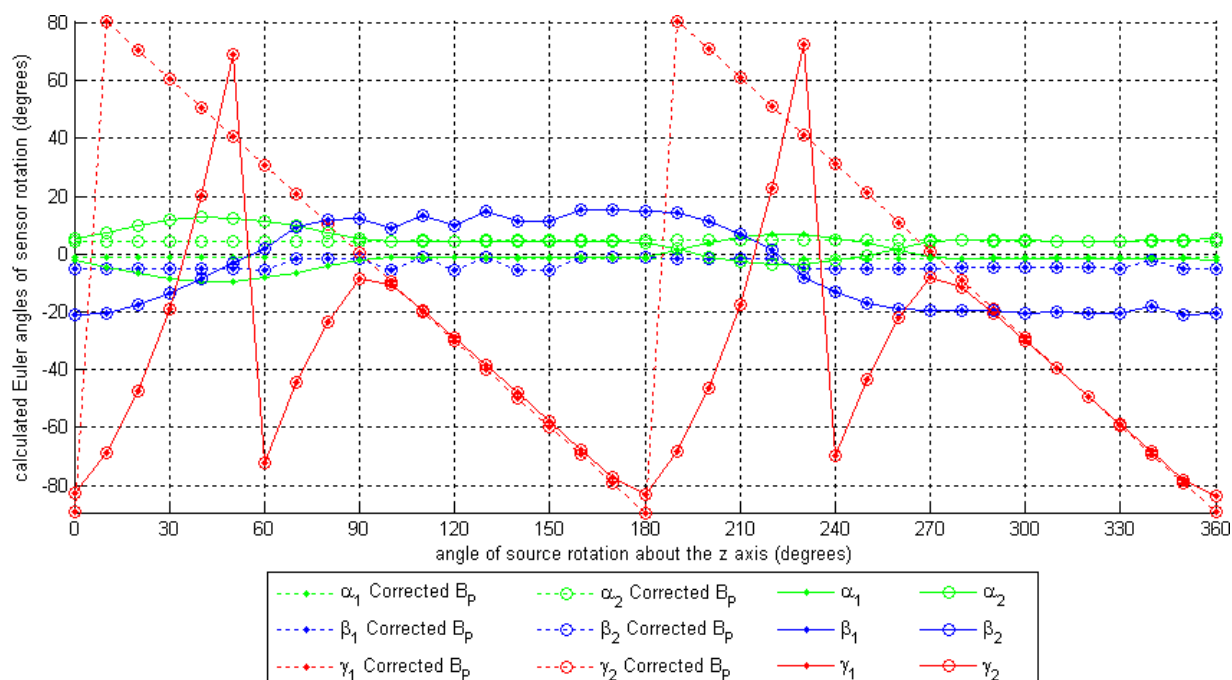


Figure 8.9: Euler angles of sensor rotation from the sensor rotation test jig calculated from the detected magnetic fields and the resolved position coordinates.

The position magnitude was used to calculate the predicted signal matrix B_P , and thus at sensor positions for which the sensor position coordinates were negative, the incorrect position coordinates were used to calculate B_P causing an invalid orientation to be resolved. This is apparent in the resolved Euler angles when the source is rotated between $0^\circ \rightarrow 90^\circ$ and $180^\circ \rightarrow 270^\circ$. The accuracy of the Euler angles resolved from the positive quadrant $270^\circ \rightarrow 360^\circ$ showed excellent agreement with the orientation measurements calculated from

8. TRACKING SYSTEM PERFORMANCE

an ideal position. The Euler angles resolved from the $90^\circ \rightarrow 180^\circ$ quadrant were calculated for the quadrant ($z = 0, -x, -y$) and therefore detected identical magnetic fields to the ($z = 0, +x, +y$) quadrant allowing the correct Euler angles to be resolved. The collective errors from the other negative quadrants significantly reduced the accuracy however as shown in Table 8.4 which compares the errors resulting from direct calculation of the Euler angles and those arising based on calculation of the Euler angles given an exact knowledge of the sensor position.

	$\Delta\alpha$	$\Delta\beta$	$\Delta\gamma$
Error in calculated Euler angles	4.2°	15.2°	56.5°
Error in corrected Euler angles	1.4°	4.2°	0.7°

Table 8.4: Accuracy of the resolved Euler angles for the sensor measurements obtained from the source rotation test jig.

Thus, although these errors are significant, they do not represent the true accuracy of the orientation algorithm but rather the effects of an incomplete implementation of the position calculation. A fairer estimate of the orientation algorithm may be determined by using the angles between $90^\circ \rightarrow 180^\circ$ and $270^\circ \rightarrow 360^\circ$ or by using the orientation calculated from the measured sensor position. This reduces the error in the resolved angles significantly. The sensor rotation test jig also demonstrated the dependence of the orientation algorithm on an accurate position being resolved as shown in Figure 8.10.

The sensor position remained aligned along the positive x axis of the source frame and thus the position polarity did not affect the resolved Euler angles however the position coordinate offsets at the measured positions were significant. The Δy and Δz position coordinate offsets resulting from the sensor position being aligned along the x axis distorted the predicted magnetic field matrix B_P and correspondingly affected the resolved Euler angles. The Euler angles calculated using the correct position yielded good agreement with the ideal Euler angles as shown in Table 8.5.

The position offsets in the Euler angles resolved from the source and sensor rotation test jigs remained relatively constant but began to show a slight increase as the range became larger. Figure 8.11 illustrates the resolved Euler angles of rotation as the sensor position was varied between 100mm and 550mm along the x axis of the source frame. The $\Delta\beta$ and $\Delta\gamma$ errors in the resolved β and γ angles were primarily caused by offsets in the calculated position coordinates and are eliminated by use of the correct position coordinates as shown

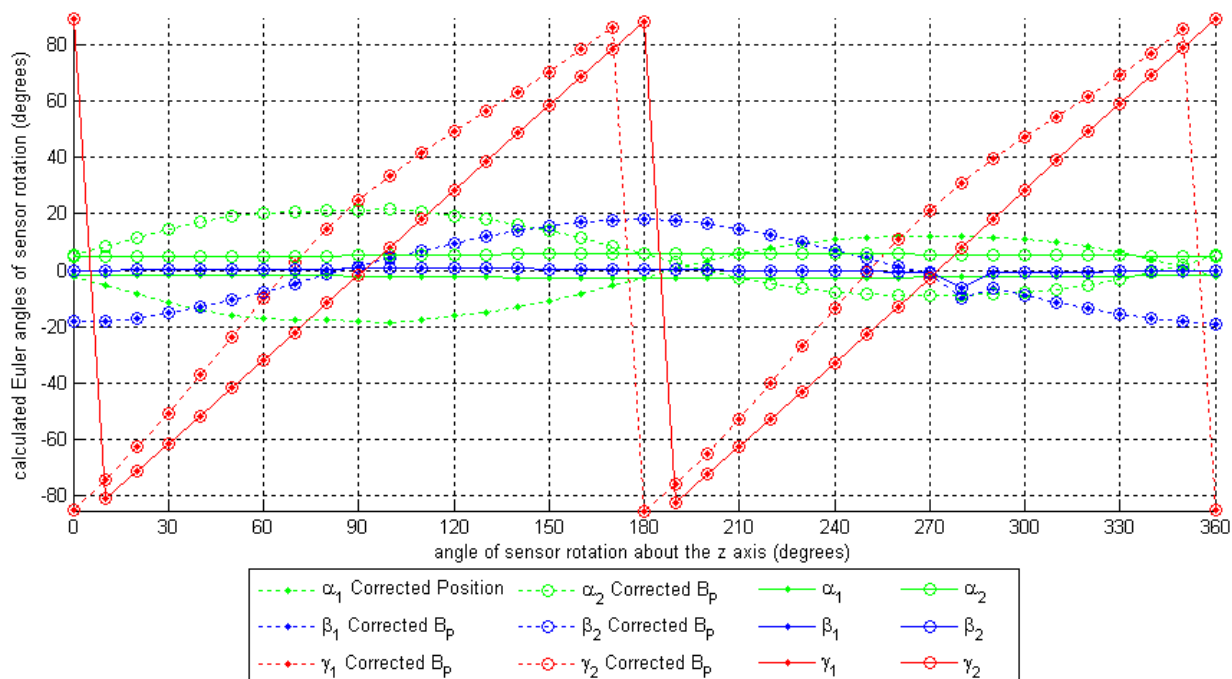


Figure 8.10: Euler angles of sensor rotation from the sensor rotation test jig calculated from the detected magnetic fields and corrected position coordinates.

	$\Delta\alpha$	$\Delta\beta$	$\Delta\gamma$
Error in calculated Euler angles	12.5°	12.8°	52.0°
Error in corrected Euler angles	5.4°	1.2°	1.9°

Table 8.5: Accuracy of the resolved Euler angles for the sensor measurements obtained from the sensor rotation test jig.

in Table 8.6. The $\Delta\alpha$ angular error in the α angle is not due to position offsets (distortion also occurs within the Euler angles α calculated from the correct position) and it is possible that aperture effects are the source of this distortion. The angular accuracy calculated from the measured positions on all three test jigs is 54.4°. This was improved to 24.3° by using accurately determined position coordinates to construct the predicted signal matrix B_P .

8.2.3 Increasing the Tracking Accuracy

The results obtained from the tracking system illustrated the validity of the algorithms and often produced an accurate agreement with the true sensor position and orientation. The levels of accuracy attained are not at a commercial standard however, and a number of

8. TRACKING SYSTEM PERFORMANCE

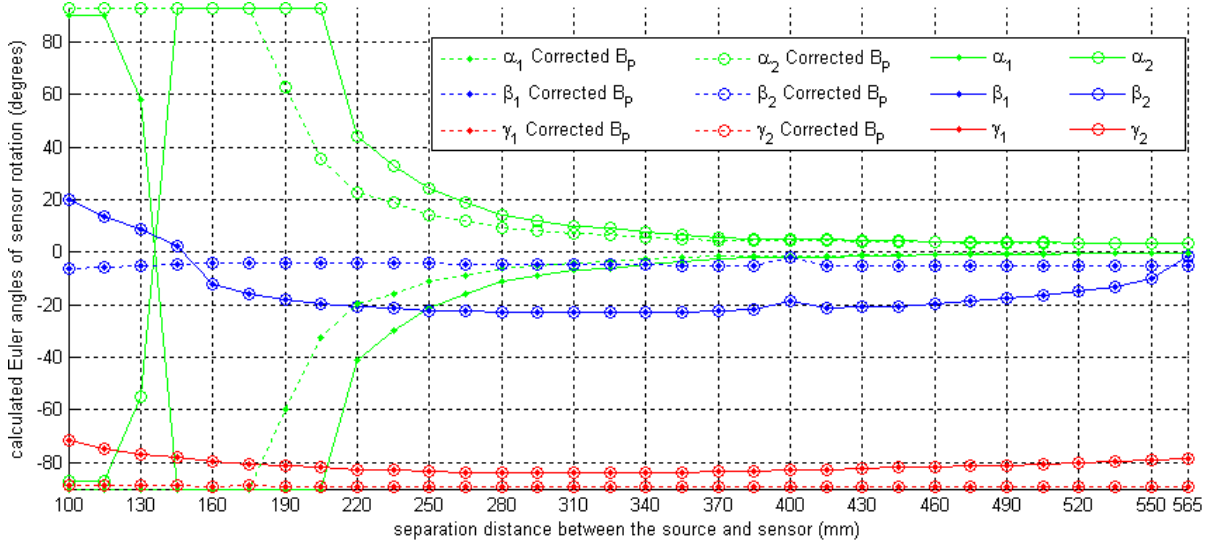


Figure 8.11: Euler angles of sensor rotation calculated as the sensor moves away from the source.

	$\Delta\alpha$	$\Delta\beta$	$\Delta\gamma$
Error in calculated Euler angles	44.6°	18.7°	9.2°
Error in corrected Euler angles	41.1°	4.8°	0.9°

Table 8.6: Accuracy of the resolved Euler angles for the sensor measurements from all test jigs.

improvements are required. The most important area of improvement is the translational accuracy as this is a fundamental specification and it is from the resolved position that the Euler angles are calculated. The position coordinate errors which are apparent when a position coordinate approaches zero may be reduced by using Pythagoras theorem to relate the resolved values of x , y , z and r . An increase in accuracy is possible because the SNR of r is always larger or equal to the SNR of any of the position coordinates (calculation of a position coordinate requires multiplication by r), and thus at sensor positions for which a position coordinate is close to zero equation 8.8 may be used to increase the translational accuracy.

$$1 = \left| \frac{x}{r} \right|^2 + \left| \frac{y}{r} \right|^2 + \left| \frac{z}{r} \right|^2 \quad (8.8)$$

In addition to this, improvements to the polarity estimation technique may be made by implementing a system which controls both generation and detection of the magnetic fields. If the polarity of the detected magnetic fields can be resolved more accurately then the

magnetic fields close to zero may be averaged allowing a significant reduction in the bias errors introduced through ‘magnitude averaging’. A final area of improvement worth noting is the calibration of the aperture effects. It appears that such effects distort the resolved Euler angles for positions in which the range is less than 250mm. Such an improvement would significantly reduce the angular error, however an accurate calculation of the sensor position would still be required.

8. TRACKING SYSTEM PERFORMANCE

Chapter 9

Discussion and Conclusions

The thesis provides a broad but relatively brief description of the operation and design of an AC magnetic tracking system. While the project began with a literature review of the relevant academic papers and the patents of all previously proposed systems, more focus was given to research relating to operational tracking systems and their functionality. From this perspective an investigation of the Polhemus Fastrak was a natural choice for the subject of research given its availability, high performance characteristics and the detailed patents outlining its theory of operation. An analysis of the Fastrak operation was completed which included a thorough review of the relevant patents and a detailed hardware analysis from which an understanding was gained of the signal generation and detection mechanisms.

A method of implementing a tracking system in conjunction with the Fastrak was devised and the appropriate components for the amplification, sampling and processing of the detected magnetic fields were constructed (or purchased) and assembled. At each stage throughout the hardware development, research was also undertaken into the behavior of the AC magnetic fields and the development of a new method for the calculation of the position and orientation of a sensor. This analysis produced a method of calculating the position magnitude and sensor orientation. This research also resulted in the development of simple equations that allow the magnetic fields generated by an ideal three coil source to be predicted for any point in space. Although it may appear somewhat trivial, the result allowed a detailed comparison and analysis of the detected magnetic fields and provided a mathematical benchmark against which future calibration could take place.

In this regard the project was very successful, however two weaknesses in the system operation prevented the completion of the tracking system. The first and most obvious

weakness appeared in the calculation of the polarity of the position coordinates. Although a method of identifying the position coordinate polarity was proposed, it required significant processing time and was very susceptible to noise and the effects of inaccuracy in both the position magnitude and orientation calculations. This represents a significant drawback to the system, however it is by no means unresolvable as the Polhemus patents outline a method of position polarity calculation and it is likely that such a calculation may be performed using another independent method. The second significant weakness of the system related to the estimation of the polarity of the magnetic fields. The timing jitter within the detected magnetic fields often caused signals of low SNR to be incorrectly resolved and the time averaging and orientation calculations to be severely affected. This affected the magnetic fields as the SNR decreased and had implications for the translational accuracy of the system. Although these two problems presented significant difficulties in the project development, the overall body of work completed provides a strong basis for further development. A brief discussion of this basis follows with notes made of the most interesting and relevant points for future work.

9.1 Research into the Polhemus Fastrak

The research undertaken into the design and operation of the Polhemus Fastrak included an analysis of the hardware from which the system was constructed and the algorithms outlined in the tracking patents. A detailed schematic diagram of the Fastrak was developed including the relevant electronic components and the signals detected at each point in the circuitry during the tracking process. The datasheets of each component involved in the generation and detection of the magnetic fields were obtained (although many were obsolete) and analyzed so that an accurate description of the system functionality could be produced. This analysis revealed a careful design with well selected components and a well thought out implementation of analogue and digital circuitry. Polhemus produced subsequent revisions of the Fastrak during the course of the project which utilized power audio amplifiers (rather than Darlington transistors) for the generation of magnetic fields each of which were carefully calibrated using a feedback system. The signal sensing circuitry exhibited careful design through the use of very low noise ($1 \text{ nV}/\sqrt{\text{Hz}}$) instrumentation amplifiers which were carefully laid out and assigned to amplify the voltage detected on each coil. The exact winding and calibration method of the 4th coil was never fully researched as such a system was not implemented due to the limited calibration methods investigated. However this method of sensor calibration appeared to indicate the level of information which was required from each

sensor in order for an accurate measurement of the sensor position and orientation to be made.

ARANZ Scanning was able to provide the detailed calibration data used to describe the imperfections in each source and sensor. Each component contained a ROM IC with a detailed reference of the aperture and calibration measurements for each frequency of Fastrak operation. The exact use of each specification and method of using of this calibration data was not determined.

The patents owned by Polhemus Ltd [Kuippers (1988)][Jones (1988)][Jones (1994)] provided well written and detailed descriptions of the mathematical models used for magnetic tracking including the calculation of position and orientation using matrices and quaternions and also outlined detailed methods of system calibration. The patents were written by reputable authors (H. Jones and Dr J. Kuippers) and were developed by a highly qualified team [Raab (1978)] over a significant period of time (research into magnetic tracking has been undertaken since the early 1970's at Polhemus). The quality of the patents is reflected in the high level of performance produced by the Fastrak. It is therefore apparent that all aspects of the Polhemus Fastrak have been very carefully designed and that it will require significant time and effort to develop a tracking system of comparable speed and accuracy.

9.2 Work Completed

The work completed encompassed hardware, software and theoretical model development, with the aim of constructing a tracking system utilizing the Fastrak signal generation circuitry to reduce development time. The hardware development included the design, implementation and testing of several low noise amplification circuits which were required to interface the Fastrak sensor to a platform capable of processing the data. Once the hardware components had been designed, selected and connected appropriately, signal amplification circuitry was used to amplify the induced voltages so that they could be converted into sampled measurements for processing. The software used for this process was written in GNU C and implemented in Code Composer Studio using a number of previously written assembly files for implementing common mathematical functions. Using this software the detected magnetic fields were measured and the mathematical models developed were tested.

The position and orientation algorithms that were developed during this process are original to the best of the author's knowledge. The position calculation method does however

appear to be mathematically equivalent to that outlined in the Polhemus patent, but was developed using a different methodology and is expressed without matrix algebra. This does not imply that a copy was made of the Polhemus algorithm but rather that any method of calculation which arrives at an identical result (the determination of position and calculation) using the same parameters as a basis (the detected magnetic fields) will be likely to have some degree of equivalence. As a result little if any performance improvement can be anticipated from the position resolution algorithm apart from the reduced calculation time resulting because unused matrix elements not need to be calculated.

The orientation algorithm developed appears to be an effective method of calculating the sensor orientation, however it is affected by noise and is very sensitive to polarity errors in the resolved magnetic fields. It may however prove to be an attractive alternative to the patented algorithms as it provides a remarkably accurate method of determining the orientation when an accurate position is known. This may be achieved through further calibration which will not only increase the accuracy of the predicted magnetic field matrix B_P , but also increase the accuracy of the detected magnetic fields B_D and may therefore produce a significant increase in the accuracy of the resolved orientation. Perhaps one of the most useful results of the research undertaken was the development of equations which allowed the magnetic fields to be predicted for any given position in space. The equations provide a reference point against which the system can be checked.

The models and algorithms developed were supported by the application of simple calibration methods which allowed the detected signals to be modeled and corrected according to the imperfections within the system. The application of these methods allowed considerable improvements in the translational and angular accuracy parameters and showed good agreement with the magnetic field predicted by the equations developed. In spite of this, there are significant improvements that need to be made to the system to improve the calculation of position and orientation.

9.3 Future Work

The tracking system designed may be modified in a number of ways to increase accuracy, resolution, update rate, latency and functionality. The design of an AC magnetic tracking system is complex and although some improvements may be relatively straightforward to implement (such as processing optimization and implementation of an averaging system),

others are far more difficult and may require lengthy and detailed research. A brief summary of the possible areas of improvement follow, to illustrate the strengths and weaknesses of the work completed and recommend possible paths for future development.

9.3.1 Resolution Improvements

The results obtained in Chapter 8 illustrate that a significant performance increase could be obtained by averaging the subsequent samples of the detected magnetic fields to reduce the noise and increase the both the translational and angular resolution. Although the levels of performance achieved by the tracking system in this area were promising, the most precise measurements were averaged over a considerable number of static samples - a method which is simply not tenable in a high speed tracking system.

Averaging is not the only method that may be used to reduce the noise within the signal. Adaptive filters may also be used to significantly reduce the noise in the tracking system. Previous research [Yun (2003)] has been undertaken into the effectiveness of Kalman filters and their applicability to motion tracking, however this area of research is particularly complex as Kalman filters are only directly applicable to linear systems and must be modified in order to be applied to a nonlinear system.

The most effective method of improving the tracking resolution is not to improve the processing techniques but rather to prevent the noise from being introduced in the first place. The system utilized multiple amplification and detection platforms powered with different supplies to amplify and sample the generated signals. In addition to this, the timing jitter between the magnetic fields generated by the Fastrak and those detected by the tracking system generated a phase error within the spectral elements of the detected signal and effectively introduced noise into the system. These combined factors caused sufficient noise to be introduced to the detected signals so that the polarity of the detected magnetic fields could be incorrectly resolved. Not only did this increase the noise significantly, but it also caused significant error within the calculation of the sensor orientation. These problems may be significantly reduced if a complete tracking system is implemented using low noise amplification and sampling mechanism which controls both the signal generation and detection of the magnetic fields to a high level of accuracy.

9.3.2 Accuracy Improvements

The ‘magnitude averaging’ mechanism which was used to reduce the noise and improve the resolution of the tracking system had an unintended side effect: the introduction of a bias into the magnetic fields close to zero which caused a reduction in the accuracy of the position coordinates close to zero. The methods of improvement suggested in Section 8.2.3 provide one solution to reducing this bias, however the most effective method of bias reduction is to directly average the detected magnetic fields and thereby increase the SNR of the estimated values. This scheme was not implemented as timing errors in the sampled signals often caused the incorrect polarity of the magnetic fields to be estimated. Thus, by implementing a system which allows an accurate determination of the polarity of the magnetic fields to be made, the magnetic fields may be directly averaged.

Although the bias introduced by the noise accounts for a large portion of the position offsets, the reduction of the bias effects introduced through ‘magnitude averaging’ will not increase the translational and angular accuracy to a commercial standard. To achieve this level of accuracy requires a highly accurate measurement of the physical characteristics of each system component and an appropriate method of accounting for those imperfections in the position and orientation calculations. This may be undertaken using a similar methodology to the calibration process described in Chapter 7. A mathematical model describing an ideal system may be modified using the the distortion characteristics of each component. The modified model may then be matched against the detected magnetic field measurements. Once the model has been matched to the detected magnetic fields for a range of positions and orientations a correction model may be developed which either corrects the magnetic fields prior to calculation of the position and orientation or modifies the position and orientation algorithms to account for the component characteristics.

9.3.3 Speed Improvements

The speed of tracking operation was reflected in both the update rate and the latency specifications which produced good results when significant averaging was not required. The latency and update rate specifications achieved by the tracking system (65 updates per second and 15 milliseconds) are still well below those of the Fastrak (240 updates per second and 4 milliseconds) however improvements may be made to these specifications by optimizing a number of aspects relating to the software and hardware implementation of the tracking system.

The first and most appropriate method of improving the latency and update rate specification is to remove the unnecessary calculations from the tracking algorithms. The system directly calculated the FFT of each detected sample set and thus the FFT of nine 1024 sample signals was performed in order to calculate each measurement. These requirements could be reduced by calculating only the spectral components required for analysis of the detected magnetic fields. While this area of processing represents a significant portion of the excess calculations undertaken by the system, a number of other redundant processes may also be eliminated for example combining the position and orientation calculations which were implemented as individual functions.

Further optimizations may be made by using the hardware features available on the DSP such as direct memory access. This mechanism allows data to be transferred directly into memory from the ADCs so that one block of data may be sampled while a previously sampled block is being processed. Although this method will not improve the latency specification (the required time for processing has not changed) the increased throughput will allow the update rate to be significantly improved. A reduction in latency may be achieved by directly coding the algorithm in assembler to optimize the use of the hardware resources on the DSP so that the instructions may be ‘pipelined’ in the most efficient manner possible.

Instead of using a single DSP for all operations an external microcontroller (such as the LPC3180 or LPC2148) could be incorporated to transfer and convert data. The use of an external high speed microcontroller would allow a reduction in latency and fast communication via a USB connector. In addition, multiple DSPs may be used to estimate multiple sensor measurements (since DSP s are a relatively modest \$20 (US) each). An FPGA would also be suited to such an application, however the required development time may make this option less attractive.

Finally, it should be noted that a complete system may be implemented with a significant reduction in the latency and update rate specifications. The current system required to use a polled-waiting method to synchronize with each new waveform, however a complete system does not require such a waiting scheme and may produce and sample measurements according to the limitations of processing speed.

9.3.4 Algorithmic Improvements

The algorithms calculate the position and orientation of the sensor using trigonometric functions and allow calculation of the position using rotation matrices. The method of using rotation matrices to represent the sensor orientation is not optimal, however, as certain positions exist for which the sensor orientation cannot be resolved (i.e. the phenomena of *gimbal lock* described in Section 5.2.2).

These problems may be avoided by using quaternion rotation which allow the sensor orientation to be resolved without ambiguity or discontinuity. A number of very useful papers [Diebel (2006)] and books exist which provide useful descriptions of the various mathematical representations of the quaternion which may be used to implement a quaternion based tracking algorithm.

9.3.5 Physical Improvements

A number of aspects regarding both the physical construction of the system and the components used to generate and detect magnetic fields may also be implemented to increase the tracker performance. Such aspects include the connection of a grounding system to the sensor wiring reducing the noise introduced through the use of RCA connectors. Additional hardware improvements may be made in the resonant circuit and feedback design and in other aspects of the precision analog and digital design.

9.3.6 Functionality

A number of functional improvements are possible which may be used to extend the tracking system. Such improvements include the transmission of multiple frequencies simultaneously (excitation of each source coil at a different frequency) and the use of multiple sensors in a fixed arrangement to measure the distortive effects of nearby metallic objects. The magnetic tracking system may also be implemented as a MARG system as outlined in Section 1.2.6 so that the algorithm takes into account the effects measured by independent sensors in the system.

9.4 Conclusions

A number of conclusions may be drawn from the research and development completed. The first is that the position and orientation calculations developed are both valid and provide accurate methods of tracking. The performance of these algorithms will need to be investigated further before the position and orientation measurements can be assigned a specific angular resolution or position resolution. The second is that the magnetic fields for any given sensor position and orientation may be predicted using the equations developed. The equations can be used to calibrate the system and are invaluable when comparing the differences between theoretical and practical measurements. The third conclusion is that the simple calibration scheme is sufficient to remove much of the distortion in the sensor but requires further development is required to improve the accuracy of the position and orientation.

The tracking system developed did not meet the required specifications. In retrospect this is unsurprising given that the market leaders have actively researched this area for 30 years and have a thorough knowledge of the practical and theoretical aspects of the system. This conclusion should not detract from the significant results obtained, however, as the work outlined provides an original perspective and a new path upon which further research may be based. Significant performance improvements may be made by eliminating the timing errors in sampled measurements. Enhancements may also be made by implementation of a complete and comprehensive calibration system. This is not a straightforward task and will require a thorough theoretical analysis of the system combined with a precise practical construction. If correctly implemented there is no reason why this research project could not lead to a useful tracking system in the near future.

9. DISCUSSION AND CONCLUSIONS

References

- G. ARFKEN, *Mathematical Methods for Physicists*, Academic Press Incorporated ©1968, Referenced on Page 56
- W. BIRKFELLNER, F. WATZINGER, F. WANSCHITZ, R. EWERS, H. BERGMANN, *Calibration of Tracking Systems in a Surgical Environment*, IEEE Transactions on Medical Imaging, Volume 17, Number 5, Pages 737-742, October 1998.
- J. DIEBEL, *Representing Attitude: Euler Angles, Unit Quaternions, and Rotation Vectors*, (Unpublished) October 2006, Referenced on Page 102
- B. GURU, H. HIZIROGLU, *Electromagnetic Field Theory Fundamentals*, PWS Publishing Company ©1998, Referenced on Page 54
- J. HUMMEL, M. FIGL, C. KOLLMANN, H. BERGMANN, W. BIRKFELLNER, *Evaluation of a Miniature Electromagnetic Position Tracker*, Medical Physics, Volume 29, Number 10, Pages 2205-2212, October 2002,
- M. IKITS, J. BREDESON, C. HANSEN, J. HOLLERBACH, *An Improved Calibration Framework for Electromagnetic Tracking Devices*, IEEE Proceedings on Virtual Reality, Pages 63-70, March 2001.
- H. JONES, *Method and Apparatus For Determining Remote Object Orientation and Position*, United States Patent Number 4,737,794, April 1988, Referenced on Pages 15, 97
- H. JONES, *Non-Concentricity Compensation in Position and Orientation Measurement Systems*, United States Patent Number 5,307,072, April 1994, Referenced on Pages 15, 97
- J. KUIPPERS, *Method and Apparatus for Determining Remote Object Orientation and Position*, United States Patent Number 4,742,356, May 1988, Referenced on Pages 15, 22, 97

REFERENCES

- Y. LIU, Y. WANG, D. ZHOU, X. HU, J. WU, *Study on an Experimental AC Electromagnetic Tracking System*, IEEE Proceedings of the 5th World Congress on Intelligent Control and Automation, Volume 4, Pages 3692-3695, June 2004, Referenced on Page 15
- LYRTECH, *Professional Audio Development Kit: Technical Reference Guide* ©2006, Referenced on Pages ix, 25
- J. MCCLAVE, T. SINCICH, *Statistics 8th Edition*, Prentice Hall Inc. ©2000, Referenced on Page 79
- POLHEMUS, *Fastrak Tracking System Reference Manual*, ©2004, Referenced on Pages 3, 9, 77, 78
- E. PAPERNO, I. SASADA, E. LEONOVICH, *A New Method for Magnetic Position and Orientation Tracking*, IEEE Transactions on Magnetics, Volume 37, Issue 4, Part 1, Pages 1938-1940, July 2001.
- F. ROUSSEAU, C. BARILLOT, *Quality Assessment of Electromagnetic Localizers in the Context of 3D Ultrasound*, Institut National De Recherche En Informatique En Automatique 2002, Referenced on Page 78
- F. RAAB, E. BLOOD, T. STEINER, H. JONES, *Magnetic Position and Orientation Tracking System*, IEEE Transactions on Aerospace and Electronic Systems, Volume AES-15, Issue 5, Pages 709-718, September 1978, Referenced on Page 97
- G. RICKER, J. WILLIAMS, *Redundant Sensitivity Processing*, IEEE Transactions on Audio and Electroacoustics, Volume 2, Number 4, Pages 348-354, August 1973.
- G. SLABAUGH, *Computing Euler Angles from a Rotation Matrix*, (Unpublished), August 1999, Referenced on Page 46
- H. SO, K. MA, T. CHAN, *Detection of Narrowband Random Signals Via Spectrum Matching*, IEEE Proceedings of the Midwest Symposium on Circuits and Systems, Pages 238-241, August 1998, Referenced on Page 30
- S. WEI, P. NAG, G. BLANTON, A. GATTIKER, W. MALY, *To DFT or not to DFT?*, IEEE International Test Conference Proceedings, Pages 557-566, November 1997.
- X. YUN, M. LIZARRAGA, E. BACHMANN, R. MCGHEE, *An Improved Quaternion-Based Kalman Filter for Real-Time Tracking of Rigid Body Orientation*, IEEE Proceedings of the

International Conference on Intelligent Robots and Systems, Volume 2, Pages 1074-1079, October 2003, Referenced on Page 99

G. ZAKARIA, A. BEEB, *Using DFT and interpolation to reconstruct narrowband signals buried in noise*, IEEE Proceedings of the 26th Southeastern Symposium on System Theory, Pages 437-441, March 1994.

REFERENCES

Appendix A

Research Apparatus

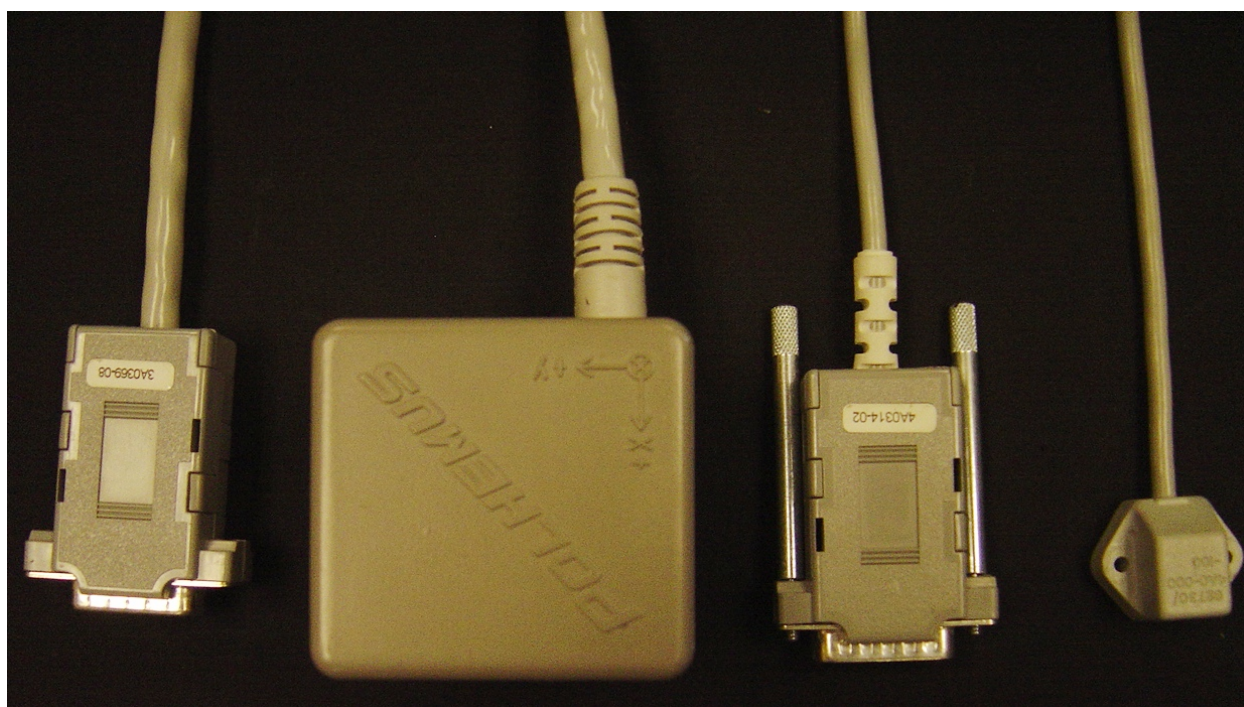


Figure A.1: Fastrak Sensor used for the detection of AC magnetic fields via the professional audio development kit.

A. RESEARCH APPARATUS

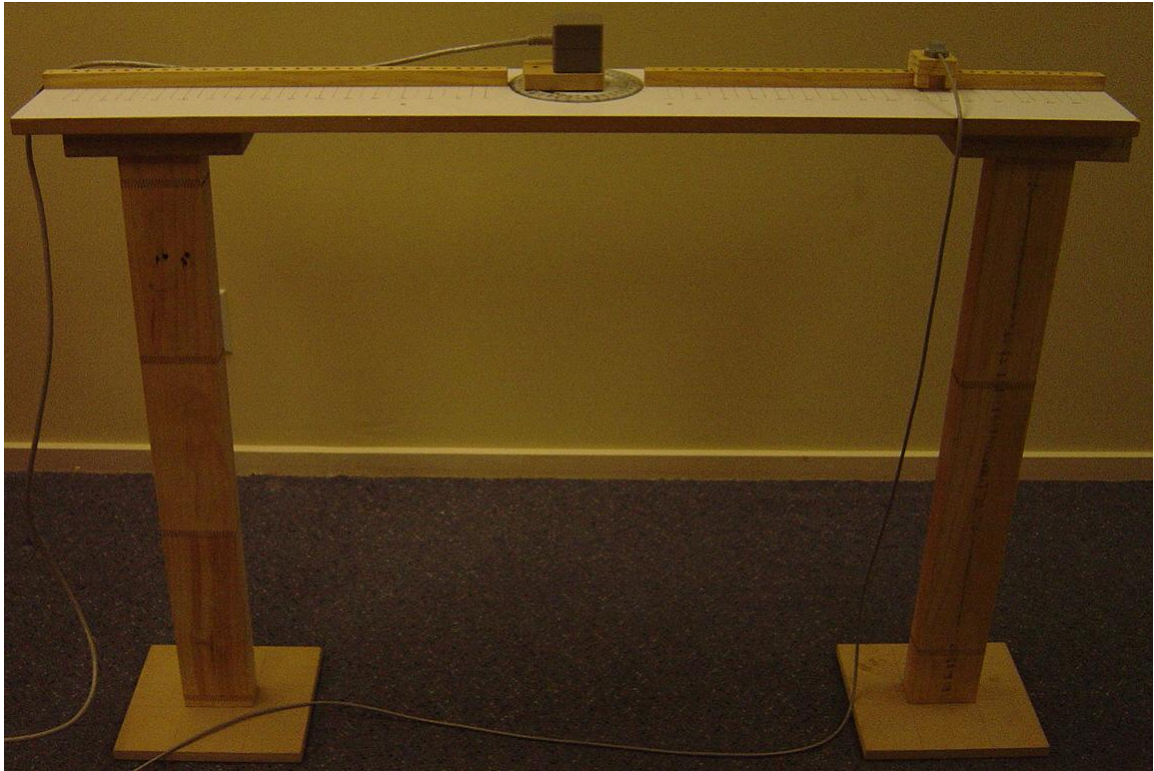


Figure A.2: Test jig apparatus used for the measurement and analysis of magnetic fields.

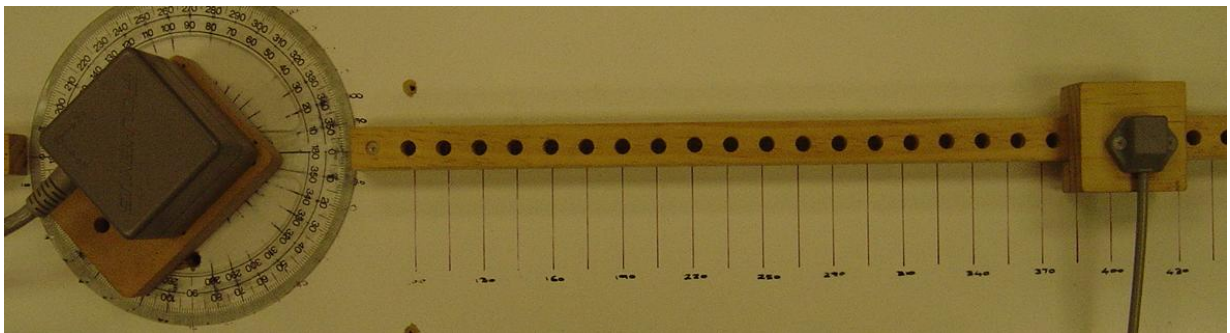


Figure A.3: Source rotation test jig setup.

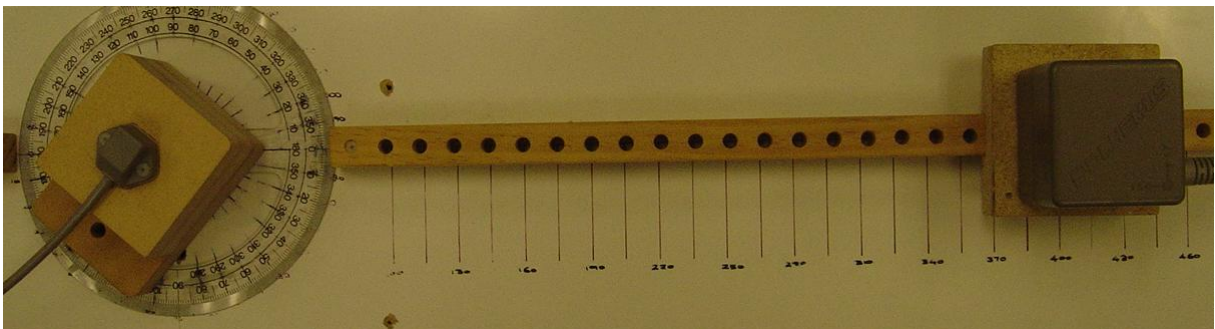


Figure A.4: Sensor rotation test jig setup.

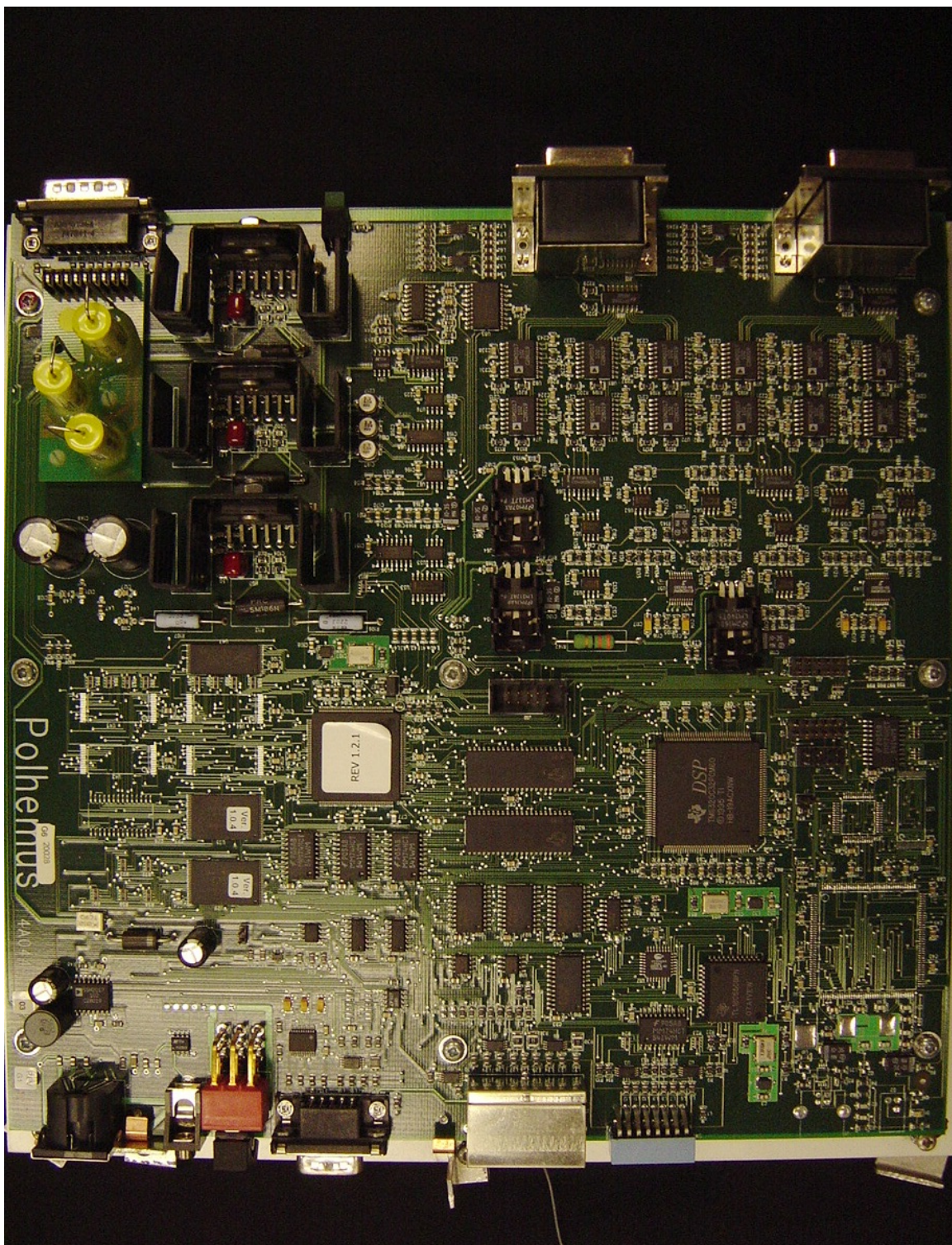
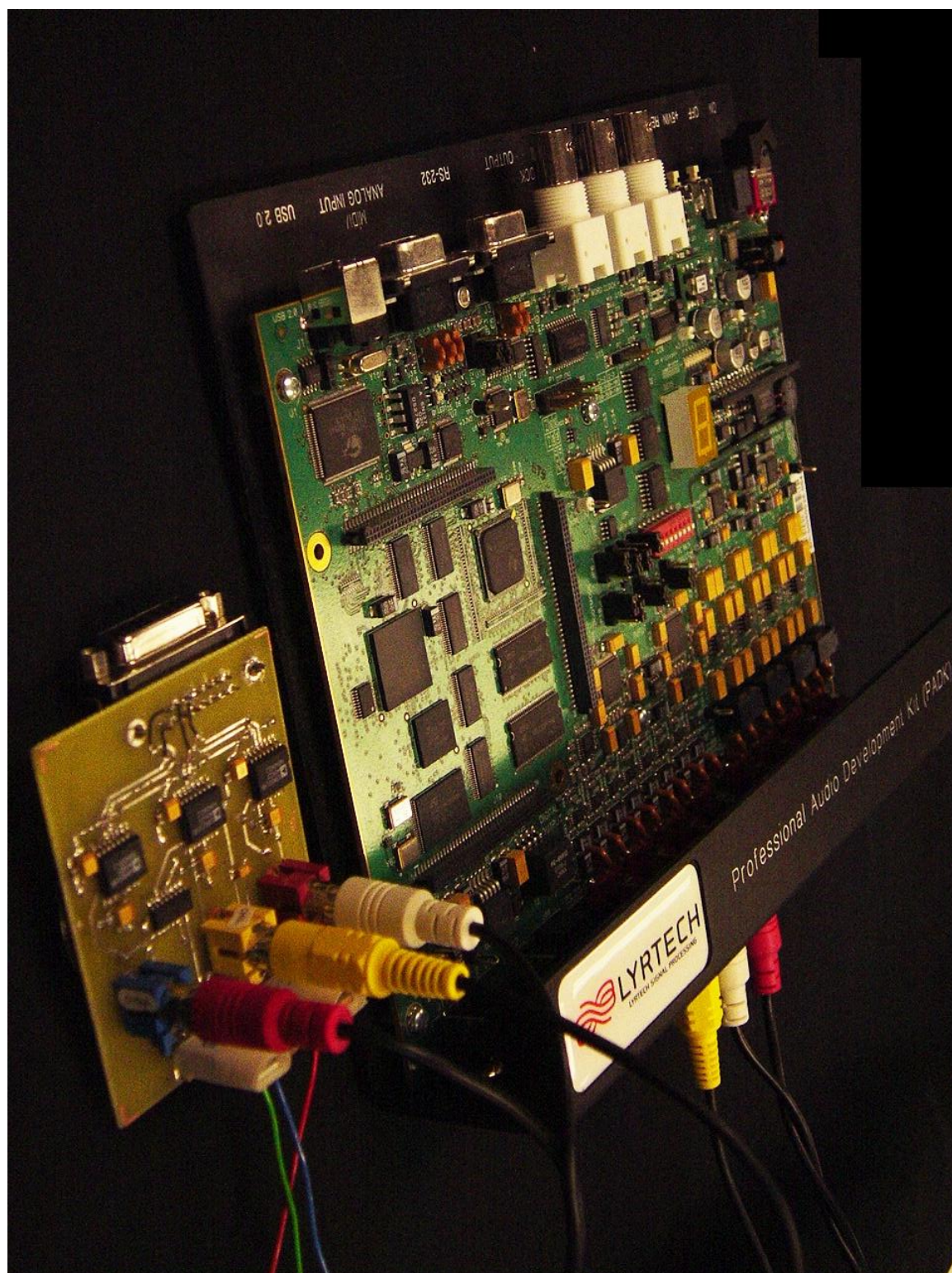


Figure A.5: The Fastrak printed circuit board.

A. RESEARCH APPARATUS

Figure A.6: . The Professional Audio Development Kit and the signal amplification circuitry used to amplify and sample voltages induced on the sensor



Appendix B

Coupled Coils Analysis

Ref: Paul and Nasar, 1982, Ex. 4.9, pp 178-9.

Notes by Phil Bones, University of Canterbury, January 2006.

Revised October 6th 2006.

B.1 Field for current-carrying circular coil

Consider a circular single-turn coil, coaxial with the z -axis and lying in the xy -plane and carrying current I in the right-handed manner w.r.t. z , i.e. in the direction of $+\phi$ (r , θ and ϕ are spherical coordinates). The coil has radius a_1 . The origin of coordinates (and centre of the coil) is O . The magnetic field strength of the field from the coil is

$$\mathbf{B} = \nabla \times \mathbf{A}, \quad (\text{B.1})$$

where \mathbf{A} is the ‘magnetic vector potential’, given by

$$\mathbf{A} = \int_V \frac{\mu_0 \mathbf{J} dv}{4\pi R}, \quad (\text{B.2})$$

where \mathbf{J} is current density in amps/m², R is the distance from the point of integration to the field point considered, dv is the volume element of integration and V is the volume containing all of the current generating the magnetic field.

Let a point on the coil be represented by angle ϕ' , where ϕ' is defined exactly as for ϕ . For a small element of the coil subtending angle $d\phi'$ at the origin, the elemental vector magnetic potential is

$$d\mathbf{A} = \frac{\mu_0 I a_1 d\phi'}{4\pi R} \hat{\mathbf{i}}_{\phi'}. \quad (\text{B.3})$$

where $\hat{\mathbf{i}}$ is unit vector in the \cdot direction.

Now consider a point P on the xz -plane, i.e. $P = (x, 0, z)$. P thus has spherical coordinate $\phi = 0$. Pairing elements as given by Eq. B.3 for $+\phi'$ and $-\phi'$, \mathbf{A} for each such pair is directed in a plane parallel to the xy -plane in the ϕ direction, thus

$$\mathbf{A}(P) = A_\phi \hat{\mathbf{i}}_\phi = \frac{\mu_0 I}{4\pi} 2 \int_0^\pi \frac{a_1 \cos\phi' d\phi'}{R} \hat{\mathbf{i}}_\phi.$$

Utilising the cosine rule,

$$R^2 = a_1^2 + x^2 + z^2 - 2a_1x \cos\phi',$$

which leads to

$$\mathbf{A} = \frac{\mu_0 I}{2\pi} \int_0^\pi \frac{a_1 \cos\phi' d\phi'}{(a_1^2 + x^2 + z^2 - 2a_1x \cos\phi')^{\frac{1}{2}}} \hat{\mathbf{i}}_\phi. \quad (\text{B.6})$$

This is a general expression for the exact field from the circular coil and can be applied to any point by simple rotation around the z -axis.

B.2 Far-field approximation

In the far field, noting that the point P is in the xz -plane, $r^2 = x^2 + z^2 \gg a_1^2$, therefore

$$\begin{aligned} R^2 &= r^2 + a_1^2 - 2a_1x \cos\phi' \\ &\simeq r^2 - 2a_1x \cos\phi' \\ \frac{1}{R} &= \frac{1}{r} \left(1 - \frac{2a_1x \cos\phi'}{r^2}\right)^{-\frac{1}{2}} \\ &\simeq \frac{1}{r} \left(1 + \frac{2a_1x \cos\phi'}{r^2}\right). \end{aligned}$$

Using this geometric approximation, therefore,

$$\begin{aligned} \mathbf{A} &\simeq \frac{\mu_0 I a_1}{2\pi r} \left[\int_0^\pi \cos\phi' d\phi' + \frac{a_1 x}{r^2} \int_0^\pi \cos^2\phi' d\phi' \right] \hat{\mathbf{i}}_\phi \\ &= \frac{\mu_0 I a_1^2 x}{2\pi r^3} \left(\frac{\pi}{2}\right) \hat{\mathbf{i}}_\phi \\ &= \frac{\mu_0 I a_1^2 x}{4r^3} \hat{\mathbf{i}}_\phi. \end{aligned}$$

Also $x = r \sin\theta$ and the product $\pi a_1^2 I$ is the magnitude of the dipole moment, m , equiv-

alent to the coil in the far field. Therefore

$$\mathbf{A} = \frac{\mu_0 m \sin\theta}{4\pi r^2} \hat{\mathbf{i}}_\phi, \quad (\text{B.7})$$

and, using Eq. B.1,

$$B_r = \frac{\mu_0 m \cos\theta}{2\pi r^3} \quad (\text{B.8})$$

$$B_\theta = \frac{\mu_0 m \sin\theta}{4\pi r^3} \quad (\text{B.9})$$

$$B_\phi = 0. \quad (\text{B.10})$$

B.3 Mutual inductance between two small circular coils

In this section, the mutual inductance between two circular single-turn coils is analysed. Coil 1, radius a_1 , carries current I ; Coil 2 has radius a_2 . The centres of the two coils are a distance R_{12} apart with $R_{12} \gg a_1, a_2$. From the definition of the mutual inductance (in Henries),

$$L_{21} = \frac{\Psi_{21}}{I_1}, \quad (\text{B.11})$$

where Ψ_{21} is the total flux in Webers coupling Coil 2 as a result of the current I_1 in Coil 1 in Amps.

For the purpose of the analysis presented in this section, the magnetic field strength at every point within the interior of Coil 2 is assumed to be equal to that at the centre of the coil. Four cases are considered:

1. the two coils are coplanar,
2. the two coils are coaxial,
3. the planes of the two coils are parallel, but the coils are placed arbitrarily, and
4. the locations and orientations of the coils are arbitrary.

B.3.1 Coplanar coils

Consider that the two small coils lie in a common plane. Without loss of generality that plane is taken to be the xy -plane ($z = 0$), with Coil 1 centred on O . From Eqs. B.8, B.9 and B.10,

the magnitude of the magnetic field at the centre of Coil 2 (with \mathbf{B} oriented normal to the coil) is

$$\begin{aligned} B_2 &= B_\theta(R_{12})|_{\theta=\frac{\pi}{2}} \\ &= -\frac{\mu_0 m_1}{4\pi R_{12}^3} \end{aligned}$$

Thus

$$\begin{aligned} \Psi_{21} &\simeq -\frac{\mu_0 m_1 \pi a_2^2}{4\pi R_{12}^3} \\ &= -\frac{\mu_0 I_1 \pi a_1^2 a_2^2}{4R_{12}^3}. \end{aligned}$$

Thus for the coplanar case,

$$L_{21} \simeq -\frac{\mu_0 \pi a_1^2 a_2^2}{4R_{12}^3}. \quad (\text{B.12})$$

Note that the negative sign occurs since a right-handed current I_1 induces an EMF in Coil 2 which is negative w.r.t. the positive rotation direction for the coil.

B.3.2 Coaxial coils

Consider the case when the two small coils lie along a common axis (and the planes of the coils are perpendicular to that axis). Without loss of generality the common axis is taken to be the z -axis, the plane of Coil 1 is taken to be $z = 0$ and the plane of Coil 2 is taken to be the plane $z = R_{12}$. From Eqs. B.8, B.9 and B.10, the magnitude of magnetic field at the centre of Coil 2 (with \mathbf{B} oriented normal to the coil) is

$$\begin{aligned} B_2 &= B_r(R_{12})|_{\theta=0} \\ &= \frac{\mu_0 m_1}{2\pi R_{12}^3} \end{aligned}$$

Thus

$$\begin{aligned} \Psi_{21} &\simeq \frac{\mu_0 m_1 \pi a_2^2}{4\pi R_{12}^3} \\ &= \frac{\mu_0 I_1 \pi a_1^2 a_2^2}{2R_{12}^3}. \end{aligned}$$

Thus for the coaxial case,

$$L_{21} \simeq \frac{\mu_0 \pi a_1^2 a_2^2}{2R_{12}^3}. \quad (\text{B.13})$$

B.3.3 Parallel-plane coils

Consider the case when the two small coils lie in planes which are parallel. Without loss of generality the plane of Coil 1 is taken to be $z = 0$, with Coil 1 centred on O , while the plane of Coil 2 is taken to be the plane $z = \text{some constant}$. From Eqs. B.8, B.9 and B.10, the magnetic field at the centre of Coil 2 is

$$\begin{aligned} \mathbf{B}_2 &= \mathbf{B}(R_{12}, \theta) \\ &= B_r(R_{12}, \theta) \hat{\mathbf{i}}_r + B_\theta(R_{12}, \theta) \hat{\mathbf{i}}_\theta. \end{aligned}$$

Thus

$$\begin{aligned} \Psi_{21} &\simeq [B_r(R_{12}, \theta) \cos\theta - B_\theta(R_{12}, \theta) \sin\theta] \pi a_2^2 \\ &= \frac{\mu_0 I_1 \pi a_1^2 a_2^2}{2R_{12}^3} \left[\cos^2\theta - \frac{\sin^2\theta}{2} \right]. \end{aligned}$$

Thus for the parallel plane case,

$$L_{21} \simeq \frac{\mu_0 \pi a_1^2 a_2^2}{2R_{12}^3} \left[\cos^2\theta - \frac{\sin^2\theta}{2} \right]. \quad (\text{B.14})$$

B.3.4 Coils with arbitrary positions and orientations

Consider the case when the two small coils lie in arbitrary positions and orientations. The coordinate system is arranged so that the plane of Coil 1 is $z = 0$, with Coil 1 centred on O and the location of the centre of Coil 2 is given by $(r, \theta, \phi) = (R_{12}, \theta, 0)$, i.e., the centre of Coil 2 lies in the xz -plane. The orientation of Coil 2 is given by the unit normal $\hat{\mathbf{n}}_2$. From Eqs. B.8, B.9 and B.10, the magnetic field at the centre of Coil 2 is

$$\begin{aligned} \mathbf{B}_2 &= \mathbf{B}(R_{12}, \theta) \\ &= B_r(R_{12}, \theta) \hat{\mathbf{i}}_r + B_\theta(R_{12}, \theta) \hat{\mathbf{i}}_\theta. \end{aligned}$$

Thus

$$\begin{aligned}
 \Psi_{21} &\simeq \mathbf{B}_2 \cdot \hat{\mathbf{n}}_2 \pi a_2^2 \\
 &= \left[B_r \hat{\mathbf{i}}_r \cdot \hat{\mathbf{n}}_2 + B_\theta \hat{\mathbf{i}}_\theta \cdot \hat{\mathbf{n}}_2 \right] \pi a_2^2 \\
 &= \frac{\mu_0 I_1 \pi a_1^2 a_2^2}{2R_{12}^3} \left[\hat{\mathbf{i}}_r \cdot \hat{\mathbf{n}}_2 \cos\theta + \frac{\hat{\mathbf{i}}_\theta \cdot \hat{\mathbf{n}}_2 \sin\theta}{2} \right].
 \end{aligned}$$

Thus for the case of arbitrary positions and orientations,

$$L_{21} \simeq \frac{\mu_0 \pi a_1^2 a_2^2}{2R_{12}^3} \left[\hat{\mathbf{i}}_r \cdot \hat{\mathbf{n}}_2 \cos\theta + \frac{\hat{\mathbf{i}}_\theta \cdot \hat{\mathbf{n}}_2 \sin\theta}{2} \right]. \tag{B.15}$$